Section 7

XRCF Efficiency and Effective Area Measurements

7.1 Overview

7.1.1 Diffracted Order Sign Convention

Note: By convention the sign of a diffracted order is given by the corresponding sign of the image location reported by the detection system:

Phase 1, HXDS – the $m = +1$ order is in the $+Y_{\mathrm{xrcf}}$ direction

ACIS-2C – the $m = +1$ order is in the $+Y_{\mathrm{xrcf}}$ direction

ACIS, HRC – the $m = +1$ order is in the $+Y_{\mathrm{Det}}$ direction, that is in the $-Y_{\mathrm{xrcf}}$ direction

7.1.2 Effective Area

One of the key calibration activites to be carried out at the XRCF is the measurement of the effective area of the AXAF. For the HETGS this effective area depends on the performance of the HRMA, HETG, and ACIS-S, that is:

$$A_{hetgs}(E, m, \mathrm{mode}) = \sum_{s=1,3,4,6} A_s(E)\ G_s(E, m)\ QE_{acis}(E, \vec{X}, \mathrm{mode}). \tag{7.1}$$

where the three contributing elements are the HRMA single shell effective areas (A_s), the effective HETG grating efficiencies (G_s) for the mirror shells, and the ACIS-S photon detection efficiencies (QE_{acis}). Here E denotes the dependence on energy, m the diffraction order, *mode* the event identification in the CCD (here, for example, we will consistently use the sum of

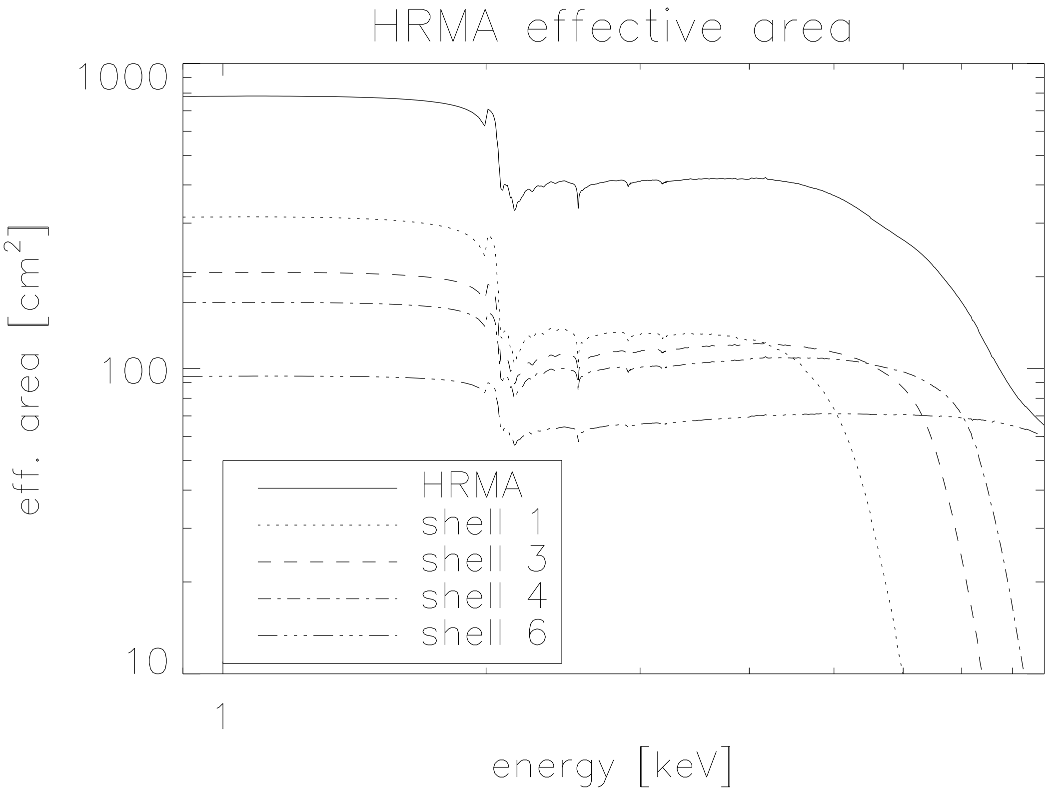

Figure 7.1: HRMA effective areas. The straight line shows the total area, followed by the ones for each shell (courtesy of the AXAF MST).

ASCA grades 0,2,3,4,6 and TE-mode), and the $\vec{X}$ dependences from spatial dependencies in the detector array, i.e FI/BI efficiencies and gap locations between the devices.

Figure 7.1 shows the total AXAF HRMA on-axis effective area at XRCF and its contributing single shell areas. Mirror shells 1 and 3 cut off at energies around 5 and 6.5 keV, while shells 4 and 6 extend up to 7 and 9 keV. The decrease near 2 keV is due to the iridium M-edge in the reflective mirror coating. The effective area sum, equation 1 above, then adds s = 1 and 3 for the MEG area and 4 and 6 for the HEG area.

The grating efficiencies have been determined from laboratory measurements, Section 4.2, where the diffraction efficiency of each flight grating was measured at several energies and orders and positions within each facet. Figure 7.2 show the predicted efficiencies for MEG and HEG. Displayed are the zeroth order (solid line) and the 1st and 3rd positive order in MEG, and the 1st and 2nd order in HEG, which are the dominant orders for each grating.

In general each CCD device has its own characteristics. However, since not all quantum efficiency functions are yet avalable, we have to use templates for each CCD type. Figure 7.3 shows the quantum efficiencies for the FI device in I3 of the imaging array versus the BI device in S3 of the spectroscopy array. The functions already include the transmission characteristics of the flight filters. The use of these templates is reasonable since FI devices are quite similar and we only expect systematic deviations of the order of 5%. The difference between the two BI devices (S1, S3) should not be significantly larger. However, as we will show during the analysis, the

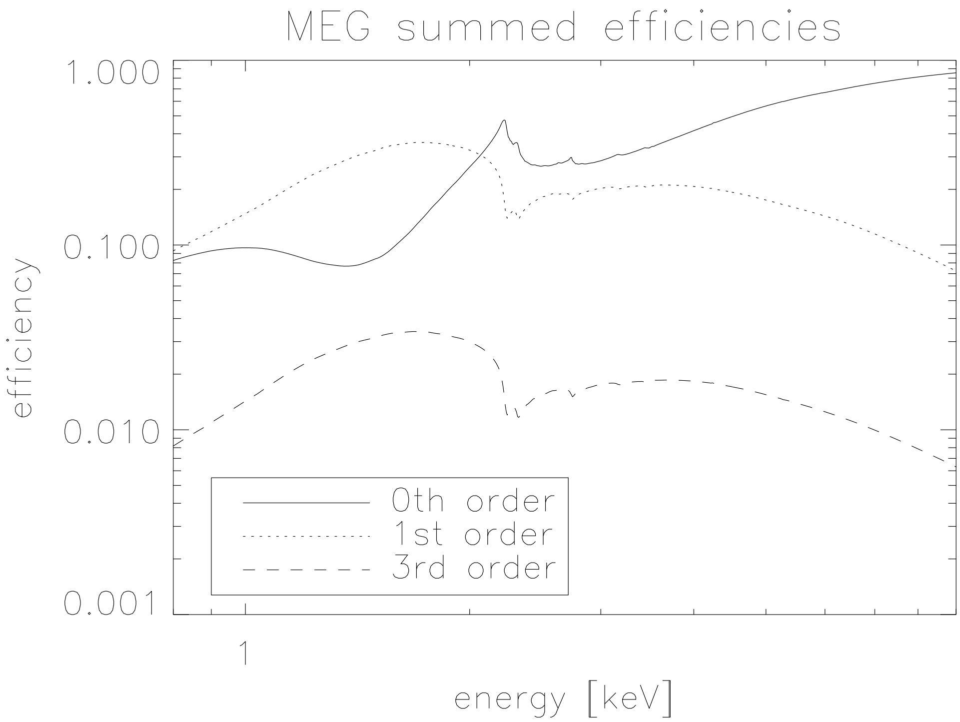

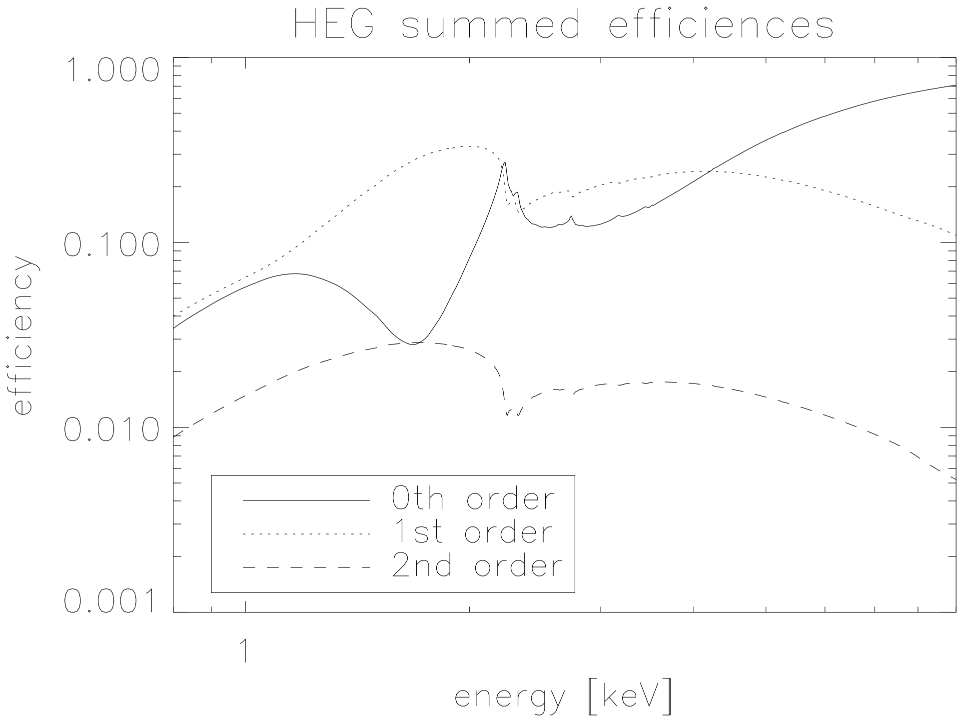

Figure 7.2: MEG (top) and HEG (bottom) efficiencies as a function of energy, from subassembly data analysis.

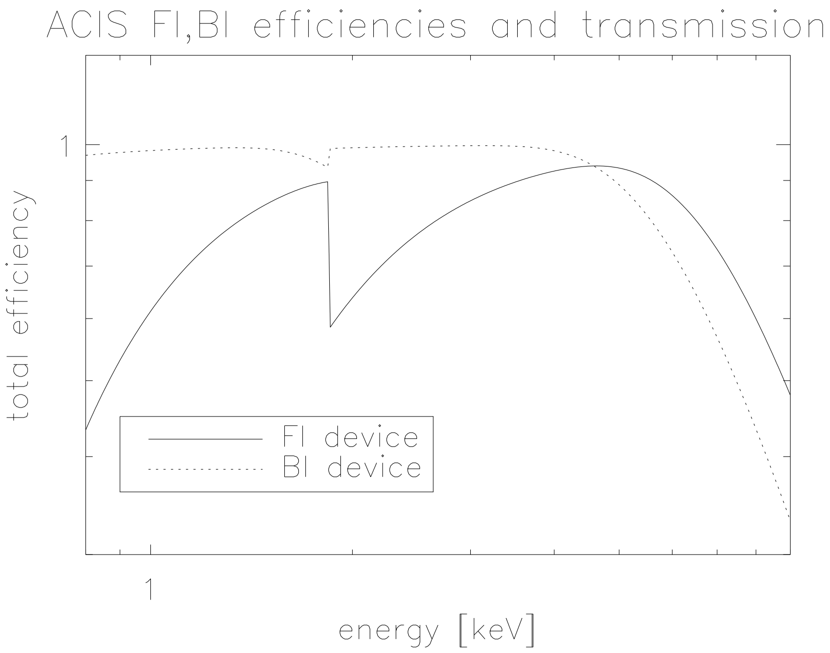

Figure 7.3: ACIS-S efficiencies. The product chip quantum efficiency times optical blocking filter filter transmission is plotted as a function of energy for the FI device I3 in ACIS-I and for the BI device S3 in ACIS-S (courtesy of the MIT ACIS team).

differences are visible in the data.

7.1.3 Divide and Conquer

An important step in the effective area calibration process is the division of XRCF testing into Phase 1 and Phase 2. In Phase 1 more traditional X-ray detectors are used to test the HRMA and HETG; this removes the flight detector complexities, uncertainties, and limitations. In this phase it is useful to consider the *optic effective area (OEA)* which represents the ability of the optics to collect photons at energy $E_{\rm line}$ into order m. This quantity does not include the detector quantum efficiency and so is a property of the optics only:

$$OEA_{2\pi}(E_{\rm line}, m) = \frac{\text{focal plane photons/s in line}-\text{order}}{\text{source flux in line}} \quad [\frac{\text{photons/s}}{\text{photons/cm}^2\text{s}} = \text{cm}^2] \tag{7.2}$$

Note that we get the usual cm^2 units, as for example in the HRMA-only effective area analysis[39]. The subscript "2π" (steradians) is used to indicate that this is the effective area over the full focal plane (half sphere) behind the HRMA and includes all structure in the diffracted order, *e.g.*, LEG support structure pattern. Low-level scattering by the HEG, Sections 3.3 and 6.6, is not considered a contribution to these integer diffraction orders, however. From a prediction or modeling point of view, the optic effective area for the mirror-grating combination is calculated from the following terms:

$$OEA_{2\pi}(E_{\rm line}, m) = \sum_{s=1,3,4,6} A_s(E_{\rm line})\ G_s(E_{\rm line}, m) \tag{7.3}$$

where the terms have been defined in Section 1.3.1. Going a step further, the ratio of optic effective areas can be used to measure the grating diffraction efficiency $G_s(E_{\rm line}, m)$ itself.

7.1.4 Order Ratios

A further simplification in the experiment can be made by measuring the grating efficiency as a ratio of grating-in to grating-out effective areas. This technique reduces the dependencies on the properties of the mirrors, detectors, or X-ray source.

Finally, for higher orders, the ratio of the higher order to the first order can be determined. These results can be compared with subassembly predictions. This approach has several advantages. It is not necessary to know the incident beam flux, mirror response, or absolute detector efficiency. The beam need not be spectrally pure, since only dispersed orders are used in this analysis. However, variations in detector uniformity must be considered, as they can affect the result, that is:

$$\frac{R_{\rm m^{th}}}{R_{\rm 1^{st}}}(E) = \frac{QE_{\rm Det}(E, \vec{X_m}) \sum_{s={\rm config}} A_s(E) G_s(E, m)}{QE_{\rm Det}(E, \vec{X_1}) \sum_{s={\rm config}} A_s(E) G_s(E, 1)} \tag{7.4}$$

where $QE_{\rm Det}(E, \vec{X_*})$ is the quantum efficiency of the detector at the different detected spatial regions ($m^{\rm th}$ and 1st orders) and the other terms have been previously defined. Note that the case where $m = -1$ is useful for uncovering detector uniformity effects and is applied to the flight detectors in Sections 7.7 and 7.9.

7.1.5 Test Strategy and Overview

The 1st-order HRMA-HETG effective area curves can be divided (somewhat arbitrarily) into 5 regions where different physical mechanisms govern the effective area of the optical (mirror-grating) system:

below 1 keV – The polyimide membrane of the gratings is dominating the area changes, with edges due to C, N, and O.

1-2 keV – The phase effects of the grating cause an increasing enhancement of the diffraction efficiency.

2-2.5 keV – Edge structure from the mirror (Ir) and grating (Au) dominates, sharply reducing effective area.

2.5-5.5 keV – Effective area is slowly varying, with some low-amplitude Ir and Au edge structure.

5.5-10 keV – The mirror reflectivity and grating efficiency are decreasing rapidly with energy.

Most of the effective area tests carried out at XRCF, Tables 5.5 and 5.6, were designed to illuminate the HRMA with a near monochromatic beam in order to sample one energy at a time. For example the Phase 1 tests with the EIPS using non-flight detectors, Section 7.4, tests using the ACIS-S and HRC-I as a detectors in order to test the predictions of high order efficiencies, Section 7.10, and tests using the Double Crystal Monochromator in order to examine the HETGS effective area at a wide range of discrete energies, Section 7.7.

In contrast, a set of tests employed the Electron Impact Point Source (EIPS) at high voltage and current in order to obtain a bright continuum, Section 7.8. These data can then be used to probe for unexpected spectral features or deviations near the sharp M edges due to the iridium on the HRMA and gold in the gratings. An original purpose of the tests was to test for molecular contamination on the mirrors by examining the mirror Ir M edge decrement, so the tests were given the designation "MC".

The result of combining these types of effective area tests is confidence in the instrument model in terms of both absolute effective area and detailed variation with energy.

7.2 Alignment Tests

Objective: Compare the defocussed ("ring focus") images with and without the HETG inserted to look for any gross vignetting that would indicate a decentering of the HETG with respect to the HRMA rays.

Using data from the no-grating ring-focus image C-IXH-RF-1.005 (961223/106856) and the grating-in "alignment" image C-HXH-AL-4.002 (961223/106860), the sector-by-sector grating-in/grating-out ratio is measured. The measured ratios are shown in Figure 7.4 for shells 1 and 6 (wide histograms.) Also plotted is a simple estimate of each grating's zero-order diffraction efficiency (from the X-GEF facet measurements) as it varies around the shell. The measured ratios have been adjusted by an overall normalization. This very preliminary analysis shows rough agreement between the measured and predicted efficiency variations; a more detailed analysis should allow vignetting and decenter limits to be placed on the as-installed HETG at XRCF.

To-do:
Re-analyze the images on a finer scale
Use the detailed X-GEF model parameters to create zero-order efficiency values.
Analyze the reference BND data to set absolute scale for normalization.

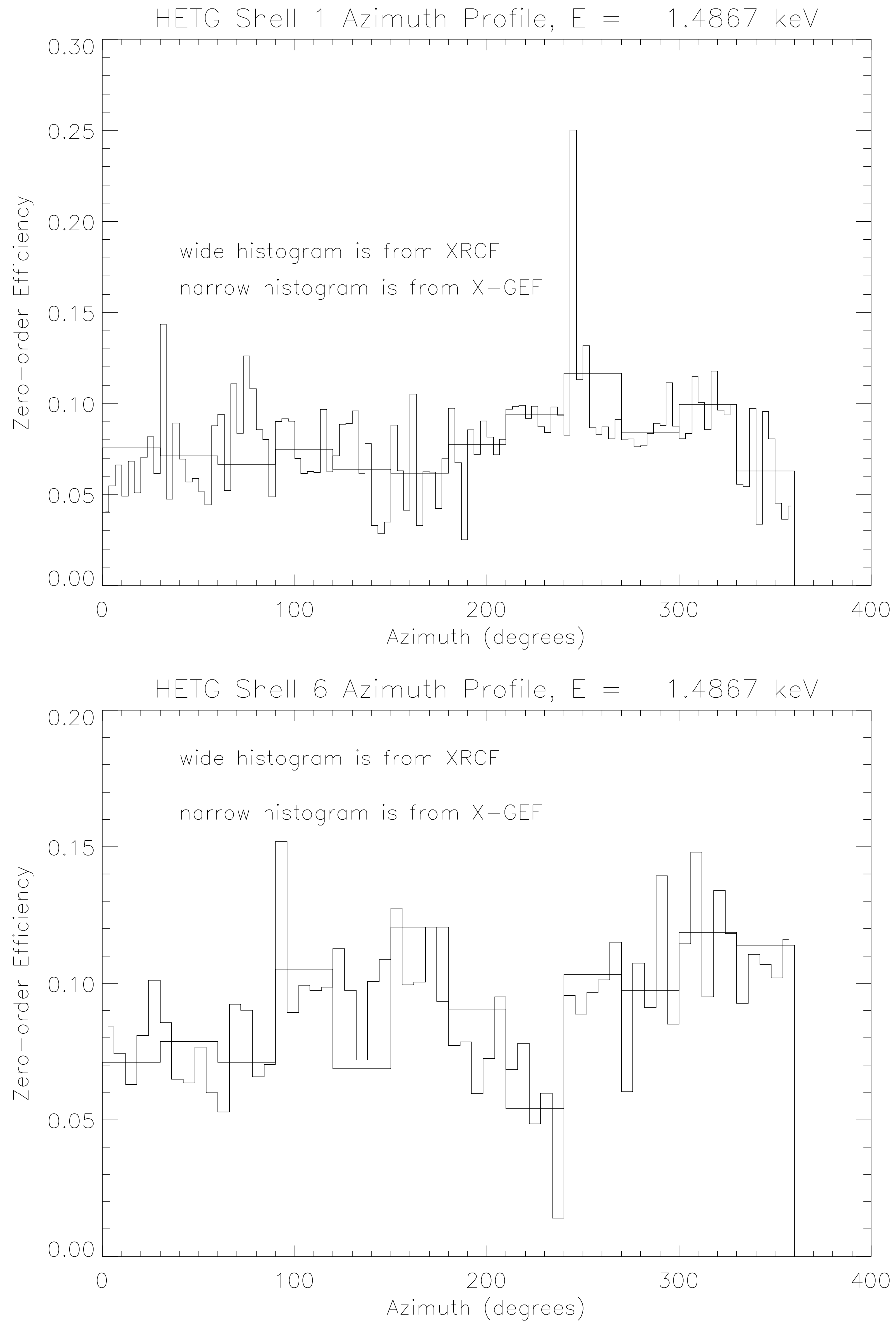

Figure 7.4: "Alignment" Test Results, Shells 1 and 6.

7.3 XRCF Source Characteristics

7.3.1 Source Spectra and Efficiency Measurements

Objective: Use the HSI images of the various source lines to create a grating-derived high resolution spectrum of the source.

During Phase I calibration the HSI detector[21] provided imaging capability at high event rates. Companion HSI exposures were taken for most of the FPC/SSD effective area tests expressly for the purpose of being able to see the dispersed images that the focal plane aperture was sampling. Through application of the grating equation these images also yield high-resolution spectra of the sources; Fe-L and Ti-K HRMA-grating-HSI spectra are shown in Figures 7.6 and 7.5.

The model spectra plotted in these figures consist of a Kramer continuum[17] plus a number of Gaussian lines with widths and intensities set to approximate the HSI-measured spectra. The line energies are fixed at tabulated values for identified lines. Comparison of the measured and modeled spectra has been done by eye, facilitated by the use of normalized cummulative plots, examples of which are shown at the bottom of Figures 7.6 and 7.5. Generally we have spectra of these lines with all three AXAF gratings. Because of the high spectral resolution of the HRMA-grating systems, the actual line widths and shapes can be resolved for many lines especially with the MEG and HEG gratings, *e.g*, the Fe-L and O-K lines here. Other lines, like the Ti-K lines shown in Figure 7.5, are narrower than the instrument resolution and are modeled as delta functions.

Source spectra from grating-HSI observations are available at:
`http://space.mit.edu/HETG/xrcf_sources/sources.html`

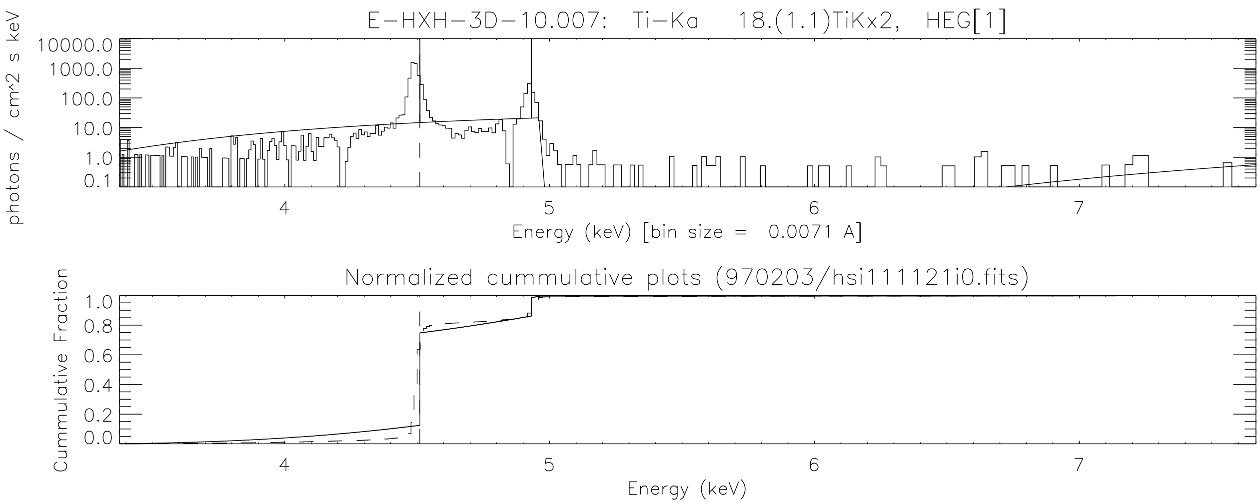

Figure 7.5: Ti-K line: HEG-HSI Spectrum and Model. *Top*: Measured Ti-K flux spectrum, calibrated by nominal parameters for the HRMA, HEG, and HSI; the Ti-Kα and Ti-Kβ lines are well resolved by the HEG dispersion. A model spectrum (solid) is plotted with the HEG-HSI-derived spectrum. *Bottom*: The data (dashed) and model (solid) spectra are compared by plotting the cummulative (integrated) normalized flux within the observed energy range. This plot provides a measured *vs.* modeled comparison of the relative line and continuum fluxes in spite of spectra differences, *e.g.*, here the measured and modeled line widths differ.

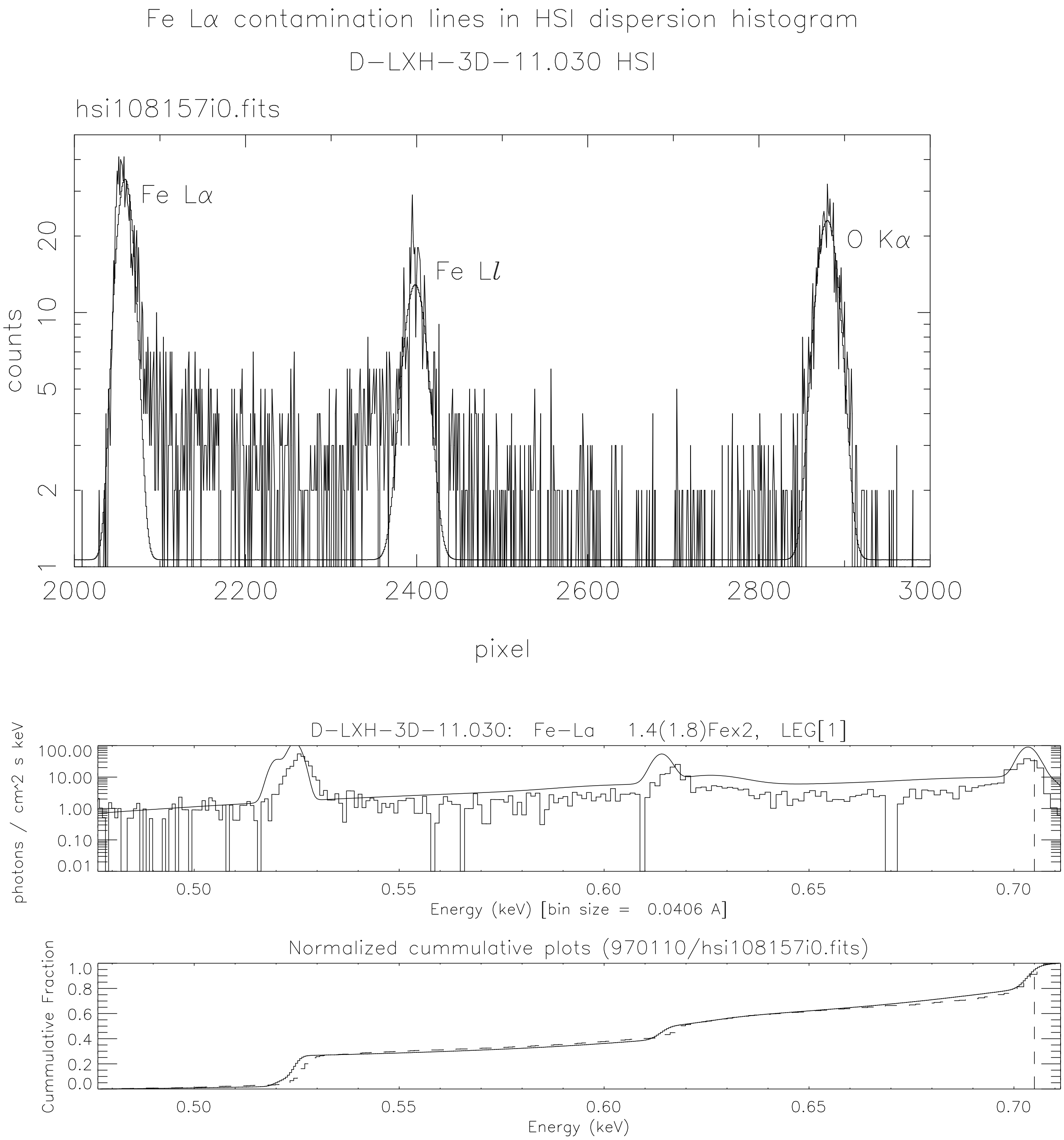

Figure 7.6: Fe-L line: LEG-HSI Spectrum and Model. *Top:* The High Speed Imager (HSI) positioned at the location of the LEG first-order for the Fe-Lα line; the detected events are binned by their location along the dispersion axis ($Y_{\rm xrcf}$). *Middle*: The counts spectrum is converted to a flux *vs.* energy spectrum using nominal calibration parameters for the HRMA, LEG, and HSI. A smooth model spectrum (see text) is plotted with the LEG-HSI spectrum. *Bottom*: The data (dashed) and model spectra (solid) are compared by plotting the cummulative (integrated) normalized flux within the observed energy range. This plot provides a comparison of the relative line (abrupt jumps) and continuum (sloping regions) fluxes in spite of data-model variations in line location, width, and overall normalization, *e.g.*, the small difference in measured *vs.* modeled energies due to inaccurate HSI position analysis.

7.3.2 Beam Uniformity Effects on Efficiency Measurements

Objective: Evaluate the effect of non-uniform illumination on "grating-in grating-out" efficiency measurements in Phase I and on relative efficiency measurements in Phase II.

7.4 Efficiency: Phase 1, EIPS Data

Objective: Derive the diffraction efficiency of the HEG and MEG using Phase I "grating-in grating-out" measurements made at fixed (non-scanned, non-continuum) energies.

Publication(s): Dewey *et al.* [18, 19]

7.4.1 Introduction and Overview

In Phase 1 of AXAF testing at the X-Ray Calibration Facility (XRCF), calibrated flow proportional counters (FPCs) and solid-state detectors (SSDs) were used both in the focal plane and as beam-normalization detectors. This use of similar detectors in the beam and focal plane combined with detailed fitting of their pulse-height spectra allowed accurate measurements of the HRMA absolute effective area with minimum influence of source and detector effects.

This paper describes the application of these detectors and fitting techniques to the analysis of effective area and efficiency measurements of the AXAF transmission gratings, the High Energy Transmission Grating (HETG) and the Low Energy Transmission Grating (LETG). Because of the high dispersion of these gratings the analysis must be refined. Key additional ingredients are the inclusion of detailed X-ray source models of the K and L lines based on companion High-Speed Imager (HSI) microchannel-plate data and corrections to the data based on high-fidelity ray-trace simulations.

The XRCF-measured efficiency values that result from these analyses have systematic errors estimated in the 10–20 % range. Within these errors the measurements agree with the pre-XRCF laboratory-based efficiency models of the AXAF grating diffraction efficiencies.

In this paper we report on progress towards the detailed analysis of the Phase 1 measurements which were designed to measure the grating effective area and efficiency using the FPC and SSD in the focal plane. First the general concepts of effective area and efficiency are reviewed; next the general XRCF Phase 1 measurement configuration is described including summary properties of the gratings and examples of the acquired data and their simplistic analysis. As will be demonstrated, analysis improvements require detailed knowledge of the source spectral composition which we derive from contemporary Phase 1 HRMA-grating-HSI observations of the source. Using the resulting spectra, accurate ray-traces of the system allow us to better understand the FPC/SSD data. Finally, analysis making use of the detailed source spectra and simulations is being carried out to derive accurate grating efficiency values and assess measurement errors.

7.4.2 Measurements and Example Data

In this paper we focus on the Phase 1 measurements that used the conventional electron impact X-ray source (EIPS) and that had either the FPC or SSD as the focal plane detector. There are of order 160 grating measurements of this kind and over 50 no-grating measurements of direct relevance.

The measurement process involved positioning the detector aperture D at one or more locations in the focal plane and acquiring simultaneous pulse-height spectra from the focal plane detector and the BNDs. We illustrate our analysis methods with example data sets taken with the Fe-L and Ti-K source lines, Table 7.1. Note that non-grating measurements were made as well (Grating = NONE) to allow a direct measurement of efficiency by dividing the grating-in by the grating-out effective areas.

Examples of the pulse-height spectra obtained for some of these Ti-K and Fe-L measurements are presented and described in Figures 7.7 and 7.8.

Table 7.1: XRCF Phase 1 Grating Effective Area Measurements at Ti-K and Fe-L. These measurements are used to illustrate the analysis. A two-mean-free-path source filter was used with these measurements to reduce above-line continuum. For the Ti-K measurements a $D = 2.0$ mm aperture was used; for the Fe-L measurements $D = 1.0$ mm. The BND detector FPC_HN was fully open for all measurements here except for '9.004 where it was closed to a nominal 36 mm diameter.

TRW-ID	Source	Shells	Grating	Orders	date/runid/iteration
E-IXF-3D-9.001	Ti-K,TiKx2	1,3,4,6	NONE	–	970203/111140i0
E-HXF-3D-10.001	"	4,6	HEG	1,2,3,0,-1,-2,-3	970203/111126i0–'i6
E-HXF-3D-10.002	"	1,3	MEG	1,2,3,0,-1,-2,-3	970203/111123i0–'i6
E-LXF-3D-9.004	"	1,3,4,6	LEG	1,-1	970203/111144i0,'i1
D-IXF-3D-11.003	Fe-L,Fex2	1,3	NONE	–	970110/108163i0
D-IXF-3D-11.004	"	4,6	NONE	–	970110/108164i0
D-HXF-3D-11.020	"	4,6	HEG	1,0,-1	970110/108161i0–'i2
D-HXF-3D-11.019	"	1,3	MEG	1,0,-1	970110/108162i0–'i2
D-LXF-3D-11.018	"	1,3,4,6	LEG	1,0,-1	970110/108165i0–'i2

7.4.3 Problems with Effective Area Analysis

A simple calculation of the measured optic effective area, Equation (7.2), from the pulse-height spectra would be:

$$OEA_D(E_{\rm line}, m) \quad = \quad \frac{R_{\rm fp}}{QE_{\rm fp}(E_{\rm line})} \Big/ \frac{R_{\rm BND}}{A_{\rm BND@HRMA} \ \times \ QE_{\rm BND}(E_{\rm line})} \qquad (7.5)$$

The subscript D indicates the measured optic effective area is into a finite focal plane aperture. The detector rates R are the counts per second in the pulse height "bumps" and the BND effective area $A_{\rm BND@HRMA}$ is the equivalent geometric area of the BND detector at the HRMA aperture and, together with the quantum efficiencies QE, provides the absolute calibration.

There is poor agreement between this simple analysis and our expectations especially for the dispersed $|m| = 1$ effective areas which are shown in Figure 7.9 and often appear lower than predicted. As the next sections will show, the source spectra often consist of multiple lines which are not resolved by the FPC detectors but are spatially separated in the focal plane by the grating diffraction. Thus, the BND is measuring several lines while the focal plane detector because of its finite aperture may be seeing only one or a fraction of the source lines. By measuring the source spectra and simulating the measurements we can implement improved analysis techniques.

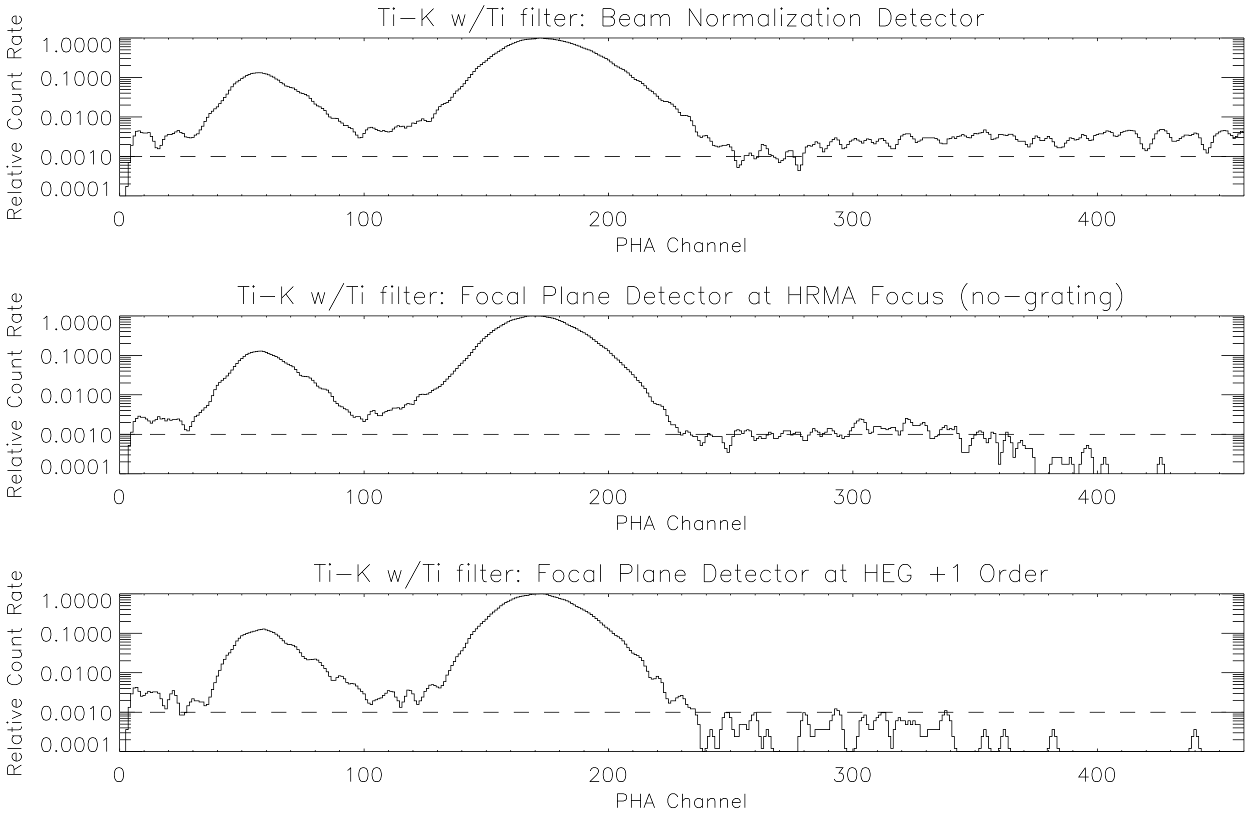

Figure 7.7: Examples of FPC Spectra for Ti-K Tests. The main features at this high energy, 4.51 keV, are the main photo-peak around channel 170 and the Ar escape peak around channel 60. *Top*: the spectrum seen by the BND FPC_HN directly viewing the source, continuum well-above the line energy is visible (channels 280 and up). *Middle*: the spectrum from FPC_X2 in the focal plane after the HRMA (no grating): the high-energy cutoff of the HRMA is visible in the continuum above channel 370. *Bottom*: the spectrum at the HEG $m = +1$ diffraction order – the detector here is seeing an essentially monochromatic input of the Ti-Kα line. To better show the differences in continuum, the histograms here have been smoothed and a dashed reference line at a relative rate of 10^{-3} has been included.

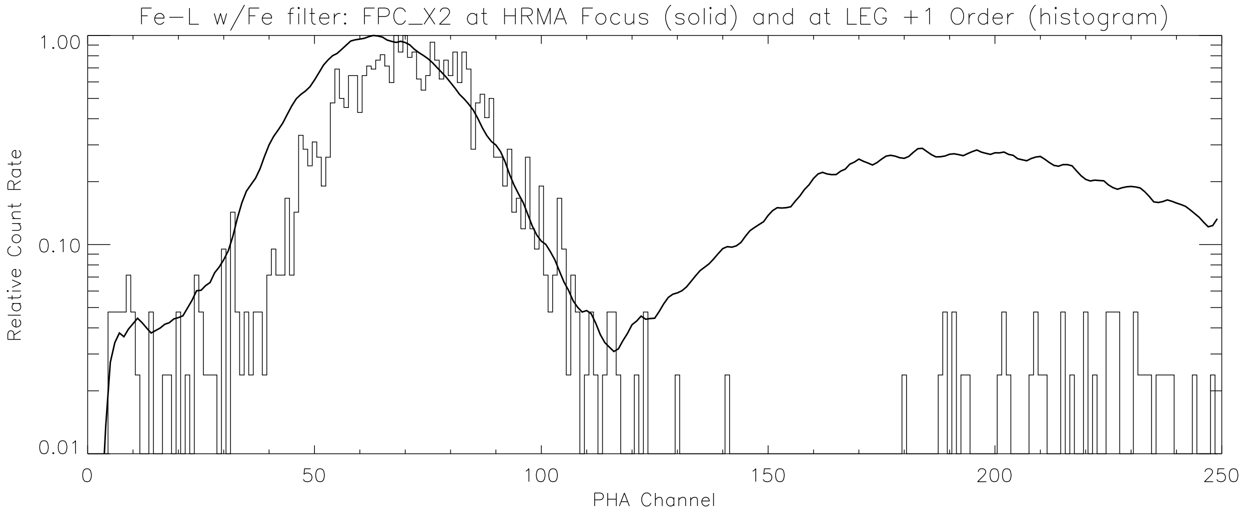

Figure 7.8: Examples of FPC Spectra for Fe-L Tests. The histogram-style curve shows the spectrum seen at the LEG $m = +1$ order: this is the monochromatic response to the 0.705 keV Fe-Lα line with some 2.1 keV $m = 3$ continuum counts around channel 220. The smoothed solid line shows the FPC_X2 spectrum at the HRMA focus without a grating (BND spectra are comparable): the "Fe-L bump" is visible peaking at channel 65 and continuum above the filter edge appears above channel 120. The extension of the bump to lower energies is due to the presence of unresolved lines, see Figure 7.6.

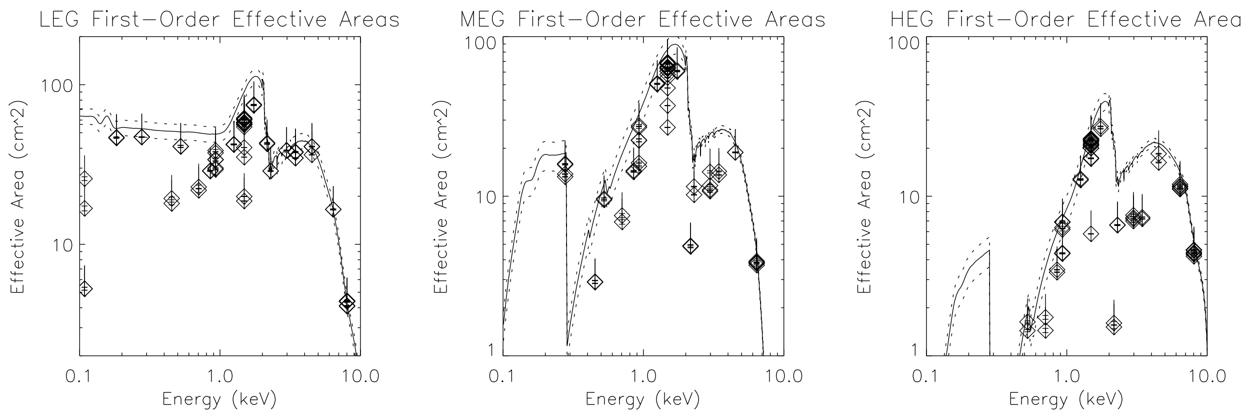

Figure 7.9: The problem with the standard effective area analysis: these plots show the grating first-order effective areas, calculated from simply extracted, uncorrected count rates, compared with model predictions[71]; these first-order effective areas are often measured low due to the presence of multiple and contaminating lines in the source spectrum.

7.4.4 Ray-trace Simulation of Phase 1 Measurements

It would be straight forward to use the grating equation and parameters of the measurement to decide which region of the detailed source spectrum will fall in the detector aperture D. While this approach works, it has difficulty including a variety of effects such as: broad lines that may overfill the aperture D, HRMA and grating PSF effects which blur the events, higher grating diffraction orders of higher-energy source photons, and the LETG support structure diffraction pattern. In the end it is best to accurately model the complete source-HRMA-grating-detector system to completely understand what the detector sees.

The "Model of AXAF Response to X-rays" simulation package[50] (MARX, 2.04) has been used as the engine to produce these simulations. Custom IDL code was produced to create modified MARX parameters for a given XRCF measurement, see Section refsec:marx.

Simulated focal plane images for the the diffracted Ti-K and Fe-L lines are shown in Figure 7.10. These simulations can be used to calculate several quantities relevant to the efficiency measurements being analyzed here:

- The encircled energy correction value $EE_{\rm corr}$ is the ratio of the number of all line events to the number of line events that fall in the aperture.
- The pulse-height distribution of events that are within the detector aperture can be formed and used to estimate what fraction of the measured count rate is due to a given line or feature in the sectrum.
- The simulations can also be used to assess the sensitivity of either of the above values to variations in the aperture placement in the focal plane.

The use of these simulation-derived values is described in the context of our efficiency analysis in the next section.

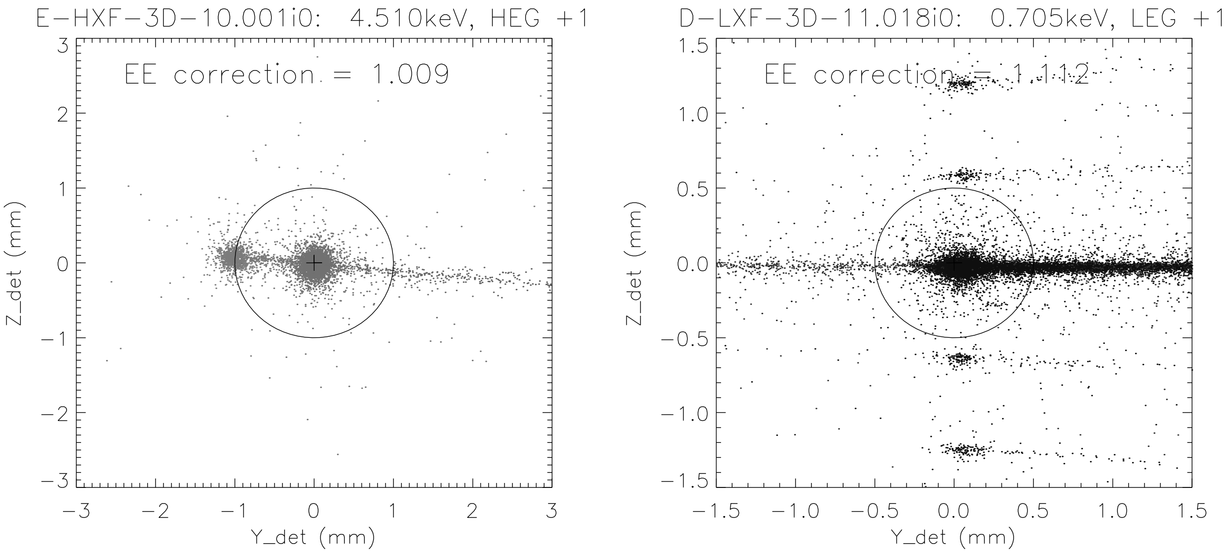

Figure 7.10: Ti-K and Fe-L simulated first-order images. In order to better undestand the FPC/SSD aperture measurements, the AXAF ray-trace package MARX was adapted to simulate XRCF measurements. These figures show the spatial distribution of events relative to the detector aperture used in the measurement. *Left*: The FPC aperture, 2 mm diameter circle, is centered on the Ti-Kα line; the Ti-Kβ line, at aperture edge, is partially included in the aperture and hence in the resulting pulse-height spectrum. The EE correction value of 1.009 indicates that very little of the Ti-Kα line flux is outside of the aperture. *Right*: Simulation of this Fe-Lα measurement clearly shows the LETG coarse-support diffraction pattern extending in the cross-dispersion direction, $Z_{\rm det}$. The bright continuum on the low-energy (right) side of the line is cut off by the Fe-L filter just above the line. The continuum streak to the high-energy side (left) of the Fe-Lα peak is actually 2.1 keV continuum that has been diffracted into the LEG +3 order.

7.4.5 Analysis Formalism

Now that we've seen the source and aperture effects, it is clear that the "failure" of the analysis specified by Equation (7.5) is due primarilly to inaccurate or contaminated values for the measured rates and the effects of the aperture. In addition, the best estimate of the effective flux at the HRMA entrance requires a detailed beam uniformity analysis and consideration of data from all of the BND detectors. These effects are included in the revised equations:

$$OEA_{2\pi}(E_{\rm line}, m) = EE_{\rm corr} \times OEA_D(E_{\rm line}, m) = EE_{\rm corr} \times \frac{\mathcal{R}_{\rm fp}}{QE_{\rm fp}(E_{\rm line})} \Big/ F_{\rm effective}(E_{\rm line}) \tag{7.6}$$

$$F_{\rm effective}(E_{\rm line}) = \left\langle \frac{BU_{\rm corr}\ \mathcal{R}_{\rm BND}}{A_{\rm BND@HRMA} \times QE_{\rm BND}(E_{\rm line})} \right\rangle_{\rm BNDs} \tag{7.7}$$

where the $\mathcal{R}$'s are the rate in a specific line or narrow energy region, an explicit encircled energy correction factor, $EE_{\rm corr}$, converts from the count rate measured in an aperture to the total focal plane rate, and the incident flux is now an average over the properly weighted ($BU_{\rm corr}$) BND measurements taking into account beam uniformity variations[62, 74].

The grating effective diffraction efficiency, Equation (1.5), is measured as the ratio of the optic effective area with the grating in place to the optic effective area without the grating (HRMA-only):

$$G^{\rm meas}_{\rm config}(E_{\rm line}, m) = \frac{OEA^{\rm g}_{2\pi}(E_{\rm line}, m)}{OEA^{\rm H}_{2\pi}(E_{\rm line})} \tag{7.8}$$

where the g superscript refers to grating-in measurement and the H superscript is a HRMA-only measurement.

7.4.6 Count Rate Corrections

In general pulse-height analysis is performed to provide measured focal plane and BND rates, R, in some, possibly broad, energy range. A "line-fraction-correction" L, can be defined for each pulse-height spectrum to convert this measured rate to an estimate of the rate in a line or narrow energy region: $\mathcal{R} = L \times R$. The value of L can be numerically determined from the simulation of a measurement as the ratio $\mathcal{R}_{\rm sim}/R_{\rm sim}$; this requires precise definitions of $R_{\rm sim}$ and $\mathcal{R}_{\rm sim}$, however.

To determine $R_{\rm sim}$ from a simulation, the analysis method itself must be faithfully modeled. In order to determine $\mathcal{R}_{\rm sim}$, that is the count rate in the line, the "line" must be defined. Because some lines are in fact naturally broad and continuum is present in the modelled spectra, it is convenient instead to talk of a spectral "feature"; here a useful and reasonable definition of the feature is "all photons in the range $E_{\rm line} \pm E_{\rm line}/100$" – thus continuum under the line is part of the feature as well.

Substituting $\mathcal{R} = L \times R$ into Equation (7.8), many of the terms will (exactly or very nearly) cancel leaving:

$$G_{\text{config}}(E_{\text{line}}, m) = \frac{EE^{g}_{\text{corr}}\ L^{g}_{\text{fp}}}{EE^{H}_{\text{corr}}\ L^{H}_{\text{fp}}} \times \frac{R^{g}_{\text{fp}}/(R^{g}_{\text{BND}}/A^{g}_{\text{BND@HRMA}})}{R^{H}_{\text{fp}}/(R^{H}_{\text{BND}}/A^{H}_{\text{BND@HRMA}})} \tag{7.9}$$

Thus, the simple count-rate based efficiency, the ratio on the right, is corrected for after-the-fact by simulation-derived parameters. This "feature-fraction" correction (the product $EE_{\text{corr}}\ L_{\text{fp}}$) can be calculated and applied to different pulse-height analysis methods.

The next sections describe our specific analysis efforts that implement this approach to more accurately calculate the measured grating efficiency. In all cases the EE_{corr} factor is derived from the ray-traces and post-applied. Two of the analysis methods (ROI and "counts-in-bump") have non-trivial L values, the third method ("counts-in-line") includes the source spectral information "upstream" of the pulse-height analysis and so has $L = 1$.

7.4.7 Region-of-interest (ROI) Analysis

The most simple pulse-height analysis method determines a count rate based on the total number of counts in a region of interest, for example the counts in channels 20 through 120 in the Fe-L spectra of Figure 7.8 may be summed. This has the advantage of simplicity and computational speed and robustness. Likewise the quantity R_{sim} can be generated with high accuracy for a coarse region of interest by counting all events in an energy range.

The very robustness of the ROI analysis points to its main defect: because the data are not evaluated with respect to any model there is no check that the assumed model is realistic (except perhaps when the ROI limits are viewed on the pulse-height histogram), errors in lines present, detector operation, continuum levels, etc. can all cause erroneous results without an indication of a "failure" of the assumptions.

For our purposes the ROI analysis with the corrections applied serves as an initial robust result and a sanity check and guide to the more complex and detailed fitting analyses, below. The results of the corrected ROI analysis are shown by the "x"s in Figures 7.13 and 7.14.

7.4.8 JMKMOD "counts-in-bump" Analysis

An improvement on the simple ROI analysis is the detailed pulse-height spectral fitting provided by the JMKMOD software[20, 75]. This software is an add-on package to the XSPEC[80] x-ray spectral fitting package and was created to model the XRCF FPC and SSD detectors. Figure 7.11 shows the application of the JMKMOD model to a Ti-K BND spectrum. Because these detectors cannot resolve the Kα and Kβ peaks, the fitting process is not able to reliably determine accurate count rates for the separate lines – rather the combined count rate in the Kα plus Kβ "bump" is determined.

Two main advantages of this fitting technique over a simple ROI analysis are: i) the measured data are fit by a model and therefore data quality and measurement assumptions are tested

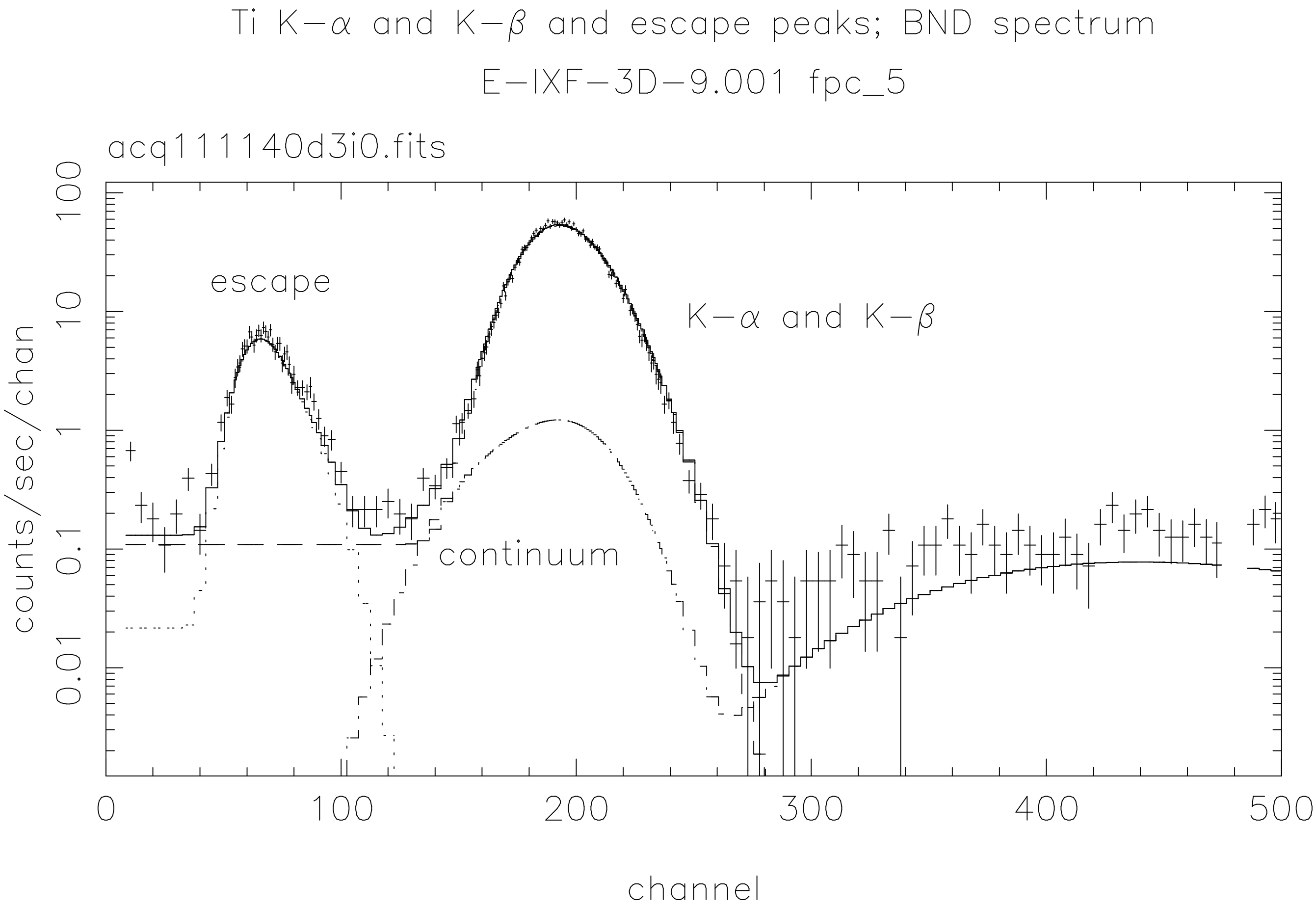

Figure 7.11: JMKMOD fit to Ti-K BND. Three of the components of the JMKMOD spectral model are highlighted here: the main Kα plus Kβ photo-peak, the Ar escape peak, and the broadband continuum generated by the source and given structure by the Ti source filter.

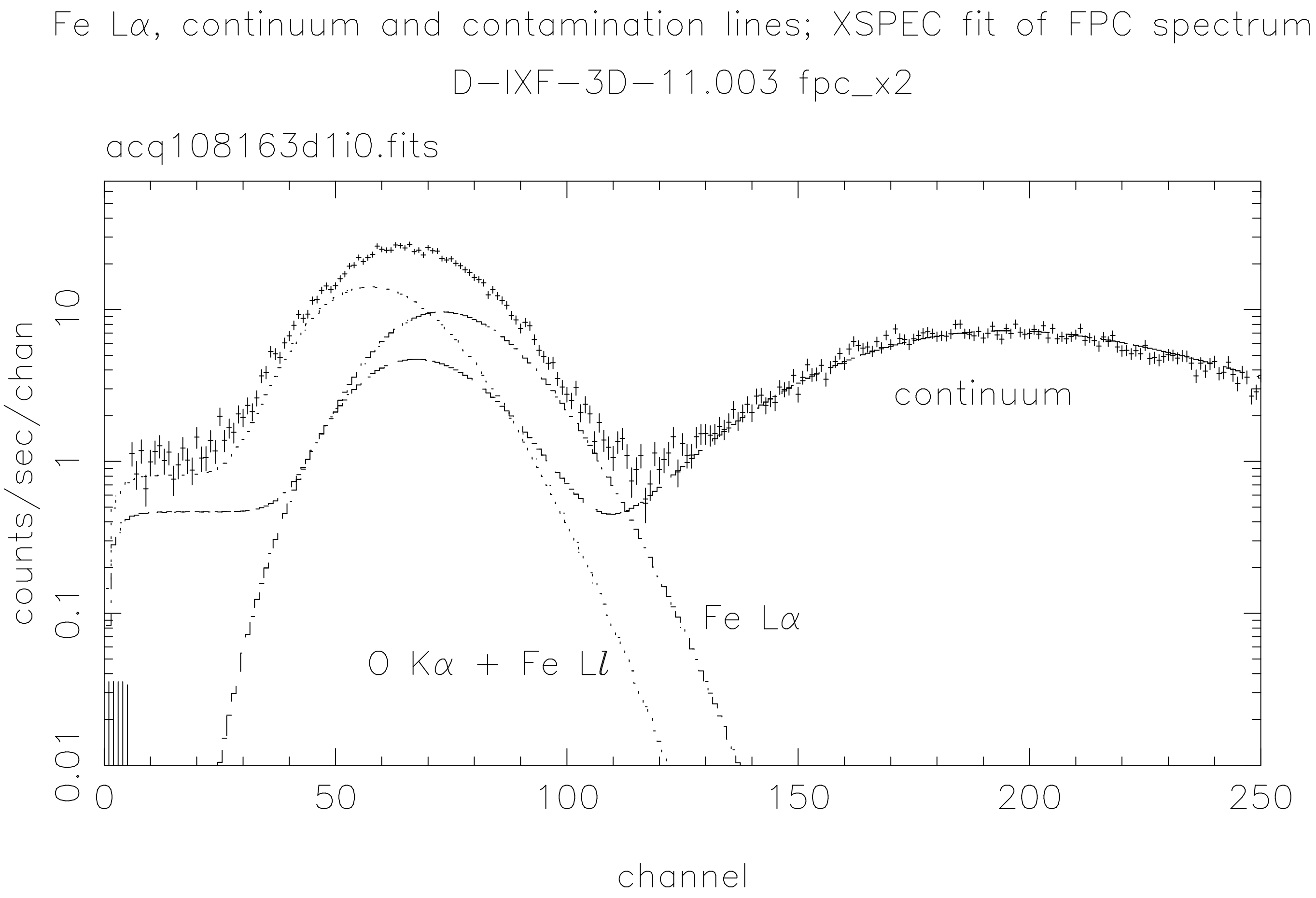

Figure 7.12: JMKMOD fit to Fe-L FPC_X2. In this "counts-in-line" analysis the three known source lines have had their relative intensities fixed based on the HSI-derived relative fluxes; the continuum component is allowed an independent normalization in the fit. The fit intensity of the Fe-Lα line is the rate in the line, that is $L = 1$ and $\mathcal{R} = R$. A good fit to the data indicates an agreement of the source model with the data to an accuracy allowed by the detector resolution and count statistics.

and ii) the continuum level in the spectrum is measured rather than depending on a modeled continuum.

The measured rate R is similar to the ROI rate but does not include a continuum contribution; this requires that slightly different values for the line fraction corrections L be applied in Equation (7.9). As a starting point, however, the efficiency results from this "counts-in-bump" analysis were corrected with the same correction as the ROI results and are shown in Figures 7.13 and 7.14 by the triangular symbols. As in the ROI case, the correction has the greatest effect on the efficiency of the L-lines of Mo, Ag, and Sn; its effect on the Ti-K HEG first-order efficiency is an increase of 9.3 %.

7.4.9 JMKMOD "counts-in-line" Analysis

Rather than applying the L line-fraction corrections to the rates in a region or bump, it is possible to fit the pulse-height spectra using as input a modeled source spectrum. Lines and features which are resolved in the spectrum can be fit with independent intensities; those that are poorly resolved must have their relative intensities fixed. This technique has the potential advantage over the "counts-in-bump" analysis in that the assumed model is directly tested against each pulse-height data set.

An example of a JMKMOD "counts-in-line" fit to a non-grating focal plane spectrum is shown in Figure 7.12. All three lines in the Fe-L spectrum, have had their relative intensities fixed based on the HSI counts spectrum, Figure 7.6, and modeled HSI, grating, HRMA, and FPC properties. The fit intensity of the Fe-Lα line is then directly the line rate, $\mathcal{R}$, *i.e.*, $L = 1$..

The only correction required to this analysis is the ratio $EE^{g}_{\rm corr}/EE^{H}_{\rm corr}$ which corrects for finite aperture effects; for LEG measurements this correction can be as much as a ≈ 10 % increase. For the dispersed orders of the broad low-energy lines (Be-K and B-K) this ratio must be calculated using an accurate source spectral line shape and source filter transmission curve.

The efficiency results of this "counts-in-line" analysis are shown by the square sysmbols in Figures 7.13 and 7.14.

7.4.10 Discussion

The agreement of the XRCF-measured efficiencies with the laboratory-measurement-based efficiency predictions shown in Figures 7.13 and reffig:megheg0 is a wonderful confirmation of the grating diffraction models and facet-by-facet laboratory measurements: taken on their own, these XRCF Phase 1 EIPS measurements do in general verify the laboratory-based efficiency models at the 10–20 % level in most energy regions.

These analyses are nearly complete, what remains is to study and assign systematic errors to these measurements, *e.g.*, by obtaining error estimates for the HSI-derived source spectra and folding them through the analysis methods. Other potentially large systematic errors yet to be accounted for in the analyses are thought to originate in the FPC detectors in ways that are difficult to account for in the detector models. Apparently subtle effects, such as a bowing outward of the FPC windows due to internal gas pressure and obscuration and reflection of focussed focal plane light by the supporting wire mesh, are calculated to affect HRMA measurements at levels below a percent[39]. However, the former of these effects can be more important at the lowest energies where the detectors and windows are more optically thick: the window bowing alters the effective thickness and location of the window seen by incoming photons, and low energy photons penetrate to smaller depths in the detector. One of the next major challenges is to understand these detector effects and to account for them in the refined spectral modelling process (§6) in order to determine more accurate fluxes at the telescope aperture and focal plane.

In the case of the LETG, which is designed to operate at wavelengths as long as 170 Å (0.07 keV), the lowest energies available for efficiency and effective area measurements—provided by the B (183 eV) and Be (108 eV) EIPS—pose special difficulties because of the very low QE of the XRCF detectors in this regime. Here, detector background and counting statistics can be significant sources of error; during the Be tests for example, the HRMA BND count rates were generally too low to be of any quantitative use for beam monitoring and normalization, and the "Building 500" FPC detector provides the only means of determining the beam flux.

In the near future, these analysis techniques will be applied to the Phase 1 measurements made with a monochromator as the source in place of the EIPS source. The spectral analysis may in general be cleaner (no closely spaced L-lines for example), however the monochromators do

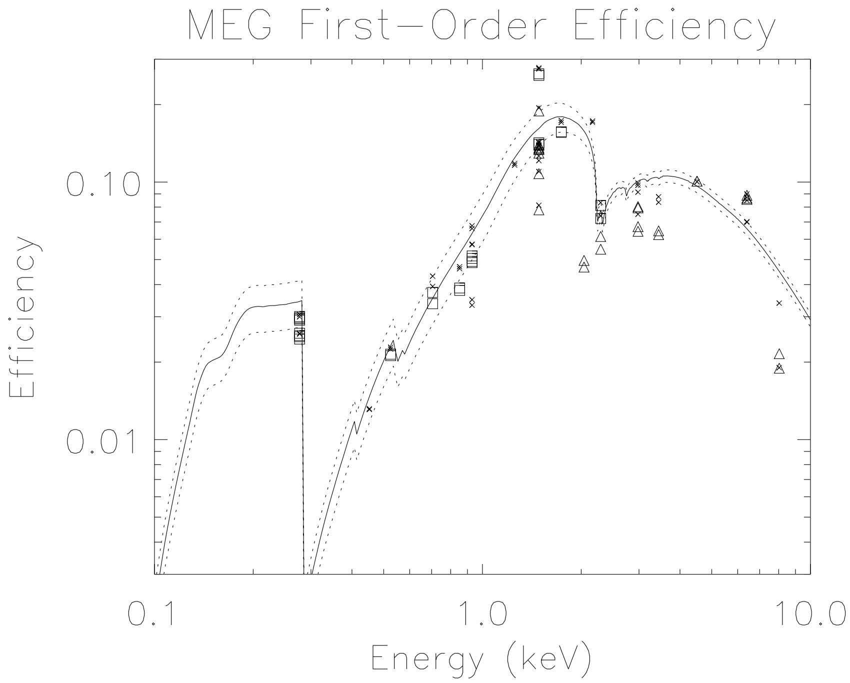

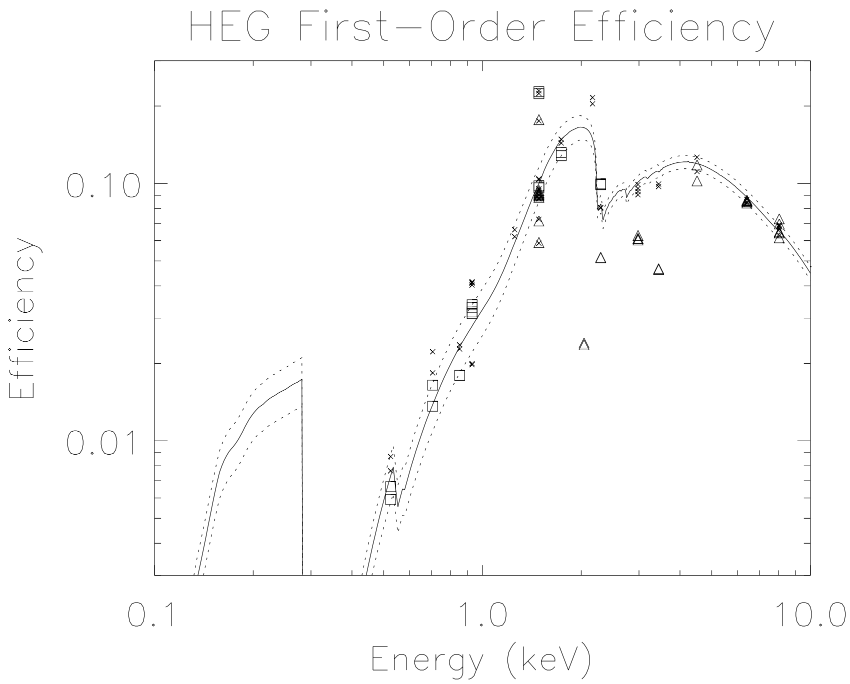

Figure 7.13: Phase 1 XRCF MEG and HEG Efficiencies: 1st order. The measured first-order efficiencies are compared with the pre-XRCF model predictions, based on facet-by-facet laboratory measurements. The plotting symbols indicate the pulse-height analysis methods: "x"s are from region of interest rates (Section 7.4.7), triangles are from "counts-in-bump" rates (Section 7.4.8), and the squares are based on "counts-in-line" rates (Section 7.4.9). Statistical errors are generally less than 3 %; understanding and reducing the systematic errors, estimated to be of order 10–20 %, is an ongoing effort.

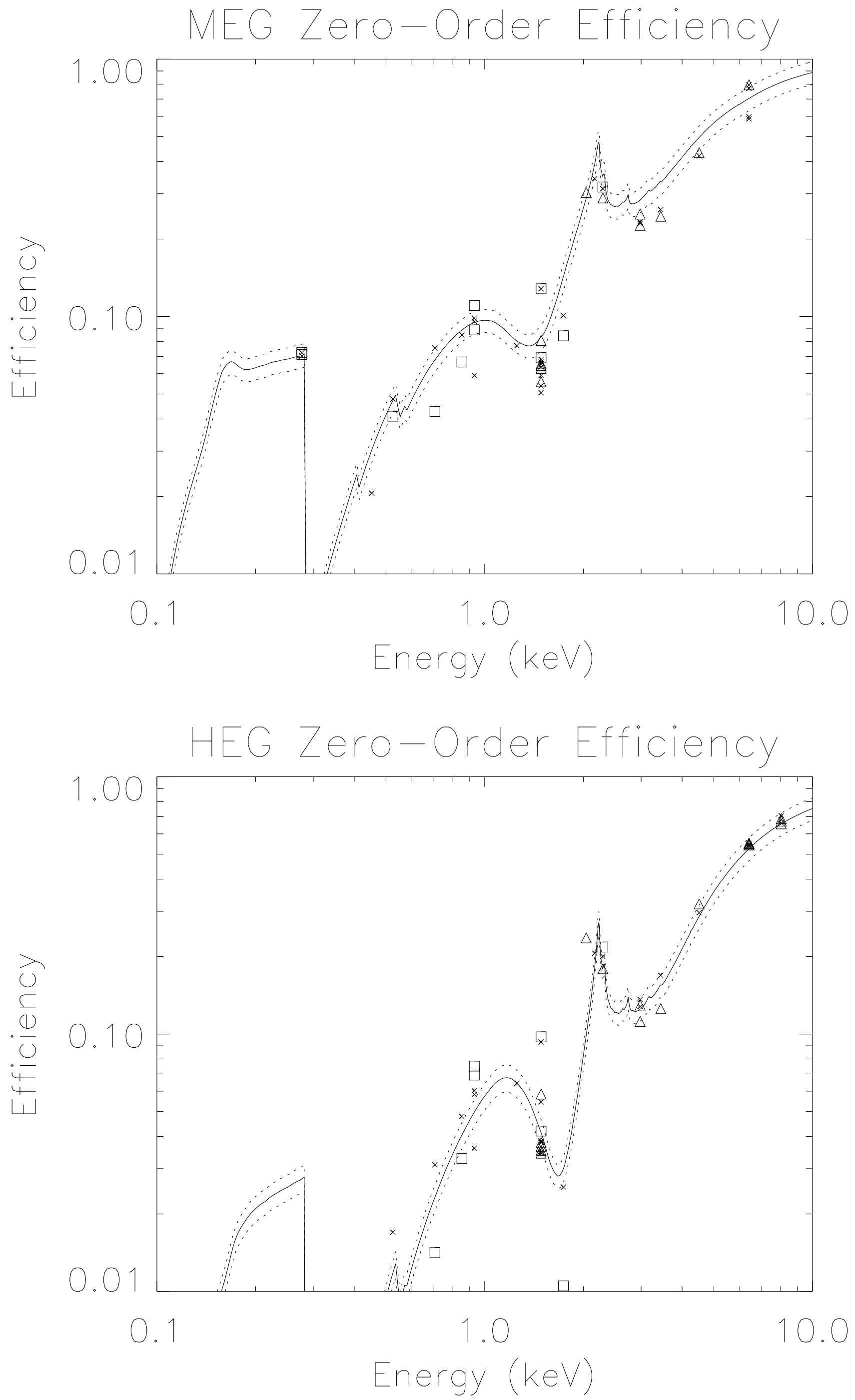

Figure 7.14: Phase 1 XRCF MEG and HEG Efficiencies: 0 order. The measured zero-order efficiencies are compared with the pre-XRCF model predictions, based on facet-by-facet laboratory measurements. The plotting symbols indicate the pulse-height analysis methods: "x"s are from region of interest rates (Section 7.4.7), triangles are from "counts-in-bump" rates (Section 7.4.8), and the squares are based on "counts-in-line" rates (Section 7.4.9). Statistical errors are generally less than 3 %; understanding and reducing the systematic errors, estimated to be of order 10–20 %, is an ongoing effort.

have substantial beam uniformity variations[74] that must be dealt with.

The ultimate target of all our analyses is to produce grating efficiency models that are of sufficient accuracy that they are not a dominant source of uncertainty in the flight HRMA+grating+detector optical system. When all known sources of systematic error have been included in the modelling processes and flux determinations, it is hoped that the final uncertainties in the individual grating efficiency measurements will be as low as 2-3 %. At this level, the XRCF measurements will be capable of providing quite stringent tests of the grating efficiency models.

To-do:

- create ffs_dkr.rdb to have accurate corrections for dk's ratio values.
- Pete to analyze D-LXF-3D-12.003a (in place of '12.003)
- Pete: "too much continuum in XSPEC fits to Fe-L,O-K, Si-K, Ti-L contnorm in 109286, 109287?
- CMDB mods for Be-K D-LXF-3D-12.003a : w/filter and 10 mm aperture and B-K 22.043 (10 mm aperture), re-MARX simulate, new ff corrections
- Improve Si-K line source model, what is 2.03 keV line in Si-K spectra? I think the Zr filter lets this line appear in FPC measurements...: Brad suggests it is W line!
- dd modify his Fe-K Mn filter to include the little lead in it...(is this the one?
- re-do HSI spectral analysis using new HRMA EA curves: check Mo line for any HRMA-induced "lines"?
- Two-step source line intensity process: use HSI spectra to decide what lines are present and then use SSD spectra to set relative normalizations where possible, e.g., Ti-K Ka and Kb.
- include support grid effect in MARX simulations
- resimulate (eae_sim) with new released MARX version
- include DeltaZ aperture errors in feature_fraction error estimate
- Make page or two of HSI source spectra plots...
- Make a no-grating BND simulation too...
- Double check the HRMA 1,3 - 4,6 area fractions used to convert shell measurements to other shell combinations
- Pete's Be and B analysis: broad line over fills aperture.
- Make sure released rdb files have N and S 's in column def.s
- Create simulated .pha files from MARX to check analysis techniques.
- Analyze the Phase 1 monochromator data - easier and harder!

7.5 Efficiency: Phase 1, Monochromator Data

Objective: Derive efficiencies of the HEG and MEG using the monochromator scan data.

7.6 Efficiency: ACIS-2C Data

Objective: Derive the diffraction efficiency of the HEG or MEG using ACIS-2C "grating-in grating-out" measurements made at fixed (non-scanned, non-continuum) energies.

To-do:
Create automated analysis s/w similar to the Phase I Fixed energy analysis.
Generalize the rdb results table (eae_weffics.rdb) to include these '2C results, etc.

7.7 Absolute Effective Area with ACIS-S

Objective: Derive the HETGS(ACIS-S) effective area and compare it to HRMA, HETG, and ACIS-S measurements and predictions. ACIS effects that must be understood include: pileup, grade effects, exposure times.
Publication(s): Schulz *et al.* [71]

XRCF measurements of the flight AXAF High Energy Transmission Grating Spectrometer throughput were used to determine absolute effective areas. The results are compared with component models of the HRMA, HETG, and the ACIS-S. The comparison provides an independent view on HETG efficiencies as well as the detector efficiencies along the dispersion direction. As detailed in Table 5.8, three source configurations were used to measure the absolute HETGS effective area: EIPS, DCM, HIREFS. Of these the most extensive data set is from the DCM and its analysis and results are described.

Using the XRCF double crystal monochromator measurements in the range from 0.9 to 8.7 keV, the effective areas in the 1st order MEG were determined with an accuracy of better than 10%, in the 1st order HEG better than 15% throughout most of the energy range. This is within the goal set for the XRCF measurements to refine state of the art composite component model predictions, which in future will allow us to draw conclusions on the in-flight HETGS absolute effective area.

For a detailed description of ACIS we refer to the ACIS Team Calibration Report[1] and publications [5]. Briefly, the CCD array, illustrated in Figure 1.2, consists of two different types of CCDs: four front illuminated devices (FI) and two back illuminated devices (BI). These are arranged in a linear array and designated S0 to S5 from left to right in the Figure, from -Y to +Y in AXAF coordinates. S1 and S3 are the two BI devices. The position of the 0th order image, is marked in the Figure by the small black box, is on the back-illuminated device S3. This will also be the a launch-locked focal position for AXAF.

In this article we focus on measurements performed with the Double Crystal Monochromator (DCM), in which an energy range of 0.9 to 8.7 keV was covered. During this phase "H" of XRCF testing the ACIS-S array was the only flight detector in the focal plane for these set of measurements. The setup also included several Beam Normalization Detectors (BNDs), here we make use of the four BNDs positioned at the HRMA entrance plane.

7.7.1 Approach and Data Sets

7.7.1.1 Effective Area Measurement Approach

The measured effective area of an HETG order is the ratio of the count rate of that particular order received by the CCD array to the incident source flux at the HRMA entrance plane:

$$A_{meas}(E_{DCM}, m, \text{mode}) = \frac{\text{focal plane counts/s in order}}{\text{source flux atHRMA}} \quad [\frac{\text{counts/s}}{\text{photons/cm}^2\text{s}} = \text{cm}^2 \frac{\text{counts}}{\text{photon}}] \tag{7.10}$$

TRW-ID H-HAS-EA-	DCM crystal	Energy eV	Increment eV	steps	~cts/step
8.001	TAP	950	50	5	41000
8.002		1200	50	5	45000
8.003		1400	30	11	28000
8.004		1860	20	8	35000
8.005		2050	30	11	12000
8.006	Ge1	2500	150	11	18000
8.007		4000	200	6	18000
8.008		5000	250	9	28000
8.009		7200	500	4	23000

Table 7.2: List of HETGS effective area measurements with the DCM at XRCF. The energies listed are the start energies of each set. Exposure times varied between ~1000 and 2000 s for each energy.

This measured quantity thus depends on the specific analysis methods, such as event identification in the detector array as well as the flux determination method in the BNDs. The uncertainty of the result involves the statistical error of the determined count rates and any statistical and systematic errors from each of the four the BND fits. Another systematic uncertainty is present in the determination of the subassembly grating efficiency measurements shown in figure 7.2. Those are not included in the uncertainty of the XRCF data. In the higher orders the uncertainty in the measured effective area is dominated by counting statistics.

7.7.1.2 DCM Measurement Set

The energy scans taken with the DCM include a total of 70 steps; Table 7.2 summarizes these measurements. The measurements were divided into 9 blocks with different increments. The first 2 blocks consisted of 8 steps of 50 eV starting from 950 eV, the next 3 blocks covered an energy range between 1.4 and and 2.4 keV in 30 eV steps, followed by 150 eV steps until 4 keV. The increments were then increased up to 500 eV until 8.7 keV.

In order to get sufficient photon counting statistics in the diffracted orders, the high voltage of the tungsten source was steadily increased above 2.5 keV. The total number of counts for each energy step then varied between 1.1×10^4 to 4.5×10^4 counts. Figure 7.15 shows a typical measurement, which included 11 steps between 2.5 and 4.0 keV. The detector was moved 40 mm out of focus along the optical axis towards the HRMA in order to spread the focal image over as many detector pixels as possible. The dispersed images appear as rings reflecting the two outer mirror shells in the MEG, the two inner shells (and therefore smaller rings) for the HEG. Each order appears as a sequence of rings separated by the dispersed increment of 150 eV.

The analysis uses DCM measurements only, that is energies above 950 eV. This has one particular shortcoming for the calibration of the HETGS, which is that except for some data from the S0 device in the HEG +1st order, the two outer CCDs S0 and S5 are not in the dispersion range of the bright 1st orders.

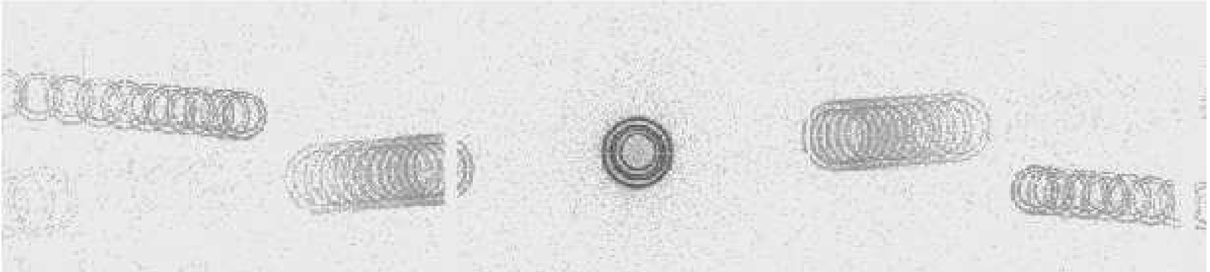

Figure 7.15: HETGS image of measurement H-HAS-EA-8.006. The image includes MEG and HEG 1st order. Each order consists of 11 steps 150 eV apart. In this closeup view the chip gap between S2 and S3 is seen to the left of zero order cutting through the MEG diffracted rings; the S3-S4 gap is seen at far right cutting through the HEG rings.

7.7.1.3 Beam Normalization Data

In order to monitor the source flux illuminating the telescope a system of beam nomalization detectors were positioned in the facility[79]. One set was positioned close to the X-ray source, and one set at the entrance plane of the HRMA. For our analysis we are primarily interested n the flux at the HRMA entrance plane; the beam is quite large at that stage, therefore we need to determine the source flux at various position within the beam in order to compensate for non-uniformities in the beam. Four gas flow proportional counters (FPCs) were placed at +Z (FPC-T, top), -Z (FPC-B, bottom), -Y (FPC-N, north), and at +Y (FPC-S, south) od the HRMA aperture at a radial distance of slightly larger than the outer shell radius. The denominations 'top', 'bottom', 'north', and 'south' reflect the actual orientation within the test chamber at XRCF. The analysis of the FPC data for the DCM scans has been performed by the AXAF project scientist team at MSFC. For details of this analysis we refer to the AXAF Project Science Calibration Report and references therein ([64, 74]).

Figure 7.16 shows the flux at the four BNDs during each of the 70 energy steps of the DCM separated into a diagram for lower and for higher energies. The behaviour of the beam flux in the two energy domains is quite different. The reason for this lies in the DCM and its X-ray source. As described above, between 1.3-2.0 keV three prominent lines appear in the spectrum. The intrinsic optical properties of the DCM crucially imprint onto the uniformity of the beam: the lines will appear at only certain angles, which translate to different locations at the HRMA entrance plane. Hence the lines result in strong non-uniformities. The DCM then was tuned in a way that the major gradient in line flux appeared between FPC-S and FPC-N, while the other two remained in reasonable aggreement, i.e only one gradient appeared across the beam. At higher energies the four monitors are well in aggreement, major discontinuities in the flux versus energy flunction appeared only when the crystal type in the DCM was changed.

7.7.2 ACIS-S/HETG Data Reduction

The event lists used for this analysis were provided by the ACIS team at Penn State University, who separated the telemetry data stream into the proper test segments and performed the basic processing of CCD data in terms of bias subtraction and ACIS flight event grading. Starting from the resulting event lists, the further reduction of the data involves several more steps. First of all, the test segments (first column in table 7.2) still contain a number of energies depending on the the number of DCM steps performed. The single energy events were extracted and written into separate energy lists with a well defined exposure time. Since in this analysis we restrict the event selection to one single grade set, we have to re-grade the data into the sum of ASCA grades 0,2,3,4,6, which are basically a subset of the 255 ACIS flight grades. One then spatially extracts each order by using the grating dispersion relation

$$sin(\theta) = \frac{m\lambda}{p} \tag{7.11}$$

where m is the order of diffraction (an integer 0, $\pm 1, \pm 2$, ...), p is the grating period and θ is the dispersion angle. Knowledge of the dispersion axis and the grating-to-detector distance, the Rowland distance, allows a conversion of the angle θ to a physical location on the detector.

Each extracted order has a pulse height spectrum from its location on a particlar CCD. After applying the specific gain correction for each device, ideally we then should see one single peak with a FWHM of the spectral resolution of the device at that particular energy. In reality this is not the case for many reasons and it is crucial to select a proper PHA region-of-interest in order to select all the counts that are from the line source only. These considerations are detailed in the pileup section below.

A further correction comes to the data from flux losses when a single order's image intersects a gap between CCD devices; an example of this is seen in Figure 7.15. The effect is quite prominent when it occurs and the probability that it effects an order near gaps is high since the diameter of an order image is more then 5 mm in the MEG and about half that size in the HEG at 40 mm intrafocal position. Flux losses sometimes amounted up to 45% in the case of the HEG. Therefore every time an image partially hit a gap (the gap is about 0.43 mm wide) we calculated the portion of the rings (note that at lower energies the image always had 2 rings from 2 contributing shells) and applied this portion as a correction factor to the flux. The method, however, has its flaws, *e.g.* when the gap was between a FI and BI device, which in the low and in the high energy domain have significantly different quantum efficiencies. However, the systematic errors introduced in these domains were less than 1% and thus disregarded.

7.7.3 Pileup in the Data Sets

7.7.3.1 Pileup Basics

All the effective area measurements performed at XRCF were primarily optimized for flux in the higher order in order to get sufficient statistics. Naturally this will cause pileup in the CCD detector array at least in zero as well as in some of the lower orders.

A recent analysis by the ASC ACIS team, Allen *et al.* 1998[3], showed that pileup affects the data in different ways and also shows differently in front- and back-illuminated CCDs. Pileup basically occurs when two or more photons incidently hit the same 3x3 detection cell. Two photons of the same energy would be detected as one event at twice the pulse height of a single photon, three photon at three times the pulse height and so on. Naturally this process has to be flux dependent. At very high fluxes will also allow two or more photons only partially contained within the 3x3 detection cell, which will then cause an enhanced background in between the main and pileup peaks.

In this respect it is more appropriate to think in terms of "fluences" rather than fluxes. Fluence descibes the incident photon density, i.e how many photons strike the CCD within one frametime per unit area, i.e. "ph/s/cm^2" or "ph/s/pix^2".

Higher fluences cause events to overlap more often, which then causes the detection algorithm to issign a higher number grade. This effect is called grade migration and causes a systematic depletion of standard grades, here the ASCA grade set 0,2,3,4,and 6. This migration is likely to be only effective at energies above $\sim$ 3 or 4 keV, when the sizes of charge clouds increase significanty.

Grade migration may not be the only effect of overlapping charge clouds. In the case when a very large charge cloud created by a high energy photon overlaps with a "normal" single or double pixel event, the 3x3 detection cell algorthm may not be able to detect any event anymore. In this case the charge would is lost.

7.7.3.2 Demonstration: the Zero-order Data

Zero-order data sets were not designed for effective area analysis because in order to get sufficient statistics in the higher orders, the source flux had to be high, especially at high energies. Therefore the zero order data will be entirely dominated by pileup effects in the CCD. They thus serve as useful pileup example.

The simplest way to identify pileup is to determine higher order pileup peaks in the pulse height spectrum. For energies below 3 keV it is possible to detect higher order pulse heights corresponding to up to 4 photons hitting the same event detection cell. The corresponding number of counts is then summed up and added back to the single photon count rate. The left diagram of figure 7.17 already includes that summation. Clearly above about 3 keV this procedure starts to fail because higher order pulse heights fall beyond the maximum pulse height channels. Therefore we observe a large drop in the measured effective area. In a first attempt to estimate the amount of piled-up photons we fit the ratio of the non-piled-up fraction to the measured piled-up fraction in the range 0.9 to 2.5 keV. In this range we were able to recover piled-up photons for up to 4 photons hitting an single detection cell. This could be done by a power law of index 0.27. We extrapolated this function into the high energy range and added that flux to the count rate above 2.5 keV. We also had to take in account that the source flux above 2.5 keV increased by a factor of 8 and scaled that function simply by that increase. Since pile-up is actually a stochastic process we could have also estimated the missing higher order counts out of a poisson distribution. In any case the resulting area was still short of the expectation by up to 45%.

Following the method to correct for grade migration as descibed by Allen *et al.* 1998 the grade distributions of all measurements above 3 keV were compared to the ones obserbed during subassembly analysis, i.e. data that were evidently free of migration effects. This results in another energy dependent correction factor. We thus calculated the grade migration correction factor for our data sets applied it to the data. Again the result above 6 keV was still short by about 20%. Allen *et al.* 1998 also apply a correction for lost charge and indetected events. Above 6 keV simply applied those correction factors from table 1 in [3] for the case of S3. The result can be seen in the right handed diagram of figure 7.17. The area now seem to fit the expectation, although a clear overcorrection is visible. However, we have to emphasize, since we did not in particular detemine the lost charge correction for our own data sets, the result is merely an estimation. It however demonstrates that those corrections applied by [3] are indeed necessary and in a reasonable order of magnitude. The applied corrections induce additional systematic errors to the data, which are *not* reflected in the error bars in the right handed diagram of figure 7.17.

7.7.3.3 Pileup in diffracted orders

The quantitative evaluation of pileup levels in the diffracted orders is still under investigation. The expected pileup level is low in all orders, however there are severall aspects to consider. For example, one major obstacle is, that at energies below 2 keV the first orders in HEG and MEG spatially mix with higher orders of the W lines generated by the DCM. For energies around 1 keV this emission interferes with the first pileup peak in the pulse height spectra.

Another problem is introduced by the design of the measurements at higher energies. In order to avoid overlaps of MEH and HEG images, the out-of-focus distance of originally 40 mm was gradually reduced with increasing incident photon energy. This hasd the effect that although flux stays constant, the fluence, i.e flux per unit area, increases. Therefore grade migration and charge loss effects will appear in the first order images. In addition that eefect is more likely to affect HEG orders, simply because of the smaller image size.

7.7.4 Effective Area Results

7.7.4.1 Zero-order Effective Area

The treatment of the effective area measurements for the zero order is in different from the ones for 1st and higher orders. In addition to the high pileup discussed above, we are not able to separate the MEG and HEG incident flux throughout the entire energy band. This is because in order to avoid any confusion of the higher order image rings with each other, the detector array was gradually moved back into the focal plane above 2.5 keV. Figure 7.15 shows the zero order image as it appeared beween 2.5 and 4.0 keV. The detector here was already moved back from 40 mm out of focus to 20 mm. It is clear that a separation of the inner two rings from the outer ones, in perticluar separating the images of mirror shells 3 and 4, would already introduce a significant systematic uncertainty. Above 4.0 keV, where the out-of-focus position was 10 mm and less, the separation of the inner rings would have become impossible.

We can use the zero order data in the low energy domain in order to fine tune the beam normalization in the range between 1.3 and 2.5 keV.

The top diagram in figure 7.16 shows quite a strong gradient between FPC-S and FPC-N flux, indicating strong beam non-uniformities. In the range 2.0 - 2.5 keV the FPC-N, however, shows an unsually large drop in flux. In order to minimize these effect on the analysis of the higher orders, we attached constant weights to each of the normalization fluxes in the range between 1.3 and 2.5 keV. Then we simply tuned those weights for each detector until the data in this range matched the values just below 1.3 and just above 2.5 keV. The result is shown in the left diagram of fig 7.17. For the other portions of the energy band, the normalization flux was simply the average over all four BNDs. Below 1.3 keV we observed an agreement with the expectation of better than 5%, between 1.3 and 2.0 keV the uncertainty is determined by the scatter induced by the BND uncertainties and thus can reach 30%; between 2.0 and 3.0 keV it is again near 5%.

7.7.4.2 Plus-Minus Order Asymetry

Figure 7.18 shows the +1 to -1 order ratio for HEG as detected by ACIS-S. The plot shows significant (up to 35%) departures from unity. Based on other measurements, grating asymmetry is not expected to account for the structure seen in here. Thus, these arise from variations within the detector. The jumps seen at 1.7 keV and 2.9 keV coincide with points at which one of the orders traverses a boundary between a frontside-illuminated (FI) and a backside-illuminated (BI) device. Between these energies, the +1 and -1 orders are both captured on FI chips, but outside that range one order falls on a BI chip, the other falls on a FI chip. It is clear that this strong residual structure, due to the detector, will complicate interpretation of the higher order ratios in Section 7.10. It is worth remembering that in the present analysis the quantum efficiency functions were not yet avaliable for each device rather templates were used for each CCD type. Thus, these kinds of chip-to-chip discontinuities are to be expected.

7.7.4.3 1st and 3rd order effective areas for the MEG

The MEG is optimized to supress efficiency in even orders. In the following we do not present results for any even MEG order. The top diagram of figure 7.2 shows the the subassembly expectation for the sum of the positive and negative 1st and 3rd MEG orders, i.e. in order to apply to single orders one has do divide these values in half. Considering the fact that efficiencies for single 3rd orders are a factor 10 to 20 lower than 0 order efficiencies we should not expect a significant contribution from pile up effects. In the 1st order single side efficiencies, however, we do have to expect a similar amount of piled-up photons at energies below 2.2 keV as we observed in 0th order, since the efficiencies are of comparable magnitude. At higher energies the efficiencies are between a factor 5 and 15 lower, which reduces the probability of pile-up accordingly. In the following we therefore will not apply any other correction than to add all the counts found in detected higher pile up orders in the pulse height spectra.

Figure 7.19 shows the effective areas determined for the -1st (top, m1) and +1st (bottom, p1) order of the MEG. All data points are confined within 3 CCDs, S2-4. The -1st order covers S2 for all energies below 4.2 keV, and S3 for all higher energies, the 1st order covers S4 for energies below 1.5 keV, and again S3 for all the higher energies. In both orders it is clear that measurements around the tungsten Mα line at 1.75 keV (width $\sim$ 150 eV) have to be disregarded; although we are able to clean the focal plane data from that emission, we cannot entirely do so in the BNDs. Around 1.3 keV we see some scatter in the data, which is also induced by the uncertainty of the BNDs of the order of 10 to 20%. At all other energies, with a few exceptions, we measured the effective area to an accuracy of 5 to 10%. At high energies above 6 keV counting statistics do not allow a determination better than 10%.

We compare these measured effective areas to the expected area distribution from equation 1. To first order we find a remarkable match of the data to the expected distribution. However, there are notable deviations, which are at the limit or exceed the 5% uncertainties of the data points. At +1st order, the very low energy data points stay below the expectation by an amount of somewhat less than 5%. There may be a similar trend in the -1st order, however here without significance. Also in the -1st order above approximately 2.5 keV and below 4.2 keV, the measured areas stay consistently above the calculated function, again by only a small amount. All of these effects happen on CCDs, where we have used a template QE from a different device. The amount of these effect also matches the expected variation between the QEs for different devices. A strong argument against these effects being intrinsic to the grating itself is the fact that in +1st order the area between 2.5 keV and 4.2 keV matches precisely the expectation: this portion covers device S3, which is the template BI device.

Figure 7.20 shows the areas determined for the MEG 3rd orders. Again, except for a couple of data points, the general trend shows that the measured values match nicely the expectation. However, the statistics already limit the significance to less than 20%. Therefore we will not present higher order data in this context. Those results will be presented in terms of efficiency ratios for combined order by [26] in this volume.

7.7.4.4 1st and 2nd order effective areas for the HEG

The bottom diagram of figure 7.2 shows the the subassembly expectation for the sum of the positive and negative 1st and 2nd HEG orders. The 2nd order efficiency, comparable to the 3rd order efficiency in the MEG, is low enough to ensure that results will be not be affected by pile up. For the first order, we face a similar situation to the MEG first order, i.e. pile up is sufficiently corrected for by adding the 2-photon peak in the pulse heights back to the measured count rate. This peak is detectable thoughout the whole band pass.

Figure 7.21 shows the effective areas determined for the -1st (top, m1) and +1st (bottom, p1) order of the HEG. Note, that the HEG has considerably less efficiency below 2.5 keV than the MEG. Therefore counting statistics are worse than in the MEG. Below 1.5 keV we cannot determine the effective area better than 20%, above 1.5 keV and below 5 keV the uncertainties are of the order of 10-15%. Again the range around 1.75$\pm$0.15 keV is not reliable and should be disregarded.

Within the given uncertainties, the measured values again fit quite well with the expected function. At -1st order, like observed in the MEG the area between approximately 2.5 and 4.2 keV stay consistently above the expectation, which again points towards a slightly higher CCD efficiency at high energies in S2. A major effect is observed above 5 keV in both orders. Here we already observe signs of pileup through grade migration. Above 7 keV the effect that charge is completely lost is also clearly visible in the data. The MEG -1st order does show a similar trend around 5 keV at a much lower scale, because of the lower incident fluence in the larger MEG image size.

Figure 7.20 shows the areas determined for the HEG 2nd orders. The measured values match the expectation. But like observed in the MEG 3rd orders, statistical uncertainties the significance to less than 20%. For higher order results we refer to Section 7.10.

7.7.5 Conclusions

We analysed effective area measurements performed at XRCF with the HETGS, by using the DCM energy scans in the energy range from 950 eV to 8700 eV. The measurements were designed to produce sufficient flux in the 1st and higher orders, therefore the 0th order measurements were dominated by pile-up effects. Table 7.3 summarizes the measured effective areas for a selected set of energies. The analysis resulted in the following:

• The absolute effective area of the combined 0th order in MEG and HEG was measured to an accuracy better than 5% in the range 0.9 and 3.0 keV. The larger uncertainties were introduced by systematic errors from the DCM. At energies above 3 keV the measurements were entirely dominated by pile-up effects and the effective area in this range could only be verfied with an uncertainty above 20%

• The absolute effective areas of the 1st orders were determined with an accuracy between 5 and 10% for the MEG and between 10 and 15% for the HEG over most of the energy range. Above $\sim$5 keV counting statistics degrades significantly.

E	0th	MEG 1	MEG -1	MEG 3	MEG -3	HEG 1	HEG -1	HEG 2	HEG -2
eV	cm^2	cm^2	cm^2	cm^2	cm^2	cm^2	cm^2	cm^2	cm^2
1000	58.9±2.5	18.3±1.1	19.4±1.4	0.0±0.0	0.9±0.3	4.9±0.7	6.5±0.8	–	–
	56.8	21.0	21.0	1.6	2.0	4.6	7.3	1.0	1.0
1200	53.6±3.3	38.8±2.7	41.5±2.8	2.9±0.7	3.9±0.8	11.9±1.5	12.6±1.5	–	–
	56.5	40.4	40.4	4.0	4.0	9.1	12.2	1.9	1.9
1400	56.7±4.6	65.0±4.6	61.1±4.4	6.3±1.4	5.7±1.4	21.3±2.6	21.4±2.6	–	3.3±1.0
	50.1	60.1	60.1	5.9	5.9	16.8	20.4	2.5	2.5
1610	48.4±3.1	75.0±3.8	60.3±3.4	6.2±1.0	6.4±1.1	24.2±2.2	21.9±2.1	3.0±0.8	3.3±0.8
	51.0	75.0	66.5	6.4	7.2	24.1	27.2	2.7	2.7
2140	95.0±3.8	29.6±2.0	21.8±1.7	1.8±0.5	2.0±0.5	16.7±1.5	17.4±1.5	1.1±0.4	1.6±0.5
	94.3	27.5	18.9	1.7	2.5	14.5	14.5	1.0	1.5
2500	74.0±3.0	20.8±1.6	18.8±1.5	1.7±0.4	1.6±0.4	12.2±1.2	12.6±1.2	0.6±0.3	1.0±0.3
	80.0	20.8	16.1	1.4	1.8	10.5	10.5	0.8	1.2
3100	94.9±4.1	25.4±2.2	23.1±2.1	2.4±0.7	2.2±0.6	17.8±1.8	17.9±1.8	1.3±0.5	1.3±0.5
	93.2	24.6	21.2	1.8	1.8	17.3	14.9	1.2	1.4
4000	129.6±4.2	26.2±1.9	27.4±2.0	2.2±0.6	2.3±0.6	19.7±1.7	21.5±1.7	1.5±0.5	1.7±0.5
	134.9	24.5	23.1	2.0	2.0	20.7	19.5	1.4	1.4
5000	131.5±6.11	14.6±2.1	11.4±1.8	1.4±0.6	1.5±0.7	14.7±2.1	16.9±2.2	1.0±0.5	1.1±0.6
	149.5	14.6	14.5	1.3	1.3	17.8	18.7	1.2	1.2
6000	122.7±7.6	4.7±1.5	4.7 ±1.5	0.5±0.5	0.6±0.5	7.7±1.9	9.6±2.2	0.6±0.5	0.8±0.6
	105.7	5.0	5.0	0.4	0.5	11.7	13.8	0.7	0.8
7000	53.7±5.3	0.8±0.7	0.9 ±0.7	0.1±0.2	0.1±0.2	4.8±1.6	5.6±1.7	0.3±0.4	0.5±0.5
	56.7	0.8	0.8	0.1	0.1	6.2	8.0	0.4	0.5
8200	16.0 ±3.8	0.1±0.3	0.0 ±0.2	0.0±0.1	0.0±0.1	1.5±1.2	1.5±1.2	0.1±0.3	0.2±0.4
	21.2	0.0	0.0	0.0	0.0	1.9	2.7	0.1	0.1

Table 7.3: Table of results of measured versus predicted effective areas if the HETGS for selected energies. The stated uncertainties include only counting statistics and BND uncertainties. The second row for each energy lists the expected effective area from the HRMA XRCF model and the ACIS and HETG subassembly predictions. Note, that because the predictions are derived from subassembly data, they itself have an uncertainty of up to 5%.

• The measured areas in the 1st orders for the MEG and HEG match the expectation from the XRCF HRMA measurements combined with the subassembly results for the ACIS-S and the HETG to quite a high degree. In detail: the MEG -1st order data from device S2 revealed significant variations that could be traced to variations in quantum efficency of device S2 in ACIS-S with respect to the applied QE template; the HEG measurements above 5 keV seem to be affected by local beam non-uniformities. A careful evaluation is still in progress.

• Although dominated by large statistical uncertainties the measured effective areas for the MEG 3rd and the HEG 2nd orders are very well in agreement with the expectation.

For the future this analysis has to be complemented by XRCF measurements using the EIPS single line sources, which allow us to study the energy range below 0.9 keV as well as the 0th order at high energies under less piled-up conditions. The DCM results for the HEG 1st order have to be fine tuned at high energies by including the measured beam unifomity maps. The 1st order results for both grating types should be refined by applying the actual QE functions for each CCD in the detector array as soon as they become available. Finally the grating results should be cross-calibrated with ACIS stand-alone measurements performed at XRCF. From the results of this analysis and once the outstanding issues are resolved, we will be able to refine our grating models in order to accurately predict the in-flight HETGS absolute effective area.

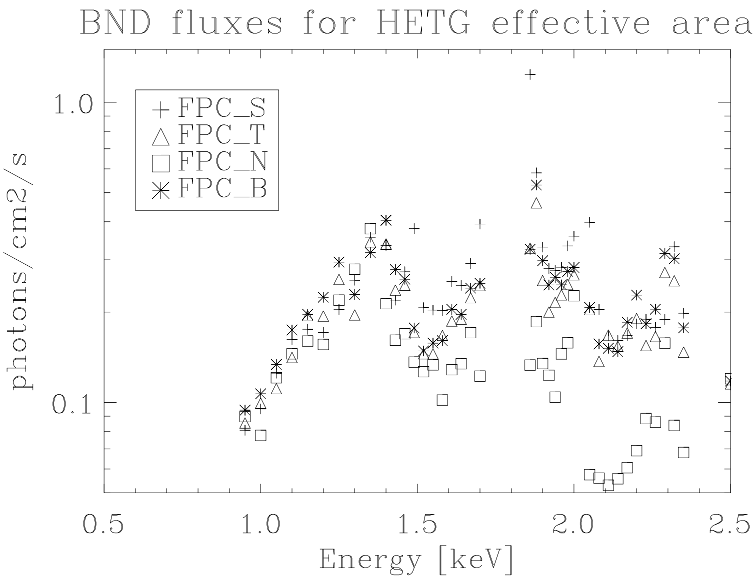

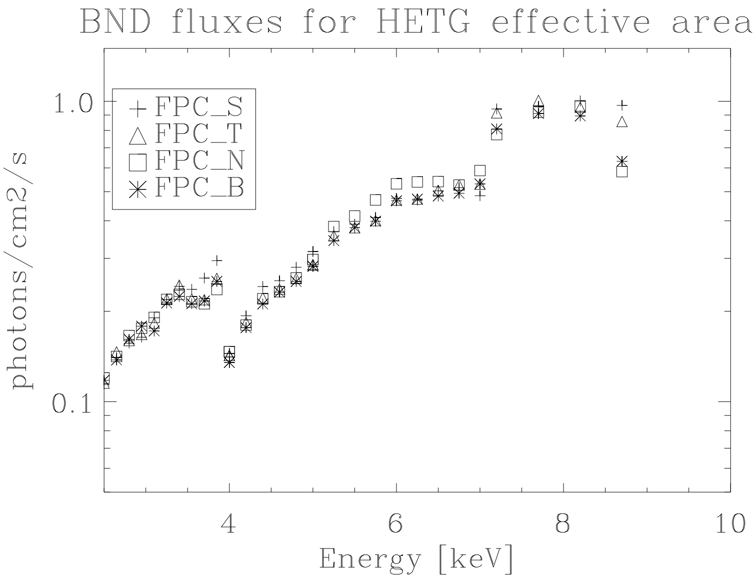

Figure 7.16: BND flux around the HRMA aperture as a function of energy, below and above 2.5 keV .

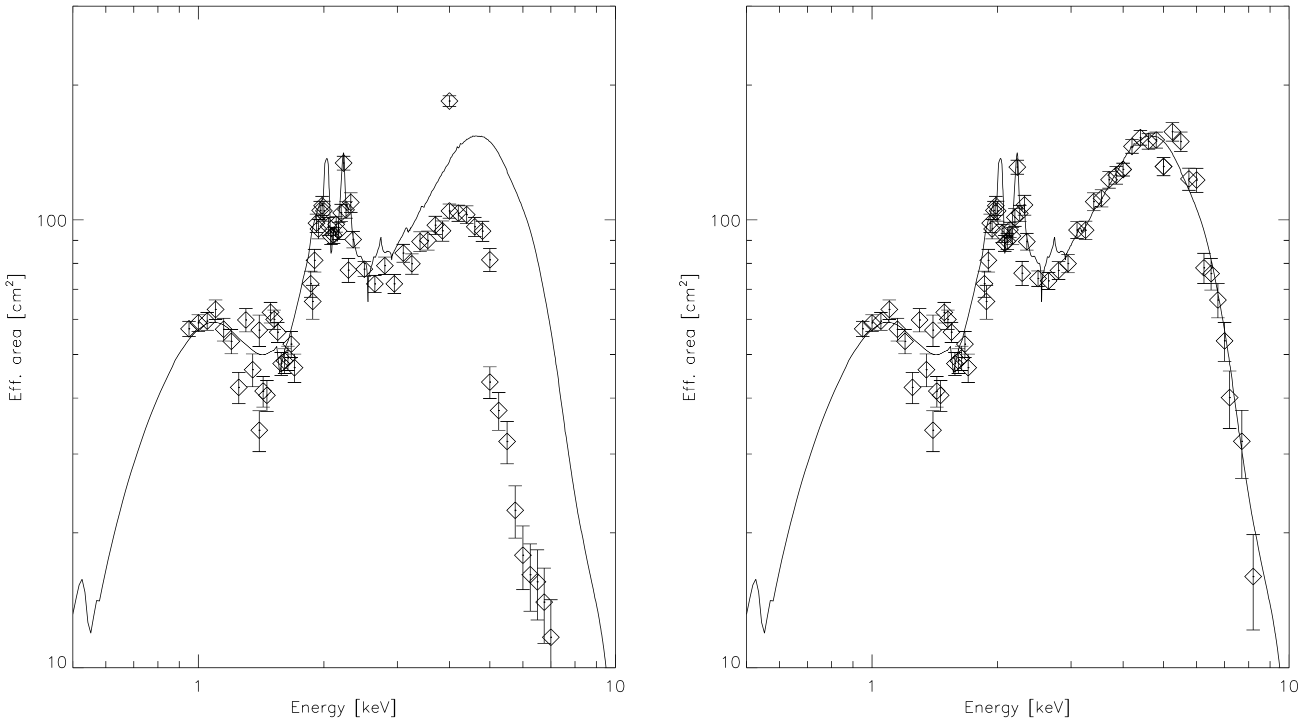

Figure 7.17: Comparison of the measured and expected effective area for the combined 0th order of MEG and HEG as a function of energy. The left hand diagram shows the result without, the right hand diagram with pile up correction as described in the text.

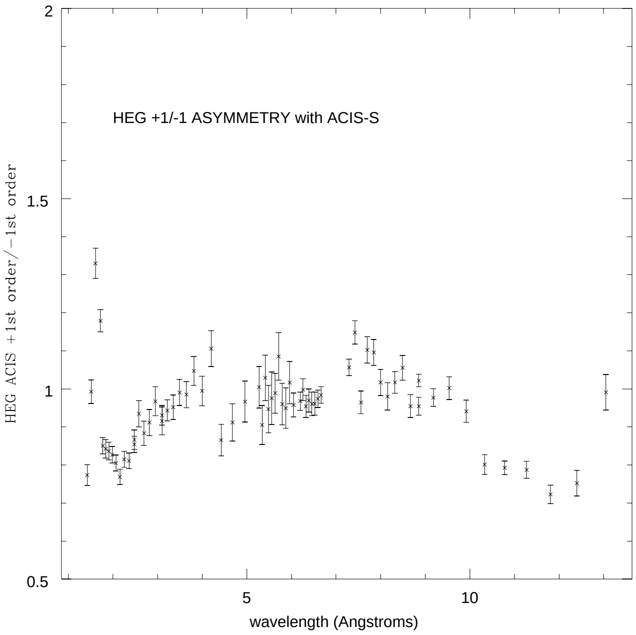

Figure 7.18: Ratio of +1 to -1 for HEG grating on ACIS-S. Structure is due to detector effects.

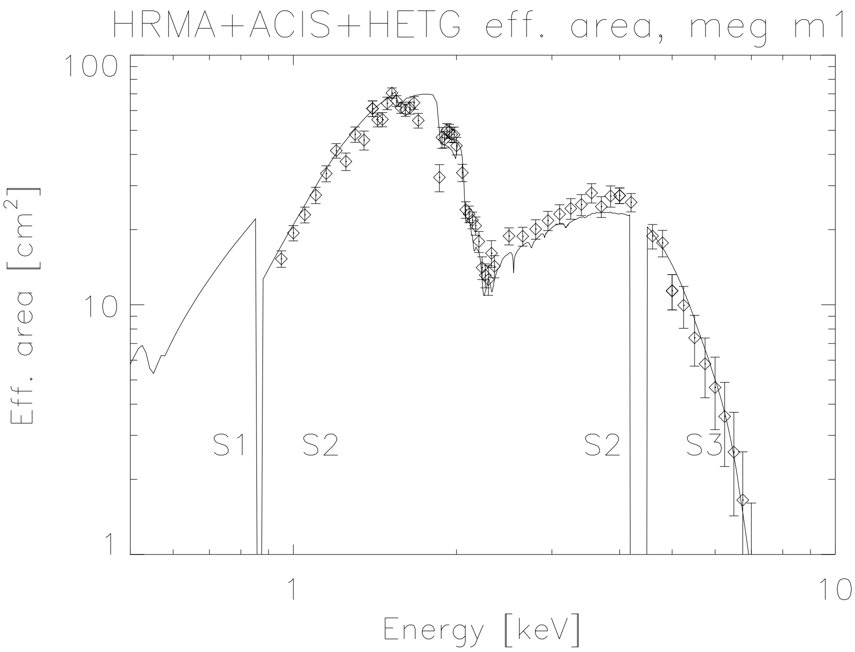

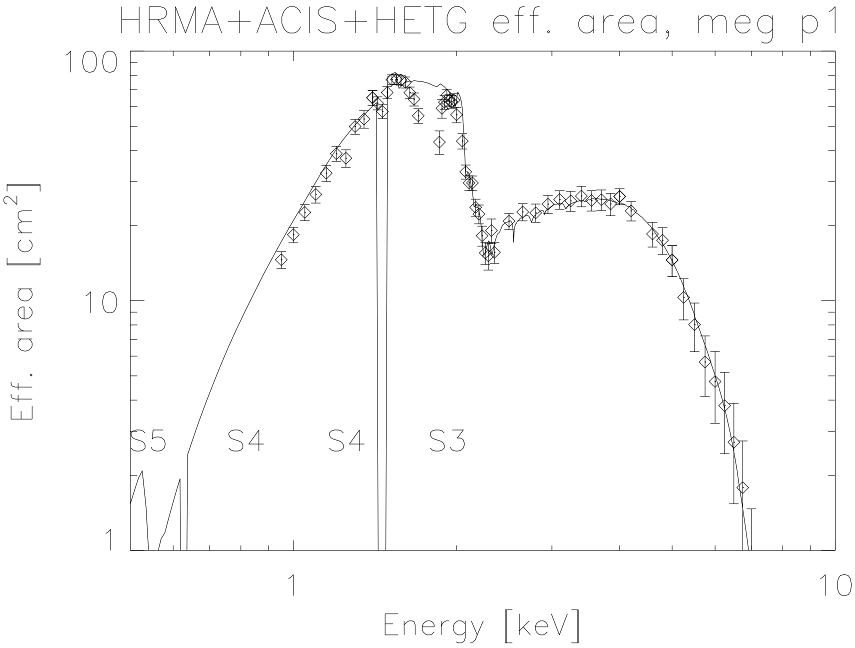

Figure 7.19: Comparison of measured absolute effective areas at XRCF of the MEG 1st order to the expected effective area. Negative orders cover S2 and S3 (from low to high energies), the gap appears just above 4 keV. Positive orders cover S4 and S3 with the gap at 1.5 keV.

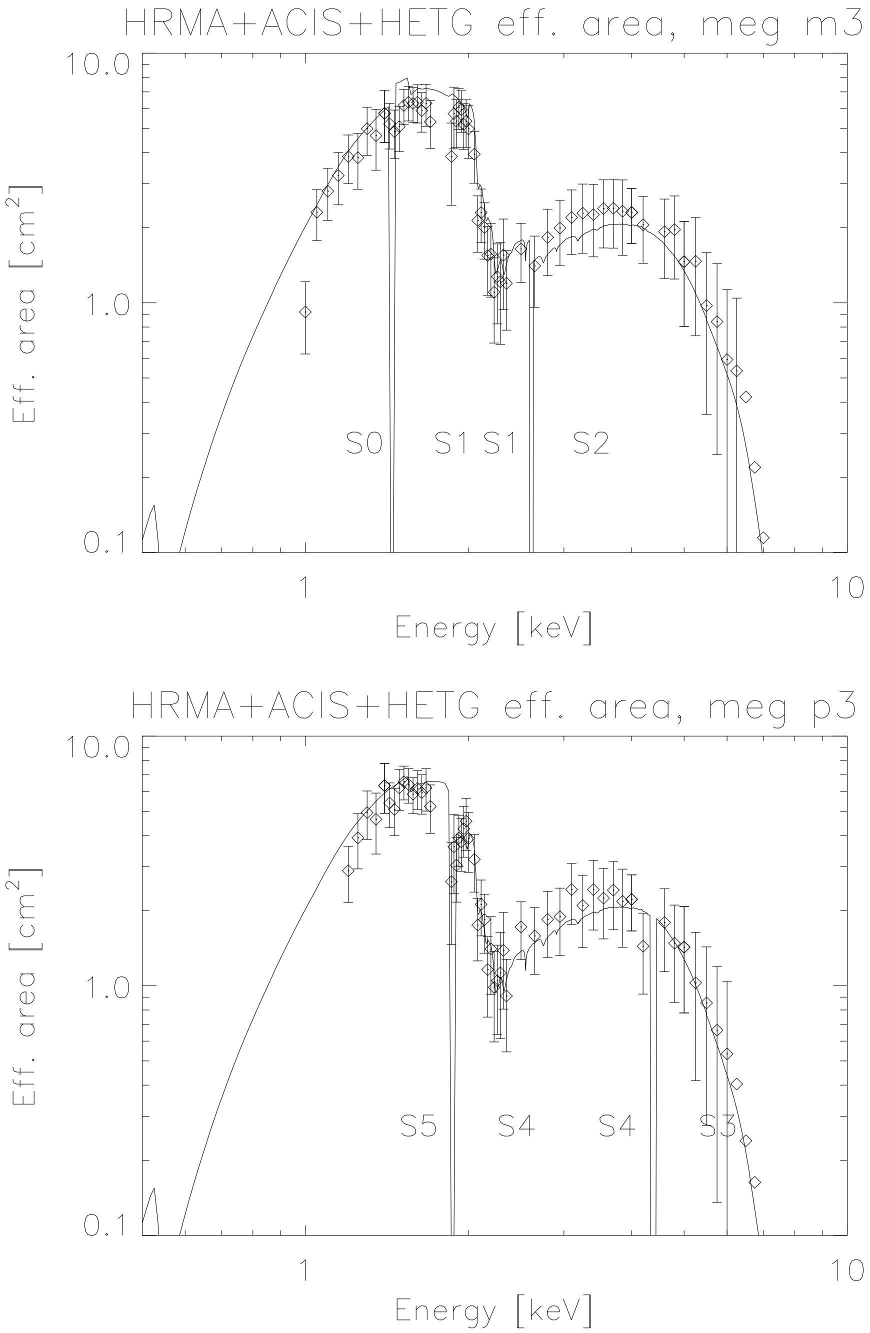

Figure 7.20: Measured absolute effective areas at XRCF of the MEG 3rd order.

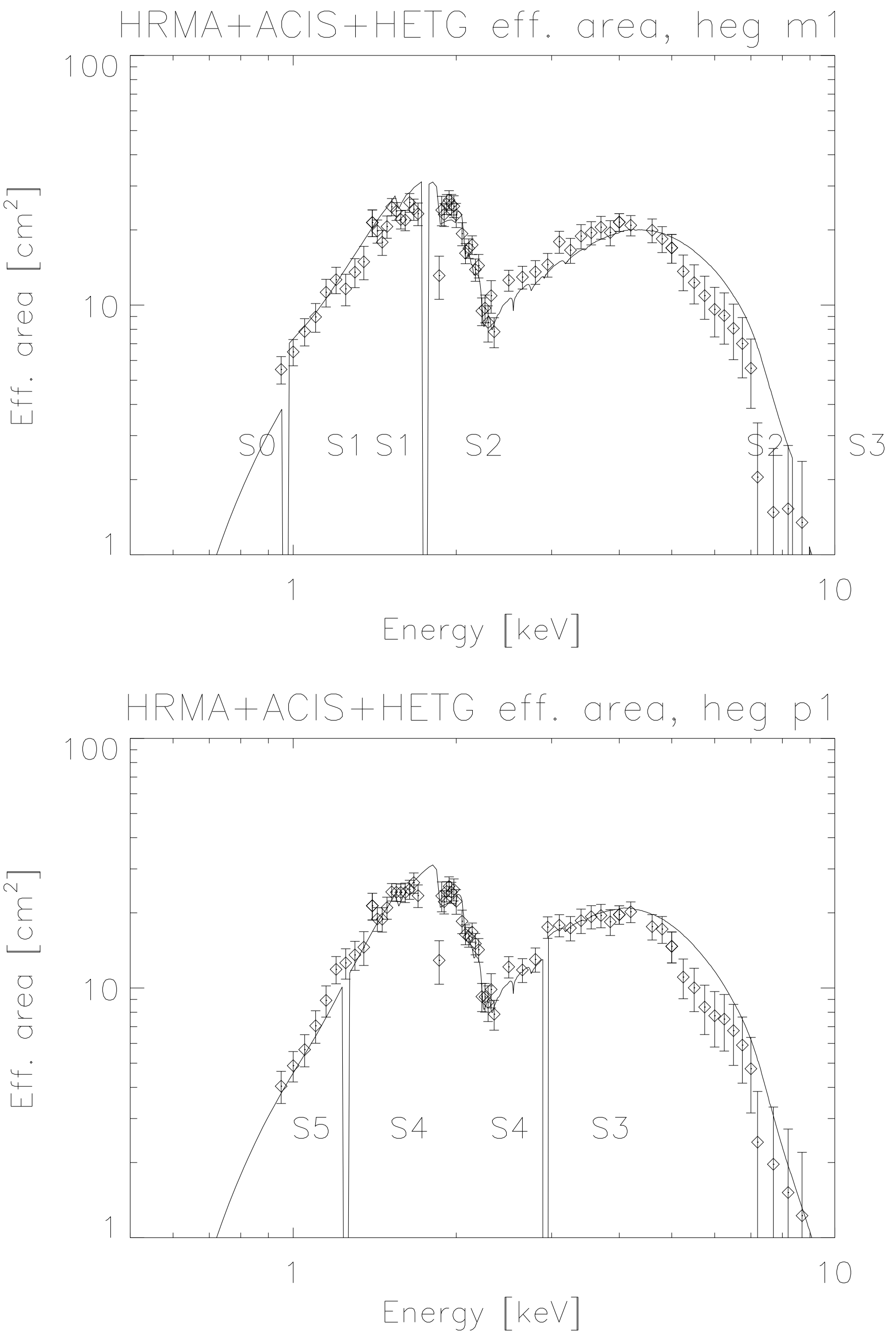

Figure 7.21: Comparison of measured absolute effective areas at XRCF of the HEG 1st order to the expected area distribution. Negative orders cover S1 and S2 (from low to high energies), the gap between the two appears 1.7 keV. Positive orders cover S5, S4, and S3 with the gaps at 1.3 and 2.9 keV respectively.

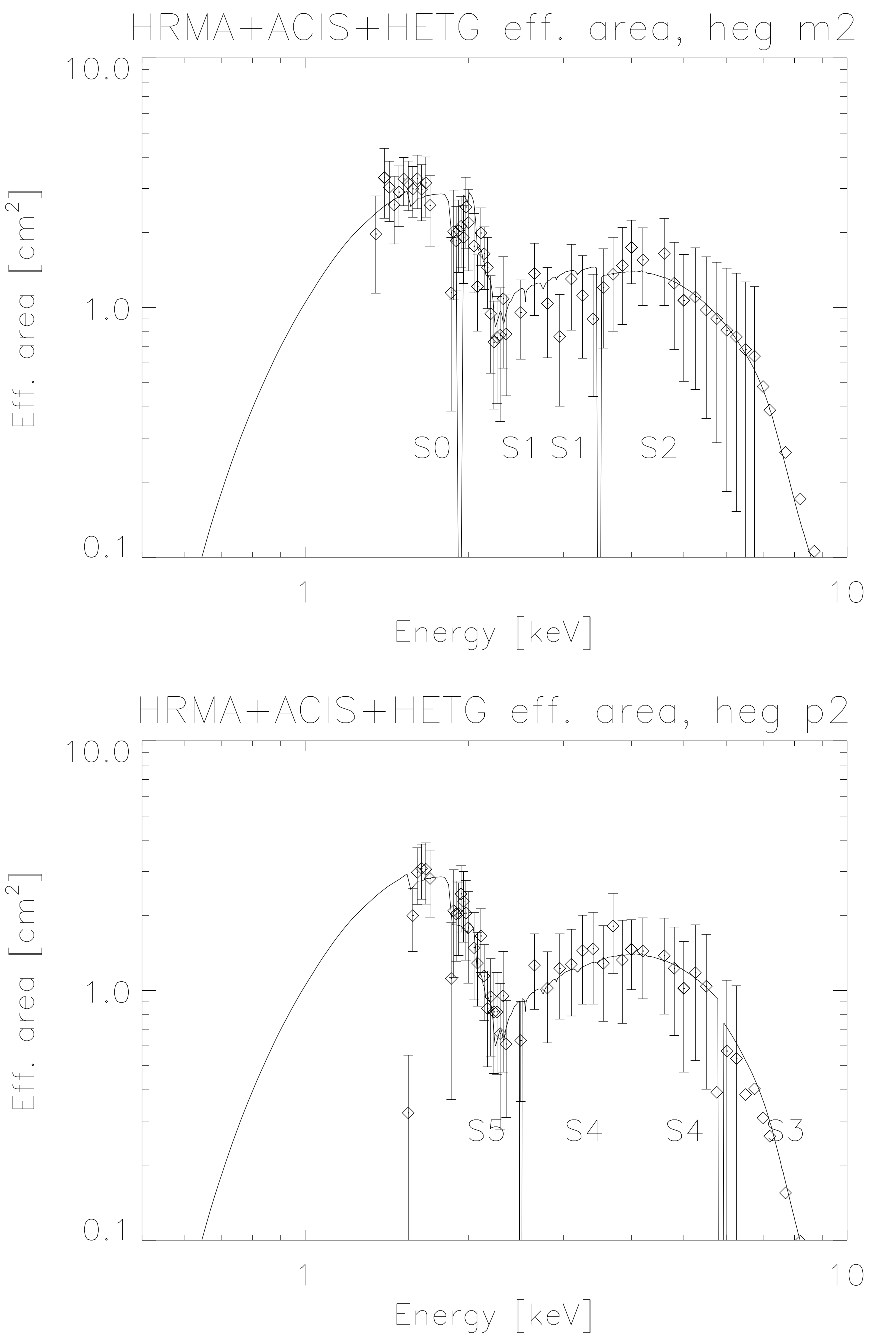

Figure 7.22: Measured absolute effective areas at XRCF of the HEG 2nd order.

7.8 Relative Effective Area: Molecular Contamination

Objective: Verify our detailed grating and detector spectral models and search for unexpected spectral features by observing a continuum source with the HETGS.
Publication(s): Marshall *et al.* [49]

In order to probe for small scale spectral features of the HETGS effective area, we performed tests at XRCF using the Electron Impact Point Source (EIPS) with the Cu and C anodes and operated at high voltage and low current in order to provide a bright continuum at high energies. In fact the continuum was bright enough to obtain 100-1000 counts *per spectrometer resolution element* over most of the useful energy range of the HETGS. The ACIS-S was used to discriminate orders and to provide high throughput with negligable pileup it was operated in continuous clocking (CC) mode.

Many spectral features are observed but most of them are emission lines attributable to the source spectrum. We find that the current models for the HETG efficiency and HRMA effective area predict very well the observed fine structure near the Au and Ir M edges where the models are most complex. Edges in the detector filter and quantum efficiency (QE) curves are somewhat more sharply defined in the data than in the current models.

By comparing the positive and negative dispersion regions, we find no significant efficiency asymmetry attributable to the gratings and we can further infer that the QEs of the ACIS-S frontside illuminated (FI) chips are consistent to $\pm 10\%$. On the other hand, we derive the ratio of the QE for the backside illuminated (BI) chips relative to that of the FI chips and show that it deviates from the expected ratio. This deviation may result from grade differences due to operation in CC mode while most calibration data are obtained in timed event mode.

To do: include Carbon results, can mc test confirm chip gap values?

7.8.1 Observations and Data Reduction

7.8.1.1 General

The tests that were reduced are given in table 7.4, taken at the XRCF on 1997 April 25 between 0341 and 0806 UT. For each of these tests, the EIPS was fitted with the Cu anode set to maximum voltage, 20 kV, and minimum current, 0.1 mA, in order to achieve the highest continuum but

Test ID	Grating	HRMA Shells open	Open Quadrant pattern
H-HAS-MC-3.001	HETG	1,3 (HEG subset)	NS, TB
H-HAS-MC-3.005	HETG	4,6 (MEG subset)	T, N, B, S
H-LAS-MC-3.009	LETG	all	T, N, B, S

Table 7.4: This table shows the set of tests used in the data analysis. For an overview of AXAF calibration, see Weisskopf *et al.*[79]. The HETG high energy gratings (HEGs) have periods near 2000 Å and are arrayed to receive light from the inner pair of HRMA mirrors while the HETG medium energy gratings (MEGs) have periods near 4000 Å and correspond to the outer mirror pair. The quadrant pattern represents the order in which the north (N), south (S), top (T) and bottom (B) quadrants were opened in order to reduce the telemetry saturation.

keep the total count rate down without using filters. In order to prevent possible radiation induced damage due to the bright zeroth order image, the detector assembly was "dithered" using the five axis manipulator (FAM). A serpentine pattern was used. Long motions in the cross dispersion direction allowed us to reduce the data in large sections at fixed offset along the dispersion direction. Dithering had the advantage of smoothing over detector gaps and any other features.

The ACIS-S was run in the continuous clocking mode and "faint" mode so that three pulse height values were obtained for each event. The detector telemetry limit in this mode is about 393 events/s (see the AXAF Proposer's Guide[59]). As it was, the source was so bright that the ACIS-S telemetry limit was reached easily. Shell quadrants were closed to reduce the count rate to a manageable level during the tests and approximately equal exposure was obtained for all shells.

As described in the AXAF Proposer's Guide[59], when the telemetry limit is reached, CCD buffers fill and data may be lost. To allow the buffers to empty in each shell quadrant configuration, the mirrors were exposed for 15 min and then closed for 5 min. Exposure is then determined by counting frames, since frames are never only partially lost. The good frames are determined by examining the average counts per frame within the time intervals during which the shutters were open. These time intervals were then examined manually to ensure that closed shutter periods were excluded in the results and to make sure that all good frames were included. The exposure per frame is given by the time to read out 512 rows at 10 μs per column per row and 285 rows per column, giving 1.459 s. The exposure was determined for each CCD separately because the buffers are independent. The pixel boundaries of each chip were transformed into wavelengths by the same method used for the events (see section 7.8.1.2) and then both sides were added to obtain the exposure functions shown in figure 7.23.

All events from columns containing hot pixels were eliminated from the data and from the exposure function. The hot pixels were most apparent in detector coordinates because the detector was dithered during the observations. Known hot pixels[59] were apparent in the first two observations (3.001 and 3.005) but two new ones showed up in the LETGS observation (3.009) in columns 225 and 232 of the S3 ACIS-S CCD. Another, much milder hot pixel showed up at column 670. The previous hot pixels (columns 383 and 792) were not observed. The new hot columns (or pixels) are somewhat surprising because the test 3.009 immediately followed test 3.005 and the ACIS electonics were not changed.

7.8.1.2 Event Processing

The overall event processing approach was the same for each test. First, the details of the dithering were measured and events were shifted to compensate. Both the actual FAM shift in XRCF Y coordinates and the times of the shifts were measured from the centroids of bright emission lines in detector coordinates. The Cu-Kα_1 (8.02783 keV) at $m = +1$ was used for test 3.001, while the $m = +2$ line was used for test 3.005 and the $m = +3$ line of cu-Lα (at 0.9297 keV, or 13.336 Å) was used for test 3.009. These data, shown in figure 7.24, indicated that the actual FAM Y shifts for all three tests were 0.18 mm, compared to the commanded values of 0.20 mm.[1] The actual time between Y shifts was observed to be about 561.5 frames, or 819.2 s, which is consistent with the expected value of 820 s.

[1] Irregularities in the FAM positioning were found in analysis of the HETGS scattering test[48, 16]. The sense of the deviation from the commanded motion was 10× smaller and had the opposite sign to the deviation determined here, however.

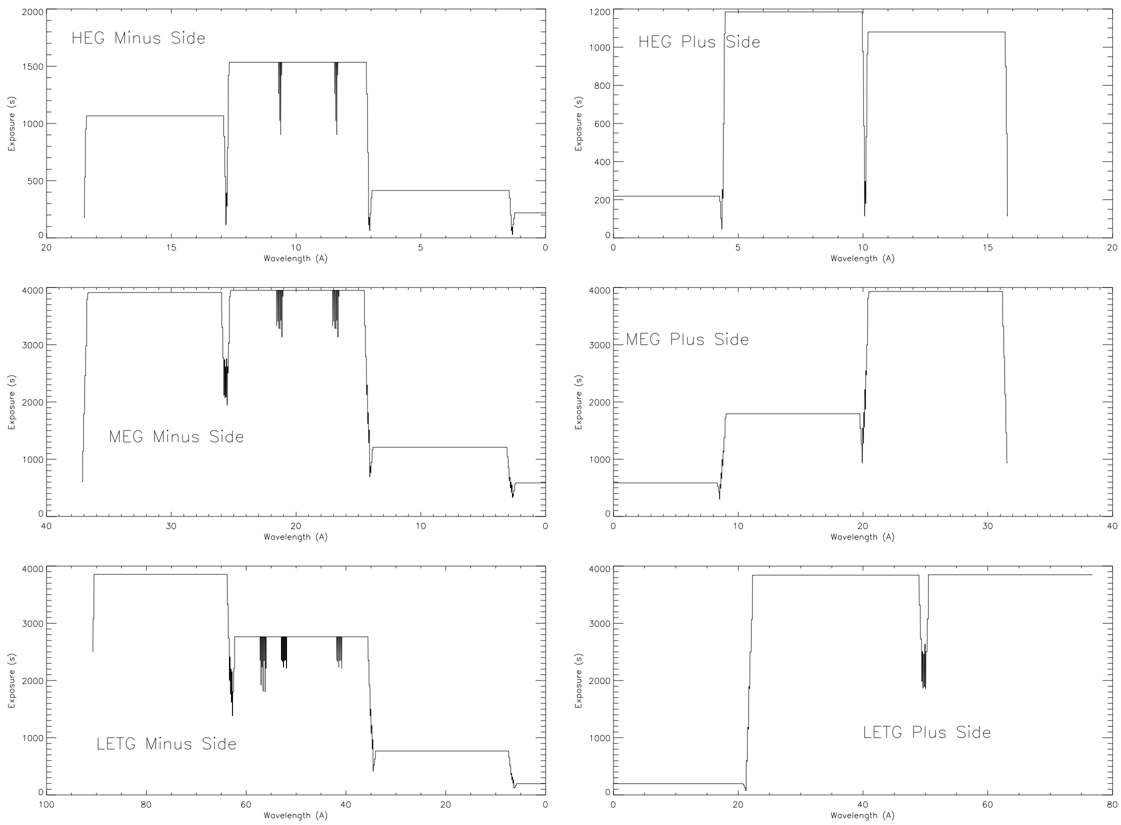

Figure 7.23: Exposure as a function of wavelength for each test and for the positive and negative orders separated. The details of the tests are given in table 7.4. Wavelengths are determined from the dispersion relation for an assumed first order spectrum. The ACIS-S CCDs start with S0 on the left and end with S5 on the right. CCD gaps are apparent; the exposure doesn't go to zero due to shifting of the detector assembly along the dispersion direction during the tests. The zeroth order (and origin) was always on the S3 CCD, a backside illuminated (BI) CCD. Several series of shallow dips result from the elimination of columns on the S1 (BI) CCD containing hot pixels and again were shifted to different locations in wavelength space as the detector was moved.

Second, event dispersion distances from zeroth order were computed based on a trial position for the zeroth order (normally determined by the absolute positioning of the FAM). By comparing the positions of lines in the positive and negative sides, the zeroth order position was measured to within a detector pixel (24 μ).

Third, a wavelength, λ_1, for each event was computing under the assumption of first order using the observed dispersion distance for that event and the grating periods, angles and Rowland distances derived from previous XRCF measurements[19]. For the HETGS, the dispersion distances are not directly observed, only the projection along the XRCF Y axis so the projected distance was corrected by $\cos\alpha$, where α is the angle from the dispersion direction to the XRCF Y axis.

Fourth, events are selected by order using the energy, E, computed from the event pulse height. Events were assigned to order m if $|E - hc/(m\lambda_1)| < \delta E$, where h and c are the Planck constant and the speed of light, respectively, and δE is 250 eV (or 150 eV in the case of the LETG observation), larger than the detector energy resolution.

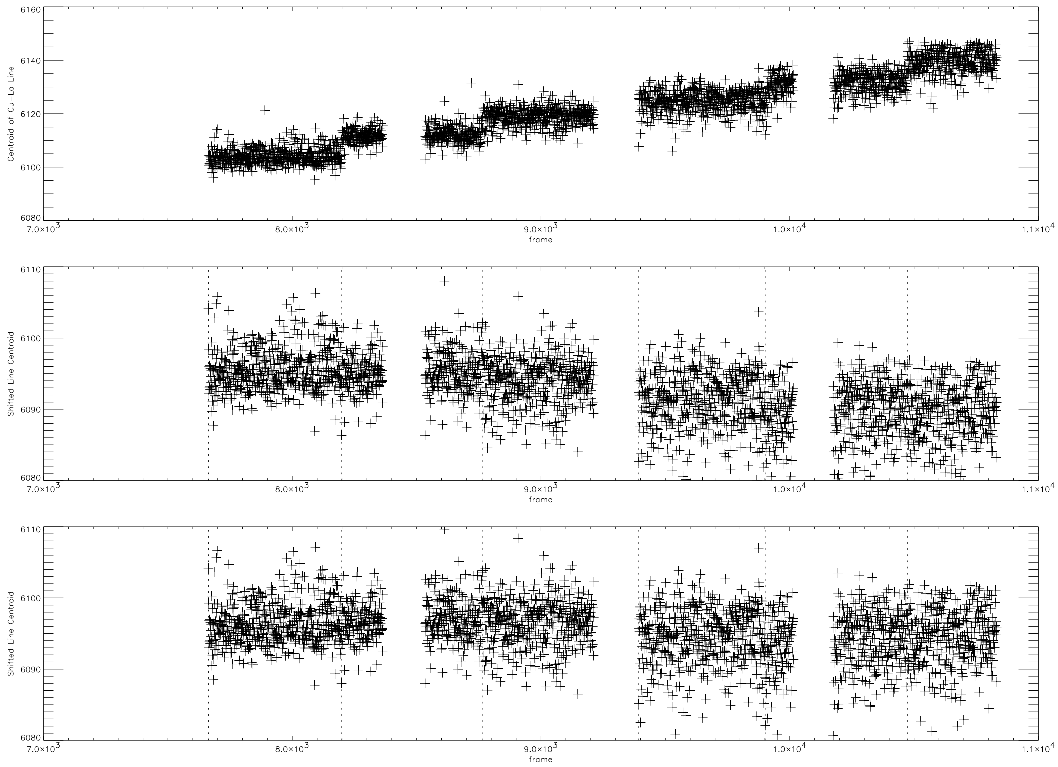

Figure 7.24: Centroid of the Cu-Lα line (at 13.336 Å) in detector coordinates as a function of ACIS frame (in continuous clocking mode) for test H-HAS-MC-3.005. *Top:* Raw centroids showing the systematic shifts due to dither, where the detector is moved in the $+Y$ direction every 820 s, or 562 frames. *Middle:* Centroids are corrected for shifts of 0.20 mm, which was the commanded value. Dashed lines indicate times when the shifts took place. A residual trend remains, indicating an error in the dither magnitude. *Bottom:* Centroids are shifted by 0.18 mm at each shift time to eliminate the secular drift.

Finally, events were selected according to CCD grade. The CCD grades were determined from the event pulse heights as in timed exposure mode except that only the 3 pulse heights from the event row were available instead of a 3×3 event "island". Thus, certain ACIS grades were not observed, such as those like ASCA grade 2 and 6, which are normally included in the event selection. Similarly, although grades 1 and 5 are normally eliminated in processing, since these grades require detecting corners of the event islands, there were no such grades available. Thus grading had little effect on the event selection.

7.8.2 Formation and Interpretation of the Continuum Spectra

A model of the effective area was generated from a HRMA effective area model recent HETG and LETG efficiency functions, the ACIS-S flight filter model and the ACIS-S FI QE model. All data files used here are available from the AXAF Science Center (ASC) calibration group web page (`http://asc.harvard.edu/cal/cal.html`) and were derived from instrument and telescope team characterizations of the AXAF components.

Because of the high spectral resolution of the grating spectrometers, it is important to use finely gridded models, especially near the spectral features such as the Au M and Ir M edges. The

HRMA effective area (EA) was generated by the AXAF telescope science team and is posted to their web site (`http://hea-www.harvard.edu/MST/mirror/ www/xrcf/hrma_ea.html`). They adjusted the model of the EA so that the prediction would conform to various XRCF measurements such the SSD continuum data[43] and they incorporated details of Ir reflectivity based on updated optical constants[32, 33]. For our purposes, the gradual variation of EA with aperture size will not have a significant effect because we are searching for spectrally small effects, so we used the EA integrated over 2π. The HETGS efficiencies incorporate details of the Au edges as described in Section 3. The ACIS flight filter transmission model was fitted to synchrotron data[1] and should include fine structure around the Al and O edges. The ACIS-S CCD QEs are taken from detailed QE curves for two "template" CCDs: one FI chip in the ACIS-I array and one BI chip (S3) in the ACIS-S array[1]; the data from the ASC web page were supplemented with QE values in the 0.05-0.20 keV range with data from a fit to BI QEs by the ACIS/MIT team (see the `QDP` plot of the w134c4r QE on `http://acis.mit.edu`).

Events were binned into histograms before forming a spectrum. The source flux, $f(E)$ (in photon cm^{-2} s^{-1} keV^{-1}), is estimated by combining the data from the positive and negative orders. Denoting the positive side with $+$ and the negative side with $-$, the expected number of counts in a pixel at energy E is given by

$$\begin{aligned} C_+ &= fA\epsilon_+TQ_+t_+dE \\ C_- &= fA\epsilon_-TQ_-t_-dE \end{aligned} \tag{7.12}$$

where C_- and C_+ are the counts in a pixel at energy E, Q_+ and Q_- are the QEs of the ACIS-S detectors, ϵ_+ and ϵ_- are the efficiencies of the grating into positive and negative orders and are assumed to be equal to ϵ, A is the effective area of the HRMA, T is the transmission of the ACIS-S optical blocking filter, and t_+ and t_- are the exposure times. The quantity dE is the energy width of the pixel based on the derivative of grating dispersion relation (for orders $|m|$ = 1) which is very nearly linear:

$$dE = hcE^{-2}P\frac{\delta x}{D}cos(\alpha) \tag{7.13}$$

where P is the grating period, D is the Rowland distance, and δx is the physical size of an ACIS-S pixel, 0.024 mm. The count spectra for the two sides were combined using an estimator that is not sensitive to situations where the counts on one side were small or zero (due to gaps between CCDs):

$$\hat{f} = \frac{C_+ + C_-}{A\epsilon TdE(Q_+t_+ + Q_-t_-)} \tag{7.14}$$

The spectra derived from each test are shown in figures 7.25, 7.26, and 7.27. The Cu-L line series (consisting of α, β, η, ζ, and $\beta_{1,2}$) is quite prominant in all spectra and makes it difficult to search for weak features in the 0.8-1.05 keV region. The Cu-Kα and Kβ lines are apparent at the high energy end so the nearly featureless continuum from 1.05 keV to 7.9 keV could be used for the purposes of this project. The O-Kα and C-Kα lines are also apparent in the MEG and LETG tests and are somewhat broad.

There are features that can be attributed to high orders from the strongest lines, in spite of the pulse height selection. It appears that these high orders can be detected because of a low pulse height tail that extends from the energy of the line down to the background level. These high order lines are especially noticeable in the LETGS spectrum (see figure 7.27). For example, the Cu-Lα line has an energy of 0.9297 keV but there are a significant number of events with ACIS pulse height energies in the .15 to .45 keV range. When the emission line is dispersed to

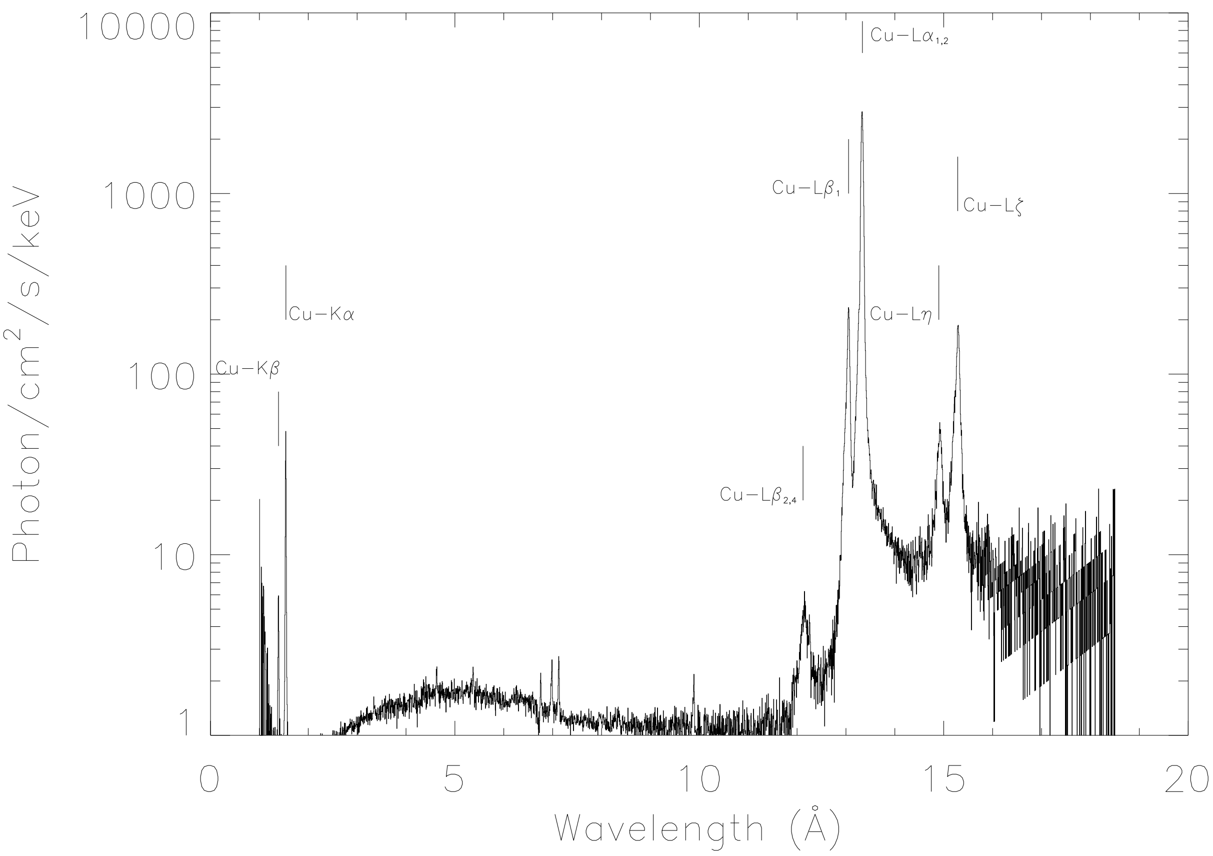

Figure 7.25: Spectrum of the source measured by the HEG portion of the HETGS (test H-HAS-MC-3.001). The strong emission lines were easily identified and are marked. The Cu-L lines are broad and have wings that make modelling difficult near them. Weak features are identified in figure 7.28. The continuum in the range between the Cu-K and Cu-L lines is well fitted with a 10th order polynomial with a few emission lines.

$m = 4$, the events are dispersed to a distance corresponding to 0.31 keV, where the pulse height selection accepts events in the 0.15-0.45 keV range. The pulse height distribution is discussed again in section 7.8.3.

Comparing the spectra obtained from each grating, we see that the continuum and line strengths are very similar but there are systematic deviations. These differences are not the subject of this analysis but may be ascribed to differences between CCD QEs, because each grating places a specific energy onto a different combination of ACIS-S CCDs. In section 7.8.3, we show that there are systematic deviations from the expected QE curves using data from within a single grating observation. This issue requires further investigation.

It is clear from the spectra that pileup is not a significant concern when analyzing these data. The peak count rates in the Cu-Lα and Cu-Kα lines gave count rates of order 10 count/s in the HEG observation. For an effective frame time of 0.00285 s in continuous clocking mode, we obtain only 0.03 count/frame, for less than 3% pileup. For the continuum regions, pileup is a

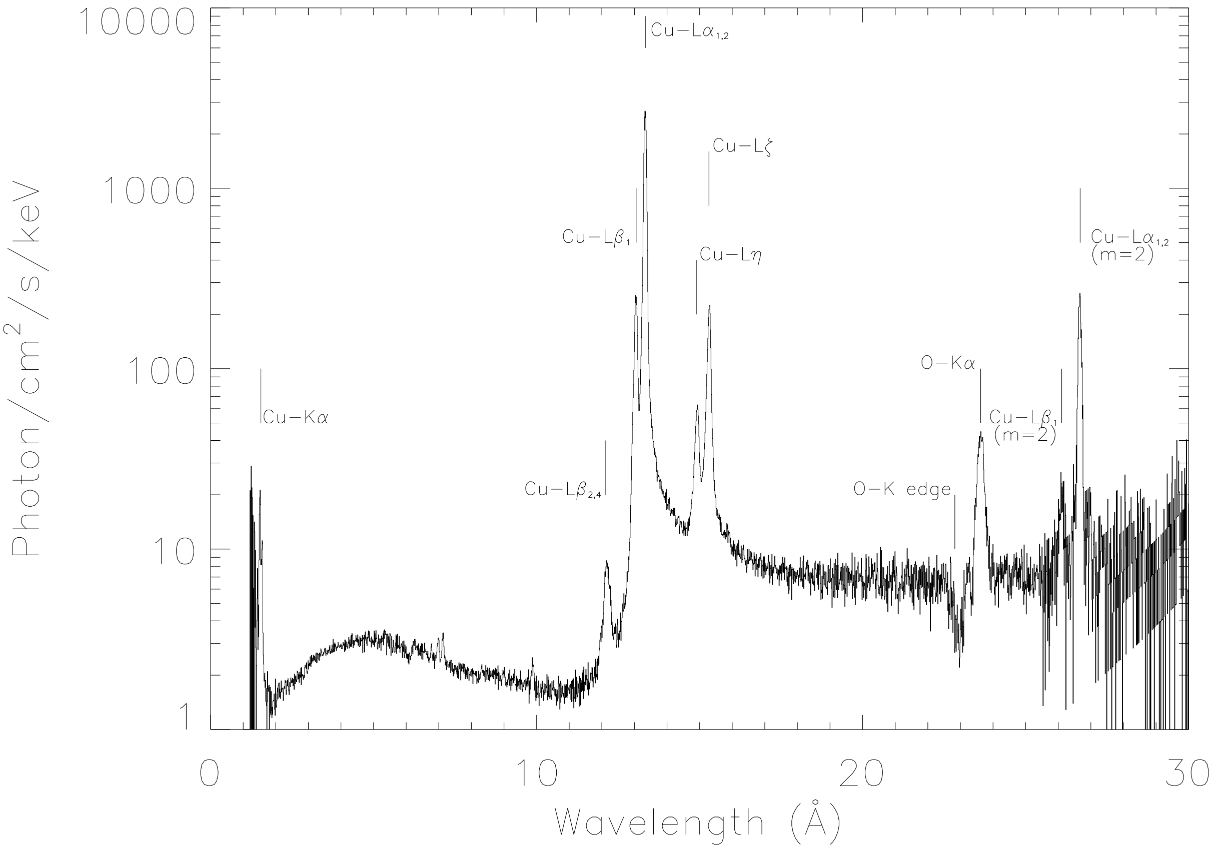

Figure 7.26: Spectrum of the source measured by the MEG portion of the HETGS (test H-HAS-MC-3.005). The Cu-L α (0.9297 keV), β_1 (0.9498 keV), η (0.832 keV), and ζ (0.8111 keV) are the strongest lines and O-Kα (0.5249 keV) is also easily detected. The line observed at 0.465 keV is actually Cu-Lα observed in second order that is picked up in this first order spectrum due to low pulse height events in the ACIS pulse height distribution. An O-K edge feature is apparent in the 0.53-0.55 keV range.

factor of >10 less. In the LETGS observation, the Cu-Lα line gives somewhat more counts per frame due to the lower resolution; there is as much as 30 count/s, for at most 10% pileup in this line. Again, the pileup fraction would be less than 1% for most spectral ranges of interest.

We have not yet computed a complete model for the source because the goal of the test was to use the continuum to search for edges and absorption lines which are not part of the source. The continuum shape is not well known *a priori* but is not required for our immediate purpose. The spectrum was estimated empirically from the HEG observations shown in figure 7.25 by fitting a 10th order polynomial so that we could examine the details of the edge and emission structure in more detail. The data are compared to the model in figure 7.28. Several emission lines due to contaminants in the source are apparent as deviations from the model. Other deviations are observed at the Al-K and Si-K absorption edges which are in the ACIS-S filter transmission model and the ACIS-S QE model, respectively. The data indicate that the edges are somewhat sharper than predicted. These deviations are caused merely by interpolating the coarsely gridded model files. When more finely computed models are made available, these edges

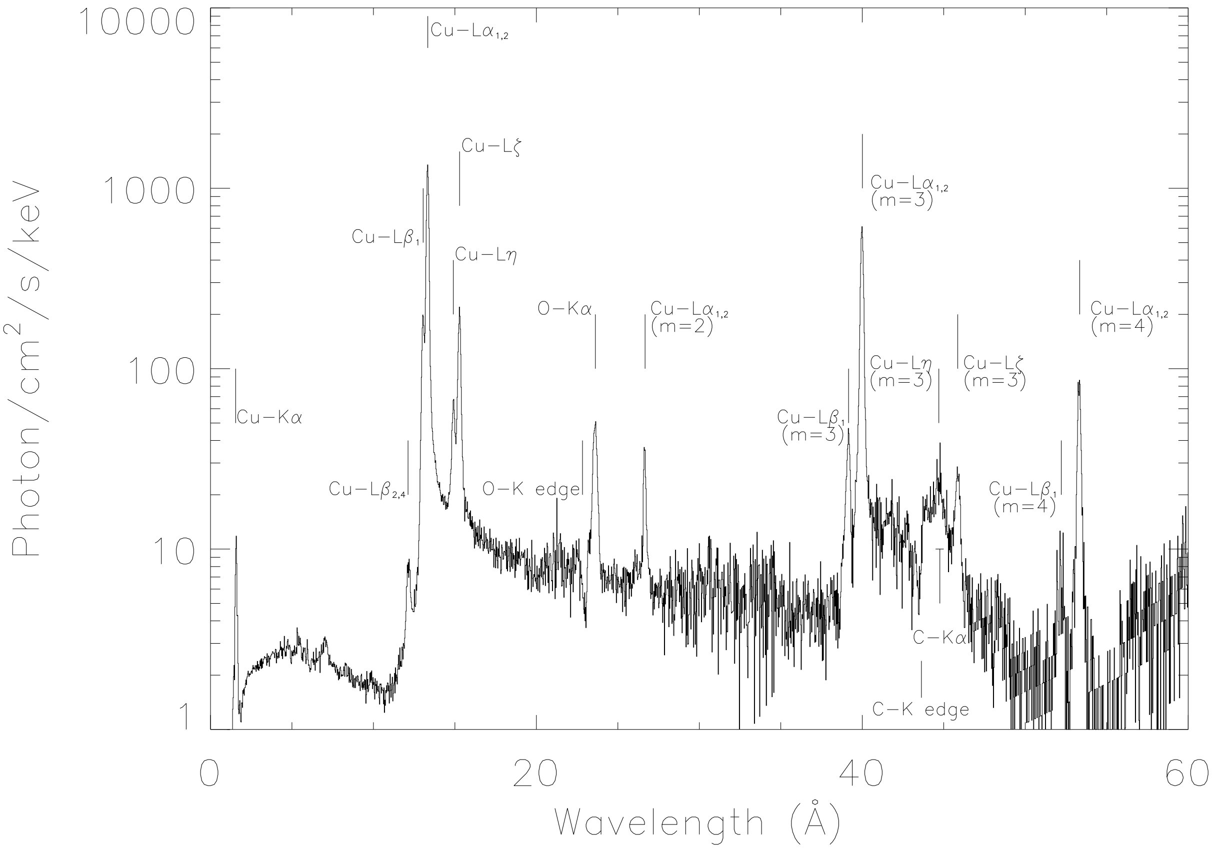

Figure 7.27: Spectrum of the source measured by the LETGS (test H-LAS-MC-3.009). The Cu-L series is observed in many orders due to the tail of the ACIS pulse height distribution. Note that the $m = 2$ lines are considerably weaker than the $m = 3$ high order lines, as expected for the LETGS. The O-K line is apparent, as in the MEG spectrum, and C-Kα is detected as a broad line component under the $m = 3$ version of Cu-Lη. Note the residual Cu-K edge at 0.28 keV.

should be more sharply defined and will be better modeled.

Another feature that is apparent in figure 7.28 is a deviation at 2 keV. This feature is in the model but not in the data and is caused by a sharp "edge" in the HRMA effective area model. This edge is not physical and was the result of patching newly determined optical constants to older Henke values at this point (R. Edgar, private communication). The feature should be eliminated in the next update to the HRMA effective area.

7.8.3 Comparison of Positive and Negative Sides

The ratios of the counts, $R = C_+/C_-$, in the two sides is dependent only on the QEs and the exposure times as long as the grating efficiency is the same for positive and negative orders. All subassembly and XRCF data to date have shown no differences between positive and negative

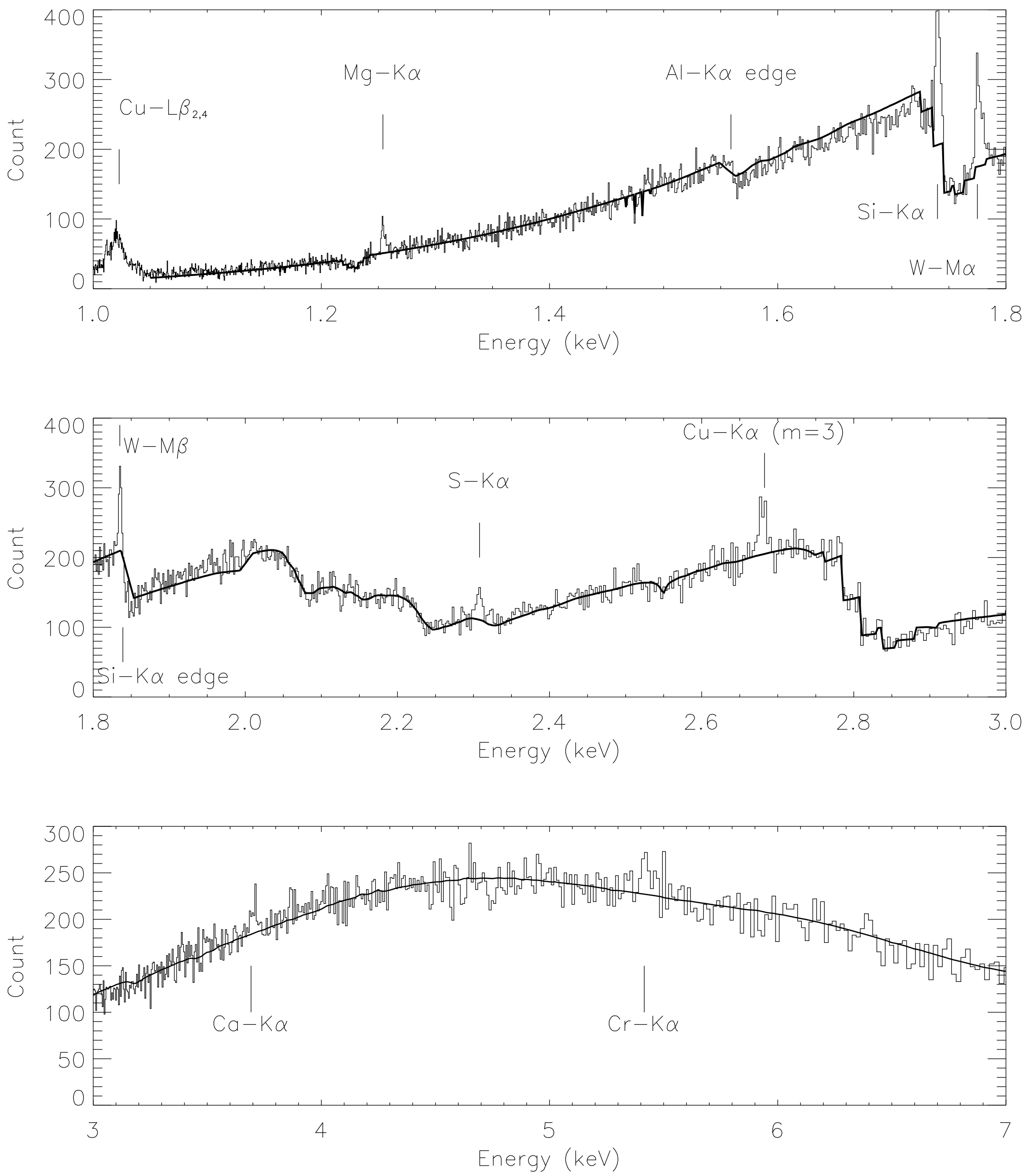

Figure 7.28: Detailed view of HEG-Cu spectrum and model features. The measured count spectrum for three separate energy ranges of the test with the HEG portion of the HETGS (test H-HAS-MC-3.001) are shown here. Emission line features that are intrinsic to the source are marked (e.g. Mg-Kα at 1.254 keV). Two absorption edges are marked (Al-K at 1.559 keV and Si-K at 1.839 keV) where the model of the ACIS-S filter (Al-K) and the detector (Si-K) are so coarsely gridded that the edge does not appear as sharply defined as the data indicate. The bumps and dips from 2.05 through 2.2 keV are the result of Ir M edges in the HRMA effective area and those in the 2.2 to 2.6 keV range arise primarily in the Au M edges of the HEG efficiency curve. Other sharp features are due to exposure variations. A significant deviation from the model occurs at 2.0 keV where the HRMA effective area has a feature that is not tracked by the data.

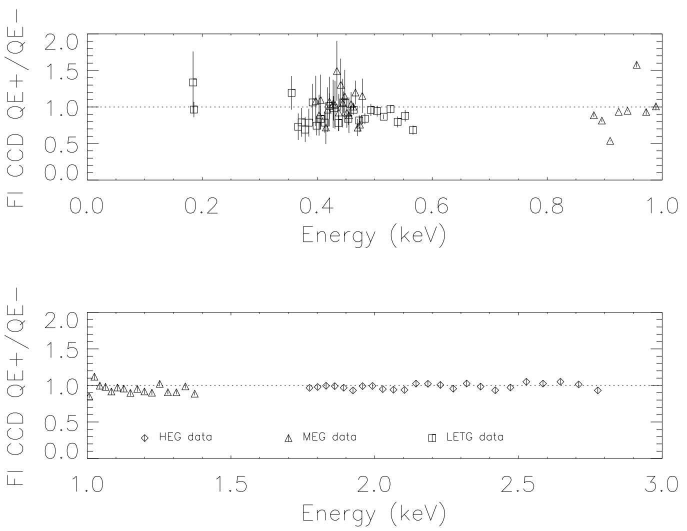

Figure 7.29: FI-to-FI count rate comparison. Ratio of the count rates from 30 pixel regions at the same dispersion distance from zeroth order but on two different frontside illuminated (FI) CCDs in the ACIS-S array. The different symbols indicated which grating data set was used to obtain the ratio. The ratios are comfortably close to unity for most of the energy range so that any deviations can be ascribed to variations of QE between FI CCDs. Data from regions near the Cu-L lines should be discounted because the analysis is very sensitive to the exact placement of the integration window around the emission lines. The analysis was designed primarily for regions where the spectrum varies slowly.

efficiencies, so we may examine the ratios of CCD QEs with these data. We kept track of which CCDs contributed to the ratios so that we could construct $R(E)$. When both orders were on FI CCDs, then all model curves cancel, so that we may test for differences in QEs between FI CCDs or check for grating positive-negative efficiency differences. Figure 7.29 shows the result. We see that there is remarkable consistency between FI CCDs, especially in the 1.8-2.8 keV region, once we discount the apparent discrepancies due to Cu-L lines. The analysis was designed for regions where the continuum was varying slowly, so it is not too surprizing that the L lines show deviations. These regions should be reduced separately and the effects of pileup should be taken into account.

The ratio of the fluxes determined for the BI CCDs could also be compared to those determined in the FI CCDs. The estimated fluxes already include the ratio of the BI to FI QEs. Figure 7.30 shows this ratio computed for each grating set. There are very significant, systematic deviations: 15-20% in the 2-4 keV band, 10-40% in the .5-.8 keV band, and differences greater than a factor of 2 below 0.35 keV. The FI QE in the latter region is extremely small and falling rapidly, so it is perhaps not too surprizing that there may be errors there. The fact that the QE ratio may be measured there may be more surprizing.

The deviations elsewhere, and especially in the 2-4 keV range, are more disturbing. Although investigations are in progress, we have identified an effect that may have bearing on this problem. In figure 7.31, we show the pulse height distribution for events detected by the S3 (BI) CCD and dispersed to a location consistent with energies in the range of 3.0 to 4.0 keV. The figure shows that there is a tail to the pulse height distribution (PHD) that contains a significant number of events and which deviates dramatically from the expected PHD measured from timed exposure mode data. This difference could arise from the inherent limitation of the on-board processing

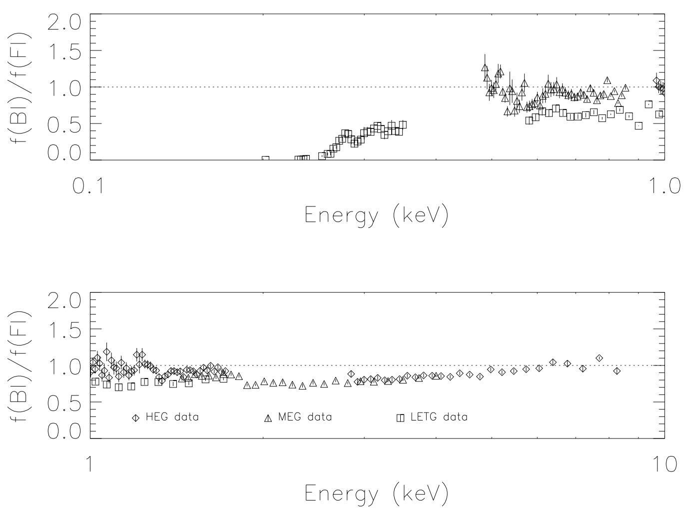

Figure 7.30: BI-to-FI count rate comparison. Ratio of the exposure and QE corrected fluxes from 30 pixel regions where the count rate from one side with a BI CCD is compared to that of a FI CCD on the opposite side at the same dispersion distance from zeroth order. The different symbols indicated which grating data set was used to obtain the ratio. This ratio indicates difficiencies in the ratios of the QE models for BI and FI chips. Investigations to explain the observed differences are currently focussed on the differences in event grade assignation between continuous clocking mode and the timed exposure mode normally used in calibration. As in figure 7.29, data points which are near or include the Cu-L lines should be discounted. Similarly, there is a point at Cu-Kα that is likely to be badly computed.

of continuous clocking mode event data. If an event is split such that a significant fraction of the charge appears in an adjacent row, then the event can be detected as two different events when operating in the continuous clocking mode.

7.8.4 Conclusion and Further Investigations

The tests proved extremely successful: we found no unusual features in effective area of the HETGS and LETGS to a level of about 5% and found that the models of the Ir and Au M edges agreed to within statistics in all cases. The detailed Ir M edge structure given most recent HRMA effective area curve match the data very well but there is a discontinuity at 2 keV which is not observed. The data were also used to show that the positive and negative orders of the gratings have consistent efficiencies and that the QEs of the frontside illuminated (FI) CCDs in the ACIS-S are all consistent. Finally, using the consistency of the positive and negative orders, we derive the ratio of the QEs of the backside illuminated (BI) CCDs relative to the FI CCDs and show that this ratio does not match the expected ratio of QEs. The reason for this discrepancy may be related to a change of event grades because ACIS was read out in the continuous clocking mode rather than in the timed exposure mode for which most calibration data exist. Finally, a pair of new hot columns (or pixels) was discovered that had not appeared in the preceeding tests.

These tests provided data that nicely validated the effective area model fine structure near known edges, so that we may be confident that spectral features in the spectrometer can be modelled adequately for observations after AXAF is launched. Concerns arise regarding the

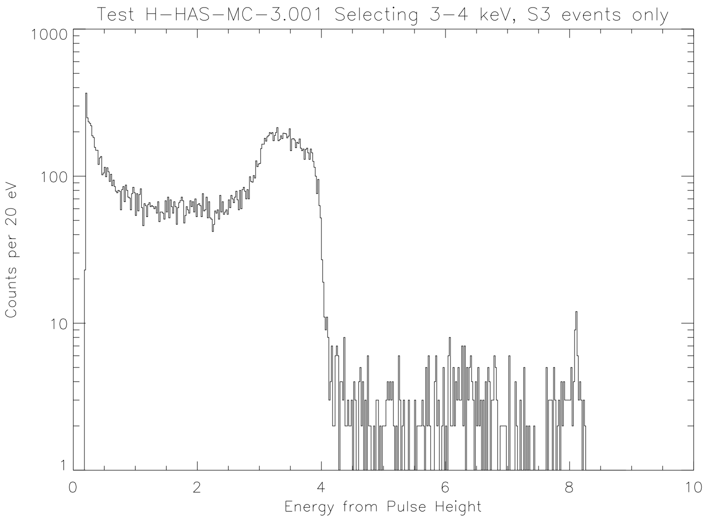

Figure 7.31: Pulse height distribution for CC data. The pulse height distribution (PHD) for a region of the S3 (BI) CCD selected from events whose dispersion corresponds to the 3-4 keV range, assuming $m = 1$ (taken from test H-HAS-MC-3.001). The peak in the 3-4 keV band is expected but the tail that extends to extremely low pulse heights contains much more power than expected. Normally, in timed exposure mode, of order 1% of events would appear in a small peak at 1.74 keV, which is the Si-K escape peak. The escape peak is not visible in this plot because it appears to have been swamped by events with partial charge collection.

HRMA effective area model near 2 keV that will be addressed by the telescope science team. In addition, we noted problems that may result from event loss.

One prospective reanalysis of the data would be to attempt to identify events that are actually associated with split events which were not recognized by the ACIS on-board processor. These events could be combined to improve the pulse height distribution so that the QEs of the BI and FI chips might be more closely comparable to that of timed exposure mode. Very little calibration data were taken in the continuous clocking mode but these data must be examined and modeled to see if the apparent QE differences we find can be explained.

There are grating observations of continuum sources that have yet to be reduced and analyzed. In one test, ACIS was read out in timed exposure mode, so we may be able to compare with the results from these observations. Pileup is expected to be more prevalent, however. Another series of tests involving continuous clocking mode employed the carbon EIPS anode, so data will be available for searching for features in the 0.8-1.1 keV region. A preliminary examination of the data[18] showed slightly different contaminants than observed in these copper anode tests.

These data can still be examined in a bit more detail for possible features in the O-K to Cu-Lζ energy range, spanning from about 0.5 keV to 0.8 keV. The details of the O-K edge structure have been measured at a synchrotron using polyimide filters similar to those used in the MEG, so these details should be incorporated into the HETGS grating efficiency curves.

7.9 Effective Area with HRC-I

Objective: Derive the HETGS(HRC-I) effective area and compare it to HRMA, HETG, and HRC-I measurements and predictions. HRC-I effects that must be understood include: quantum efficiency, quantum efficiency, and quantum efficiency.

Publication(s): Flanagan *et al.*[26]

7.9.1 HETG/HRC-I Tests at XRCF

The tests and data presented here are similar to the ACIS-S tests described in Section 7.7. The analysis here for the HETG-HRC-I does not currently include the BND data and hence only relative effective areas are described. In particular, the HRC-I detector uniformity and HETG grating symmetry can be assessed using the plus/minus first order ratio.

HETG was tested in combination with the HRC-I in Phase 2 at XRCF. The complete series consisted of one focus check at 1.254 keV, 33 effective area tests in a defocussed configuration, and one monochromator scan with 4 energies centered on 1.54 keV. These are listed in Table 7.5, along with the energy and range of dispersed orders on the detector.

Figure 7.32 shows the HRC-I with the HEG and MEG grating dispersion pattern at 7 keV. The HRC-I detector is square and the image of Figure 1 is presented in detector coordinates. The dispersion direction for the gratings is aligned approximately parallel to a diagonal of the detector, so that the number of orders detected is limited by the detector size and the intensity of the high orders. In general, the zero order position was displaced from the nominal imaging aim point in order to minimize accumulated dose in that region. Note that the direction of the bias angle of the microchannel plate is toward the top in the figure, and is not symmetric with respect to the dispersion direction. Details of the HRC-I and its calibration have been published by the HRC team[40, 41, 54].

7.9.2 Processing the HRC-I Data

The HRC data were processed in several steps. The raw data files were screened for lost major frames, converted from telemetry format and degapped. Starting with a compressed raw data file, file.rd.gz, the following steps are taken as summarized in the unix command line:

```
gunzip -c file.rd.gz | tm2ftm | nftm2prd -S/dev/null | nprd2epr -u1.0517 -v1.
0363 | nepr_sel -a4090 -P254 > file.nepr
```

The raw data file is uncompressed with `gunzip` then `tm2ftm` screens out lost major frames. Decommutation is preformed by `nftm2prd` with the option not to look at the rate data (`-S/dev/null`). Then `nprd2epr` degaps the data and makes an event list (where 1.0517 and 1.0363 are the u,v degap parameters). Finally, `nepr_sel` sets the amplifier saturation value to 4090 and the upper PHA value to 255. The file `file.nepr` is the desired event list file.

Run ID	TRW ID	Energy keV	HEG Orders	MEG Orders	Comments
i0810621	G-HHI-EA-7.048	7.0	+6 to-6	+3 to -5	
i0811327	G-HHI-EA-99.059	7.0	+4 to -4	+3 to -5	
i0810657	G-HHI-EA-7.047	6.3	+6 to -5	+8 to -5	
i0811342	G-HHI-EA-99.060	6.3	+4 to -4	+8 to -3	
i0810725	G-HHI-EA-7.046	5.76	+5 to -5	+8 to -5	
i0811356	G-HHI-EA-99.061	5.76	+4 to -4	+5 to -5	
i0810804	G-HHI-EA-7.045-1	5.66	+5 to -5	+8 to -9	
i0810756	G-HHI-EA-7.045	5.66	+5 to -5	+5 to -7	
i0810831	G-HHI-EA-7.044	5.48	+5 to -4	+7 to -5	
i0810855	G-HHI-EA-7.043	5.32	+5 to -4	+7 to -8	
i0810916	G-HHI-EA-7.042	5.25	+5 to -4	+8 to -7	
i0810936	G-HHI-EA-7.041	5.13	+4 to -4	+5 to -5	
i0810950	G-HHI-EA-7.040	5.05999	+4 to -4	+6 to -5	
i0811005	G-HHI-EA-7.039	4.96	+4 to -4	+5 to -7	
i0811019	G-HHI-EA-7.038	4.9	+4 to -4	+7 to -8	
i0811037	G-HHI-EA-7.037	4.8	+4 to -4	+7 to -5	
i0811054	G-HHI-EA-7.036	4.59999	+4 to -4	+7 to -5	
i0811114	G-HHI-EA-7.035	4.51	+4 to -4	+7 to -5	
i0811132	G-HHI-EA-7.034	4.0	+4 to -4	+7 to -7	
i0811155	G-HHI-EA-7.033	3.5	+3 to -3	+7 to -6	MEG 2 overlaps HEG 1, Not corrected.
i0811238	G-HHI-EA-7.032	2.29	+2 to -2	+4 to -4	
i0811414	G-HHI-EA-7.031	1.95	+2 to -1	+4 to -4	
i0811434	G-HHI-EA-7.030	1.7	+2 to -1	+3 to -3	
i0940311	G-HHI-EA-9.018	1.48693		+3 to -3	MEG only. Has contaminant line.
i0911019	G-HHI-EA-6.002	1.254		+2 to -2	MEG only. EIPS - broad line.
i0911034	G-HHI-EA-6.003	1.254	+1 to -1		HEG only. EIPS - broad line.
i0910739	G-HHI-FC-1.003-Q1	1.254	+1 to -1	+2 to -2	
i0910817	G-HHI-FC-1.003-Q2	1.254	+1 to -1	+2 to -2	
i0910854	G-HHI-FC-1.003-Q3	1.254	+1 to -1	+2 to -2	
i0910931	G-HHI-FC-1.003-Q4	1.254	+1 to -1	+2 to -2	
i0940337	G-HHI-9.019	1.17595		+1 to -1	MEG only. W contaminant line.
i0811452	G-HHI-10.003	1.54	+1 to -1	+3 to -2	Energy scan; analysis complete.
i0940357	G-HHI-9.020	0.95996			Not analyzed
i0902304	G-HHI-6.004	0.9297			Not analyzed. MEG only.
i0902318	G-HHI-6.006	0.9297			Not analyzed. HEG only.
i0940427	G-HHI-9.021	0.75996			Not analyzed
i0901229	G-HHI-6.005	0.705			Not analyzed
i0940505	G-HHI-9.022	0.70499			Not analyzed
i0900251	G-HHI-6.001	0.5249			Not analyzed. MEG only.
i0900336	G-HHI-6.001-b	0.5249			Not analyzed, MEG only, Contains O.

Table 7.5: Summary of all HETG-HRC-I data sets taken at XRCF.

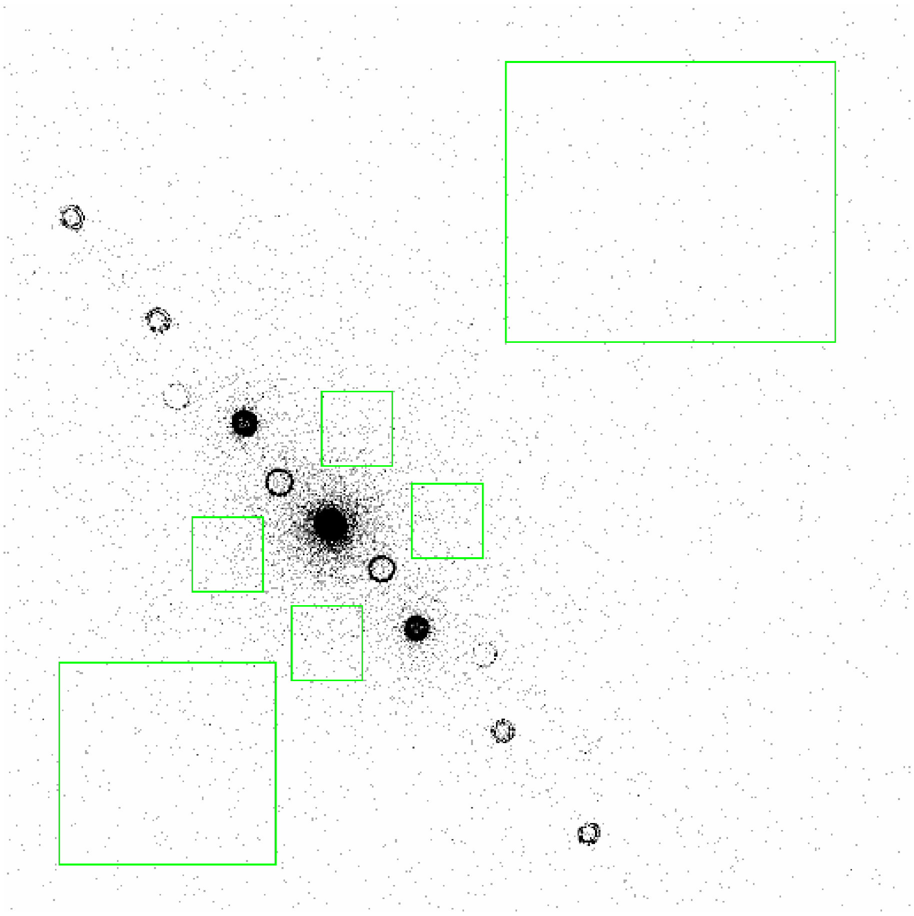

Figure 7.32: HETG-HRC-I image from test at 7 keV. Positive orders are dispersed toward the upper left in the figure. The large box, top right, is used to estimate detector background. The small boxes around zero order sample mirror-scattered events. The data have been "cleaned" to remove saturated events.

7.9.2.1 Event selection criteria

Two sets of event lists were then created, with different rejection criteria based on the saturation levels of the electronics (4096 for the amplifiers and 255 for the pulse height). This approach was prompted by considering the testing conditions early in Phase 2. In the first day of the HETG-HRC-I tests, the detector high voltage was set at a relatively high level and there was a considerably higher fraction of saturated events. This unusual saturation level[54] was decreased on subsequent days (the high voltage was lowered) and has been eliminated in the flight instrument.

Since readout saturation can also result in incorrect position assignment of the events (of order 1/2 mm or less), two separate analyses were performed on the data. In the case of "cleaned" data, all events with pulse height above 254 or with amplifier value above 4090 were rejected. In the second case, saturated events were included in the analysis (for which the data were termed "uncleaned"). There is evidence to suggest a higher proportion of saturated events in bright orders relative to faint orders. (This is currently under study.)

7.9.2.2 Background Subtraction

The technique employed for selecting regions of the grating readout was to display each dataset with SAOtng[65]. Each order of interest was captured in a simple rectangular box region, and the number of events within each box was determined. In order to estimate the effects of background and mirror scattering, several "background" regions were selected, as illustrated in Figure 7.32. The largest box, distant from the zero order, is assumed to reflect approximately detector backgound. The next largest box, while distant from the zero order, nevertheless was found to have a higher ($\sim$ 2 times) background rate and is assumed to contain mirror-scattered photons. The selection of small boxes centered among zero and 1st order had a much higher ($\sim$ 8 times) background rate, which is presumed due to mirror scattering around the zero order. (The c program which counts the events within the box region is /nfs/wiwaxia/h2/kaf/hrc/src/ssm/fits/nepr_sel_kaf.c.)

In the analysis, the simple detector background was used for background subtraction for all orders. This is appropriate for the distant high orders, but there may be mirror-scattered photons captured within the first order regions. Mirror scattering is on the 1% level or less, and by using the measured "scattered rate", we found that corrections to the ratios systematically increase it by 0.5% to a few percent, a negligible effect given the counting statistics and other errors. We have neglected this correction.

7.9.2.3 Detector Uniformity

Flat field tests to measure detector spatial uniformity were not performed with the settings used on the day on which most of the HETG-HRC data were taken. However, the HRC-I was known to be *more* uniform than on subsequent days, for which uniformity data are available[54] at 4.5 keV and 1.49 keV. At 4.5 keV, the HRC-I was found to be uniform to better than 5% over the central region. At 1.49 keV, the detector QE was not as uniform as at the higher energy, but was flat at the 10% level over the central region[54] out to a radius of 30 to 35 mm. Beyond this radius the QE dropped by $\sim$ 20%. No detector uniformity corrections have been applied to the measured ratios.

Error	magnitude	Comments
Counting Statistics	10% to 30%	accounted for in analysis
Background subtraction	up to 3%, systematic	only detector background used
bias angle	few percent	neglected
detector QE nonuniformity	5 to 10% within 35 mm radius; edges drop by 20%	neglected
Event saturation	10 % to 40% systematic	accounted for: all events included

Table 7.6: Corrections, systematic sffects and srrors in HETG-HRC-I analysis

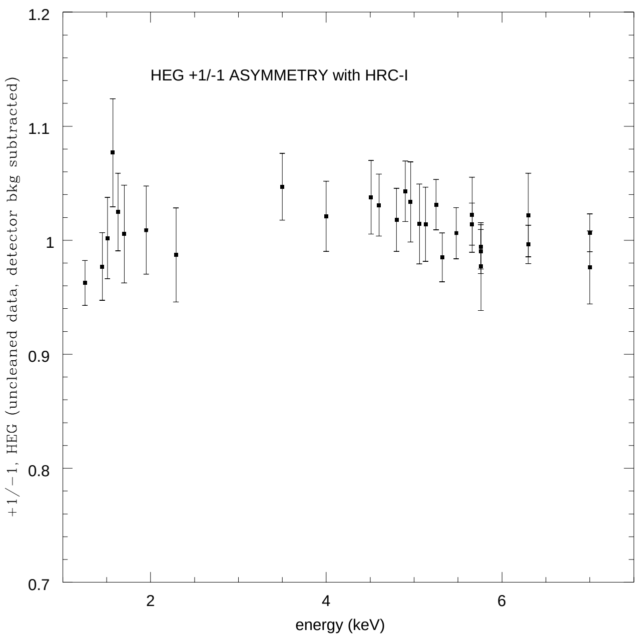

Figure 7.33: Ratio of +1 to -1 for HEG grating on HRC-I. In general, departures from unity are expected to be caused by intrinsic grating asymmetry, detector nonuniformity, or bias angle effects.

7.9.3 Plus/minus First Order Asymetry

It has been noted that the bias angle is not symmetric with respect to the dispersion direction. This can result in an asymmetric detection efficiency of a positive order with respect to its negative counterpart. The angle dependence of the QE is estimated to result in a difference[34] of at most a few percent, and correcting for bias angle has been neglected. In order to examine the potential effects of bias angle on the result, the ratio of the +1 order to the -1 order was taken. Any systematic asymmetry would most likely be ascribed to grating asymmetry in these orders, detector asymmetry due to bias angle, or to nonuniform QE effects across the detector (known to be small). The result is given in Figure 7.33 for the HEG grating, which is more likely than the MEG to show intrinsic asymmetry and which disperses across more of the HRC-I surface. The plot reflects asymmetry due to all effects: the asymmetry is obviously very small in comparison with other errors. Thus, neglect of bias angle and detector uniformity corrections is acceptable. Table 7.6 gives a summary of the various effects that have been discussed and their impact on the results.

7.10 Efficiency: High-Order Efficiency Measurements

Objective: Calculate the relative efficiencies of the diffracted orders seen in the Phase 2 flight detector data in order to calibrate the HETG high-order efficiencies. The use of the two detector's data sets allows likely detector effects to be separated from HETG effects.

Publication(s): Flanagan *et al.*[26], Schulz *et al.*[71]

7.10.1 Overview

During Phase 2 XRCF testing some 54 HRC-I and ACIS-S EA measurements were made with the HETG inserted in the beam. Descriptions and analyses of these data sets are presented in Sections 7.7 and 7.9. The data from these tests can be used to test the predicted high-order efficiencies, expressed as a ratio of high-order to first-order efficiency; these predicted ratios are shown in Figure 7.34. Given that the intensity of higher orders is a strong function of grating bar shape[47], the extension of the subassembly model to very high orders is tenuous, underlining the need for direct measurement at XRCF. Thus, the measurements reported here provide a necessary complement to the limited set of laboratory high-order efficiency measurements that was made on each of the flight gratings. In addition, analysis of the data has yielded insight into both the HRC-I and ACIS-S instruments in aspects that were not fully examined at subassembly level.

7.10.2 HRC-I Data Sets

The HRC-I data sets and aspects of their analysis are described in Section 7.9. From Table 7.5 it is evident that HEG 2nd order is only available on the detector for energies of 1.7 keV and above. For the MEG gratings, 2nd order was suppressed and measurable at only a few energies, but third order was detectable at 1.49 keV and above. Energies below 1.254 keV were not analyzed for either grating since there were no higher orders falling on the detector. The breakdown of order by energy is given in Table 7.7.

Order	HEG Energy range	MEG Energy range	Comments
2	1.7 to 7.0	1.254, 1.7, 1.95, 2.29	not sufficiently detectable at other energies
3	3.5 to 7.0	1.48693 to 7.0	
4	4.0 to 7.0	1.95 to 6.3	not sufficiently detectable at 7.0
5	5.25 to 7.0	3.5 to 7.0	
6	6.3 and 7.0 only	3.5 to 6.3 except 5.13	
7		3.5 to 5.76 except 5.05999, 5.13	
8		4.9, 5.25, 5.32, 5.66, 5.76, 6.3	
9		5.66 only	

Table 7.7: Energy ranges of the measured HETG-HRC-I higher orders.

A detailed investigation showed that smearing of the image due to electronic saturation did *not* systematically affect the result: ratios remained unchanged to within $\sim 3\%$ regardless of whether or not the smeared events were captured within the counting region. This is understandable since the regions of interest used were large compared to the position errors due to saturation.

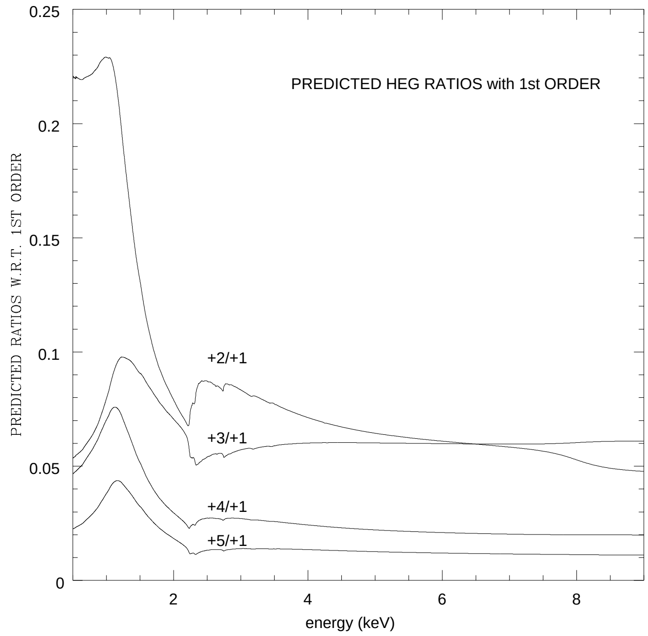

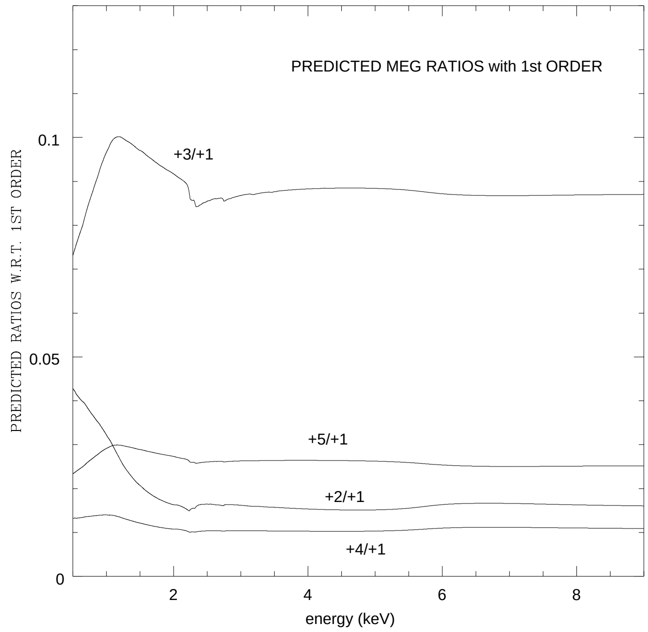

Figure 7.34: Predicted ratios of orders 2 through 5 with respect to 1^{st} order for HEG (top) and MEG (bottom). These are based on subassembly calibrations.

However, as mentioned in Section 7.9, there is evidence to suggest a higher proportion of saturated events in bright orders relative to faint orders. If so, then when "cleaned" data are used, ratios formed with a bright first order are systematically enhanced (by 10% to 40%). Therefore, since saturated events represent true X-ray events and their positioning errors do not compromise the analysis, we have chosen to use the "uncleaned" data set throughout this order-ratio analysis.

Grating	Order Ratio	Typical Counting Statistics	Assigned Subassy Error	Deviation from Predicted
HEG	2/1	10%	20 to 25%	-10 to -15%
	3/1	10%	50%	-35%
	4/1	15%	90%	-35%
	5/1	20%	90%	-60%
	6/1	20%	90%	-60%
MEG	2/1	15%	20 to 25%	≈ correct
	3/1	10%	50%	-5%
	4/1	20%	90%	+25%
	5/1	20%	90%	-25%
	6/1	20%	90%	≈ correct
	7/1	20%	90%	-25%
	8/1	30%	90%	≈ correct
	9/1	30%	90%	-45%

Table 7.8: Comparison of Predictions with Measured ratios for HETG + HRC-I higher orders.

7.10.3 Discussion of HRC Order Ratios

Figure 7.35 shows the measured HEG ratios for 2nd, 3rd and 4th orders overlaid with the predictions of Figure 7.34. (Solid points are the ratios of positive orders, hollow points refer to negative orders. The error bars reflect only counting statistics.) The 5th and 6th order ratios are similar and are not shown. The measurements appear to be systematically suppressed relative to the predictions. The approximate magnitudes of these deviations are given in Table7.8 along with the typical errors due to counting statistics. Although the departures are within the errors assigned to the predictions, they exceed the counting statistics and other uncompensated correction effects, and are taken to be significant.

Figure 7.36 shows the shows the measured MEG ratios for 2nd, 3rd, 4th and 5th orders. In general, there is fairly good agreement with the predictions. Moreover, the higher ratios (orders 6 through 9) are similar, agreeing reasonably well with the subassembly predictions. These results are summarized in Table 7.8.

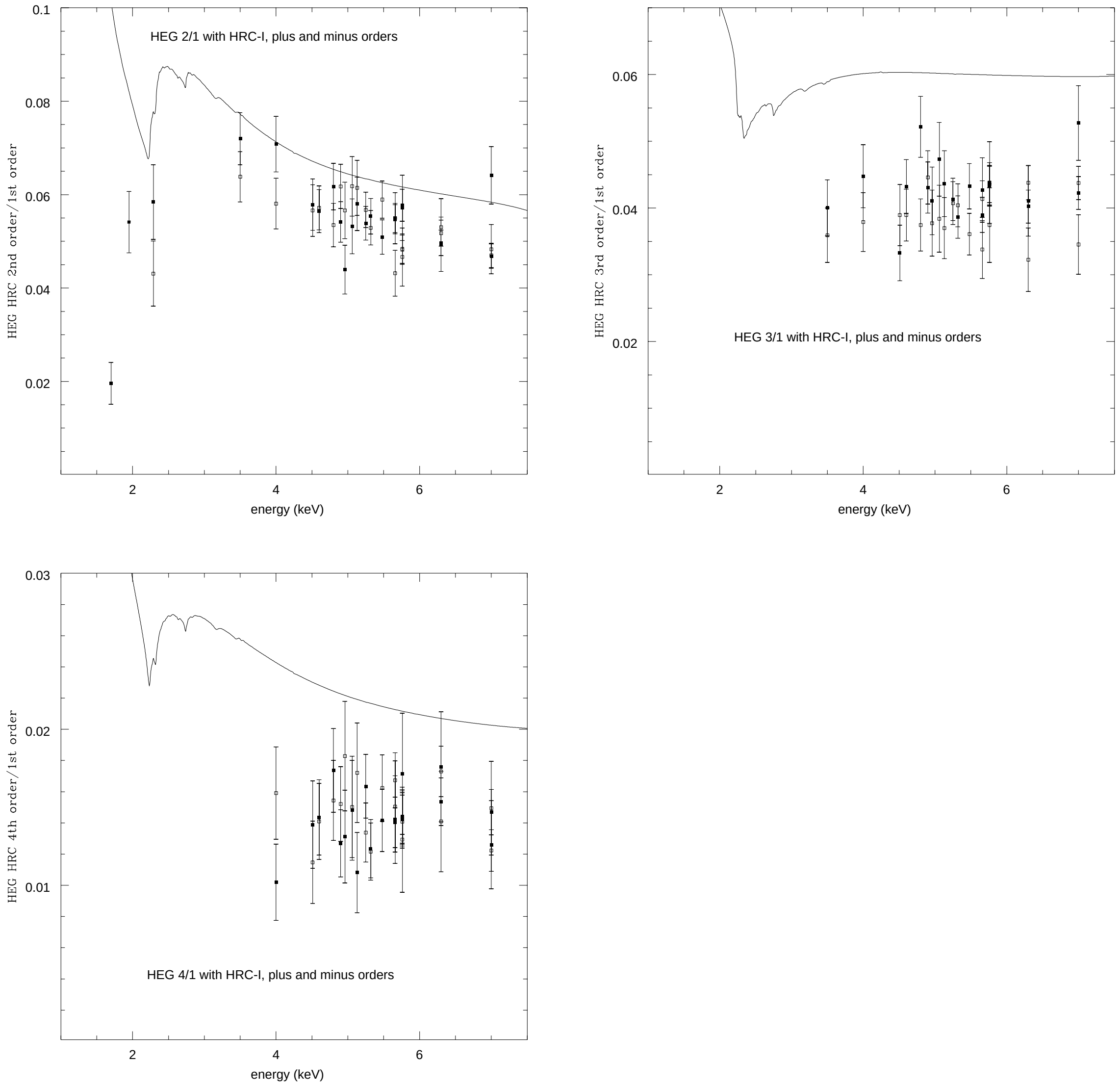

Figure 7.35: Measured HEG ratios for 2nd,3rd, and 4th orders with HRC-I. The solid curve represents the predicted ratios. Hollow points indicate ratios of negative orders, and solid points refer to positive orders. The error bars are due to counting statistics. The measurements systematically fall below predictions.

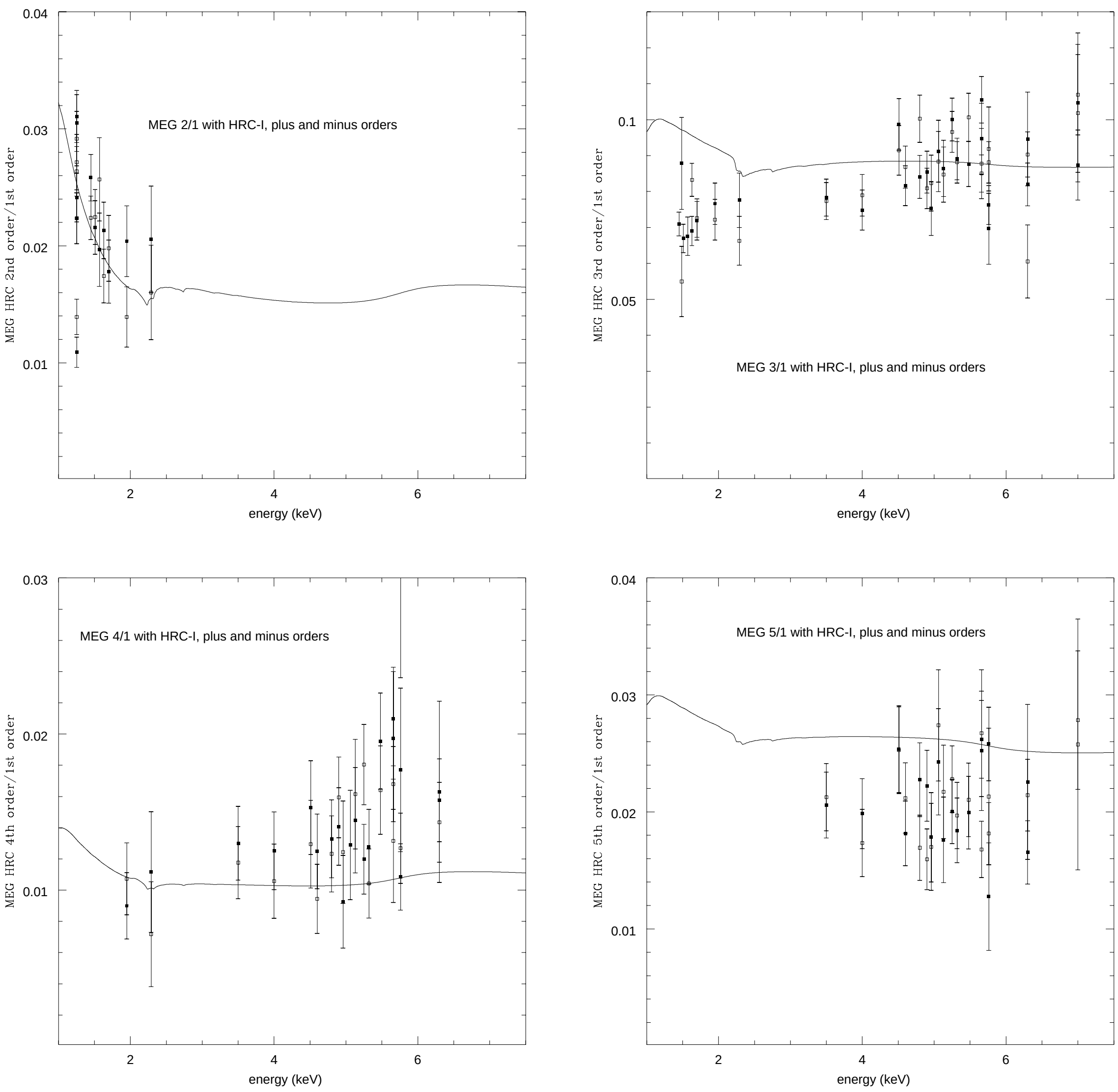

Figure 7.36: Measured MEG ratios for 2nd,3rd, 4th and 5th orders with HRC-I. The measured values agree fairly well with the predictions.

7.10.4 ACIS-S/HETG Order Ratios

Figure 7.37 shows the HEG 2nd, 3rd, 4th and 5th order ratios. Ratios between positive orders are denoted with filled boxes, whereas those between negative orders are marked by hollow boxes. In each one of these plots, there is a strong enhancement above 7 keV. Since it is common to all four order ratios, it likely arises from a supression of first order effective area. From the 2nd order ratio, it is clear that this feature is far stronger it the -2/-1 ratio (where the -1 order is captured by a FI device) than in the +2/+1 ratio (where the +1 order lands on the S3 chip, a BI device). The 3/1 ratio agrees generally with the HRC-I results over the energy range of 3 to 5 keV, but then the ratio is enhanced above 5 keV and shows other structure. In general, the HEG ratios with ACIS-S show much structure and do not reproduce the systematic reduction relative to predictions as shown with the HRC-I.

Figure 7.38 shows the MEG 3rd, 5th, 7th and 9th order ratios. The 3rd and 5th orders show enhancements above 5 keV, but there appear to be some smooth regions (2.5 to 4.5 keV) which agree reasonably well with predictions.

The features that have been noted can be traced to detector effects which will be discussed below.

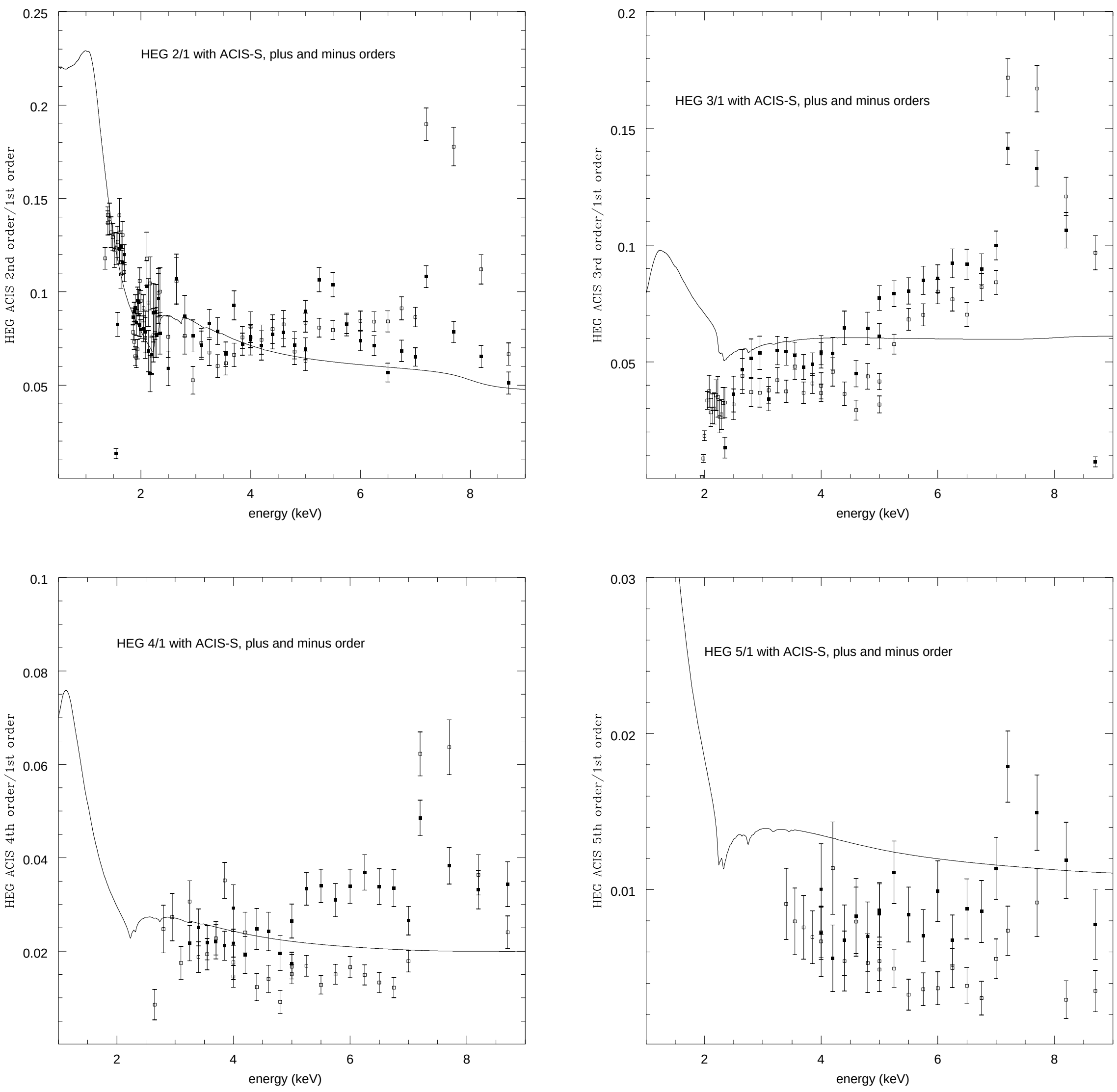

Figure 7.37: Measured HEG ratios for 2nd, 3rd, 4th and 5th orders with ACIS-S.

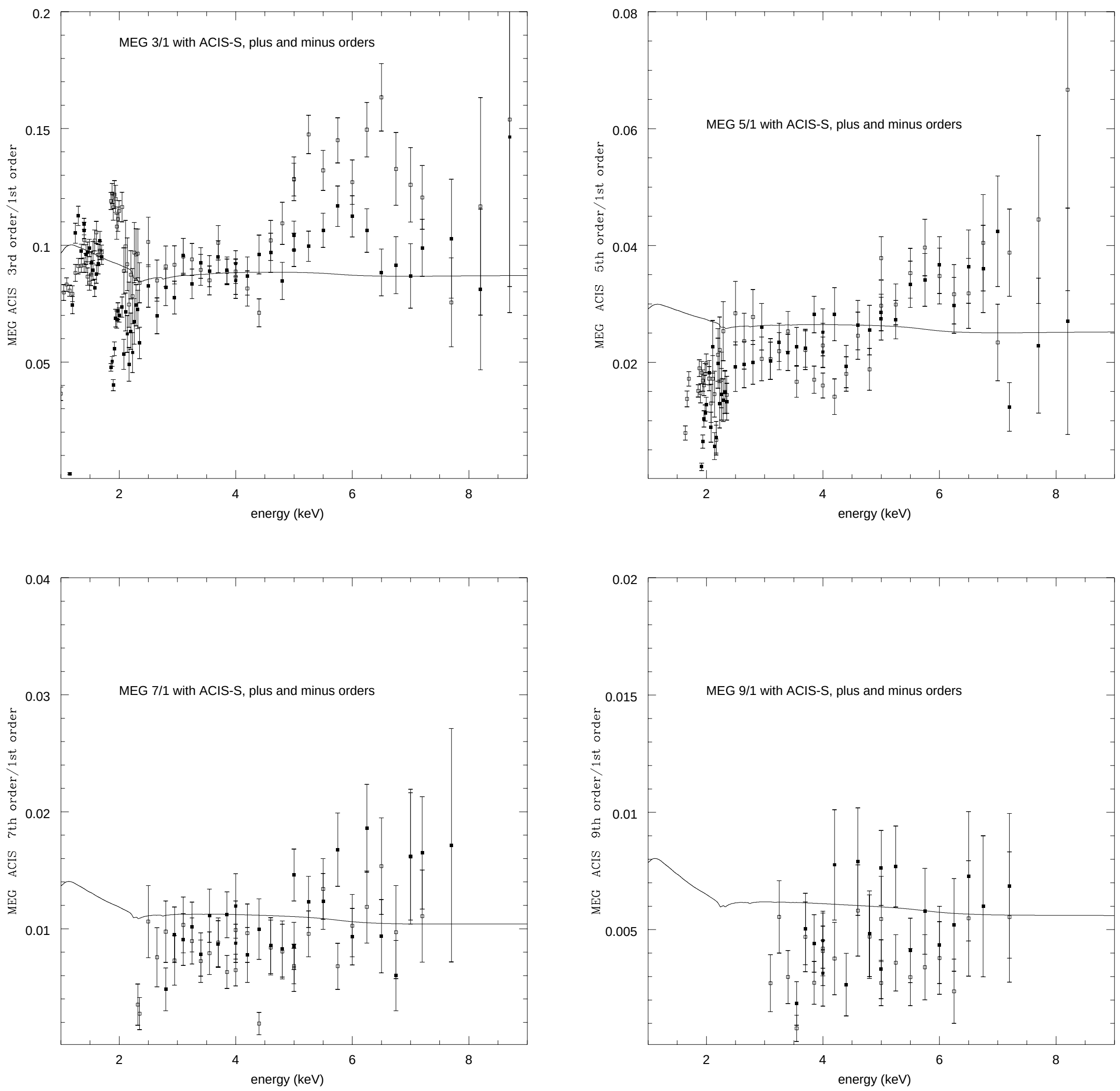

Figure 7.38: Measured MEG ratios for 3rd, 5th, 7th, and 9th orders with ACIS-S.

7.10.5 Discussion of ACIS-S/HETG Order Ratios

The absolute effective areas derived in Section 7.7 in general agree with the expected effective area function to quite a high degree. However, there are significant local deficiencies that remain. The most prominent is an apparent drop of effective area for HEG +1 and -1 orders below the expected curve at energies above 5 keV, Figure 7.21.

One possible explanation is a local non-uniformity effect in the beam to which the HEG, because of its smaller aperture, would be more susceptible than the MEG. (In the MEG such a drop is not significantly visible in the data.) However, the observed drop in HEG area sometimes exceeds 10%, which would need a quite strong local non-unifomity in the beam. This is unlikely since the DCM beam at higher energies has been measured to be very uniform overall. In addition, if beam nonuniformities were the cause, the 2nd order effective area would also show this deficiency, but it does not. Also none of the beam uniformity meaurements ever performened at that energy ever showed any significant deviations. Therefore a local beam uniformity effeect can be ruled out.

A more plausible explanation, which is currently under investigation, are deficiencies in the CCD quantum efficiencies caused by grade migration and lost charge effects at high energies and high fluences (see Section 7.7.3). The HEG is more susceptible to these effects since the fluence in the HEG image at XRCF is generally higher than in the MEG image (recall that the HEG mirror shells are of smaller diameter). A quantitative assessment of these effects is still under way.

During subassembly testing of the ACIS instrument, fluences were low and grade migration and lost charge effects were not observed[1]. Although the focused beam at XRCF increases the fluence, the higher order grating efficiencies are low enough that fluences in these orders drop below those of subassembly testing. Thus, grade migration and lost charge effects should not be noticed in any order other than 1st (see also Section 7.7). Key indicators for grade migration and charge loss effects are the ratios of the lower orders to the first orders. (Higher order ratios will have poor counting statistics and large uncertainties.) Figures 7a and 8a show the HEG 2nd to 1st order ratio and the MEG 3rd to 1st order ratio. The solid line indicates the prediction. Clearly, in both figures the ratios start to deviate from the prediction above 5 keV, suggesting a deficiency in the 1st order effective area. Here the HEG, as expected, shows the strongest deviations. Above 5 keV we probably see the effects of grade migration, and above 7 keV the additional effect of charge loss. The latter effect is more pronounced in the negative order ratio (empty squares) where the 1st order appears on a FI device, as compared to the positive ratio (filled squares), where the 1st order appears on a BI device. This is consistent with the related effect of 'blooming' caused by high energy events in FI devices; it is not seen in BI devices[59]. The effects are also observed in the HEG 3rd and MEG 5th order ratios. At higher orders, the ratios follow the predictions nicely, however the data show significant scatter due to poor counting statistics.

We can rule out the possibility that these effects are caused by the grating itself, because they are not observed in analogous measurements with the HRC-I. As discussed earlier, the near-perfect symmetry of the +1 and -1 orders (to within 5%) of the HEG with HRC-I exclude the grating as a contributor to these effects.

7.10.6 Conclusions

We have examined the ratios of higher grating orders with respect to the first order for Phase 2 tests of HETG with the flight instruments, HRC-I and ACIS-S. We found that:

- The symmetry of the +1 and -1 orders of HEG with HRC-I lead to the conclusion that detector nonuniformity, grating asymmetry and bias angle effects were small.
- HRC measurements show suppressed higher grating orders for HEG relative to predictions. Measurements of the MEG orders agree well with predictions.
- ACIS-S shows strong detector effects, compatible with grade migration and charge loss, especially in the HEG 1st orders.

Several items remain for future work. These include:

- Investigate the relation between saturation and count rate density in HRC-I.
- Quantitative analysis of grade migration and charge loss in ACIS-S.
- Incorporate synchrotron high order measurements.
- Examine Phase 1 measurements for high orders and asymmetry.
- Analyze EIPS sources with both detectors and the monochromator scan with HRC-I.